Doctoral Thesis

A Study on Efficient Charge Transport Layer for High-Performance Perovskite Based Light-Emitting Diodes

Da Bin Kim

Department of Materials Science and Engineering

Graduate School of UNIST

2019

A Study on Efficient Charge Transport Layer for High-Performance Perovskite Based Light-Emitting Diodes

Da Bin Kim

Department of Materials Science and Engineering

Graduate School of UNIST

A Study on Efficient Charge Transport Layer for High-Performance Perovskite Based Light-Emitting Diodes

A thesis/dissertation

submitted to the Graduate School of UNIST

in partial fulfillment of the

requirements for the degree of

Doctor of Philosophy

Da Bin Kim

07. 12. 2018 of submission

Approved by

Advisor

Myoung Hoon Son

A Study on Efficient Charge Transport Layer for High-Performance Perovskite Based Light-Emitting Diodes

Da Bin Kim

This certifies that the thesis of Da Bin Kim is approved.

07. 12. 2018 of submission

Advisor: Myoung Hoon Song

Doo-Hyun Ko: Thesis Committee Member #1

Jin Young Kim: Thesis Committee Member #2

Hyesung Park: Thesis Committee Member #3

Min Sang Kwon: Thesis Committee Member #4

Abstract

Recently, metal halide perovskite has been attracting attention as a next generation display material due to their low cost and simple solution processibilities and excellent properties such as high color purity, easy color tunability and high photoluminescence quantum efficiency of up to almost 100%.

Balanced charge transport using an effective charge transport layer and excellent film surface morphology with low defect density are key factors for achieving high performance perovskite-based light-emitting diodes (PeLEDs). The optimum charge transport characteristics are realized by well-matched energy level alignment for efficient charge injection and blocking the opposite charge to confine charges for radiative recombination within perovskite emissive layer. Moreover, the growth of crystalline perovskite and the stability of the perovskite films are also influenced by the surface of charge transport bottom layer.

Here, I present effective charge transport layers employing PEDOT: molybdenum oxide (MoO_3) composite layer, nickel oxide (NiO_x) and Poly(9-vinylcarbazole) (PVK) bilayer as a hole transport layer in p-i-n structured PeLEDs.

In chapter 2, I demonstrate the enhanced performance of PeLEDs using a solution-processable MoO_3 and poly(3,4-ethylenedioxythiophene):poly-styrene sulfonate (PEDOT:PSS) composite layer as the hole transport layer (HTL). The PEDOT:MoO_3 composite layer presents improved hole injection through a reduction in the contact barrier between the HTL and the $CH_3NH_3PbBr_3$ layer and enhanced crystallinity of the perovskite film. The optimized PeLEDs with the PEDOT:MoO_3 composite film showed enhanced external quantum efficiency (EQE) and maximum luminous efficiency, compared to a PeLEDs using a pristine PEDOT:PSS layer.

In chapter 3, I investigate the interfacial energetics and optoelectronic properties of the perovskite layer grown on a NiO_x, and PEDOT:PSS layers. The perovskite grown on NiO_x/ layers presents lower density of traps/defects and balanced charge carrier transport in the perovskite layer, leading to significantly improved device efficiency, photostability of perovskite, and operational stability of PeLEDs.

In chapter 4, I introduced the NiO_x/PVK bilayer for the enhanced hole injection in quasi-2D PeLEDs. PVK was introduce to match the energy level between NiOx and perovskite layer. However, the perovskite film on hydrophobic PVK layer exhibited poor morphology due to non-wetting problem from a hydrophilic perovskite precursor solution. In order to solve the morphology problem of perovskite layer, hot-casting method that heat was applied to the substrate layer to improve the perovskite morphology and crystallinity.

The efficient charge transport layer engineering is simple and promising way for balanced charge

injection and realizing high-performance PeLEDs.

Keywords : perovskite light-emitting diodes (PeLEDs), charge transport layers (CTLs), high efficiency PeLEDs, nickel oxide (NiOx), PEDOT:MoO_3 composite layer, quasi-2D perovskite

Contents

List of Figures

Chapter 1. Introduction

1.1 Perovskite Light-emitting materials

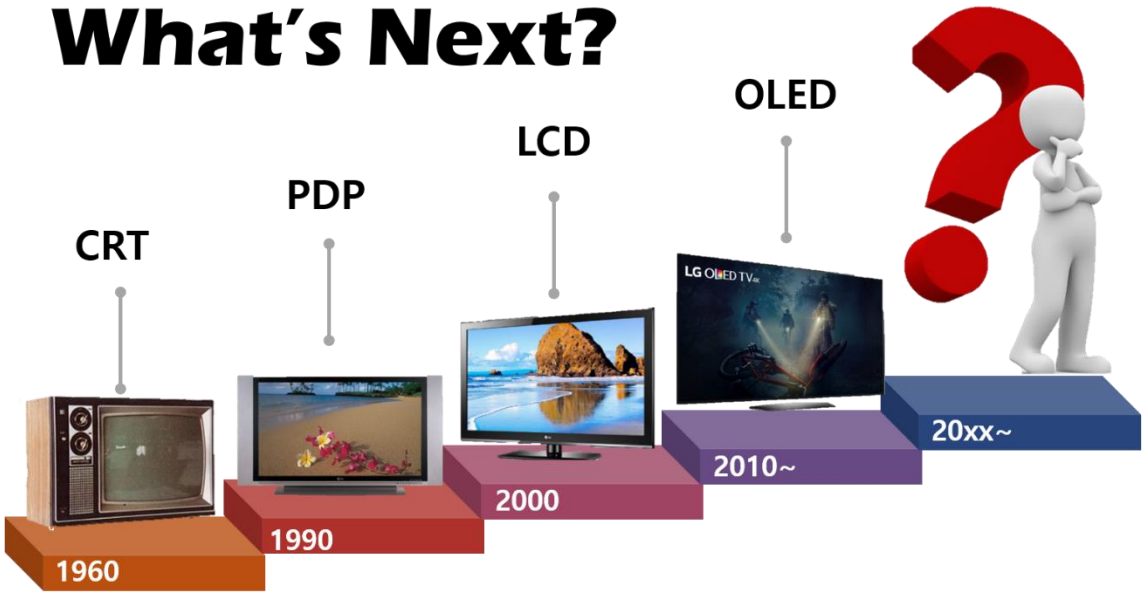

Figure 1.1. Display trends

The global display market is expected to be commercialized with 5G communication and ultra-high resolution 8K as a new power source. With the development of data communication technology, a large amount of data can be transmitted, and thus a demand for an ultra-high resolution display is increasing. And because of the increased demand for virtual reality (VR) related technology, it is necessary to develop a new display material capable of realizing near realistic brightness and color. Conventional organic light emitting materials in organic light emitting diode have a disadvantage in that they have high luminous efficiency but are expensive and have low color purity. (**Figure 1.1**)

The perovskite material is a crystal structure with ABX_3 formula, which is a metal oxide of a special structure that shows superconductivity as well as non-conductor, semiconductor, and conductor properties. In particular, the halide-based perovskite materials attracted much attention in optoelectronic devices such as solar cells[1-3], light emitting devices (LEDs)[4-7], photo sensor[8-10], amplified spontaneous emission (ASE) and lasers[11-15] due to their excellent electrical and optical properties[16-19]. The perovskite has recently been reconsidered as new light emitting materials because of the breakthrough in photovoltaics. It can control various electrical and optical properties by controlling the composition of the compound and processing method. Perovskite has the formula ABX_3, A site is generally occupied by monovalent cation such as methylammonium (MA^+, $CH_3NH_3^+$) or formamidium (FA, $(NH_2)_2CH^+$)) or cesium cation (Cs^+). B site is normally occupied by a divalent metal cation such as lead cation (Pb^{2+}) or tin cation (Sn^{2+}), and X site is a monovalent halide anion, which is a halogen

element such as iodine anion (I^-), bromide anion (Br^-), chloride anion (Cl^-). The many natures of perovskites depends on this constituent compound. The perovskite structure is shown in **Figure 1.2**. The Goldschmidt tolerance factor (t) shows how stable the perovskite structure is made by the various element. The equation is as follows.[20-22] (1.1)

$$t = (R_A+R_X)/\sqrt{2}(R_B+R_X) \quad (1.1)$$

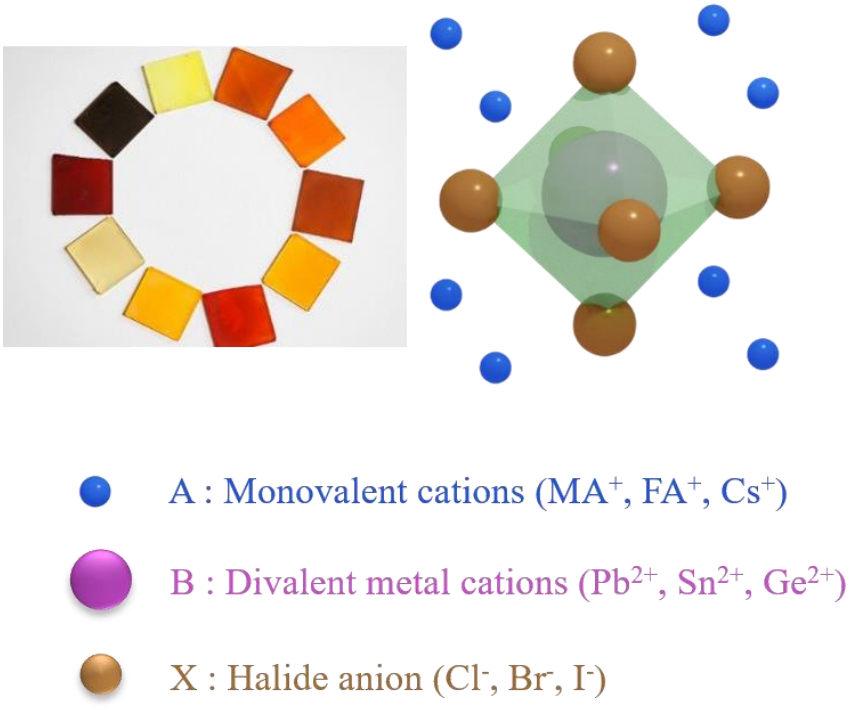

Figure 1.2. Perovskite structure

where R_A, R_B and R_x are effective ionic radii of A, B, and X element, respectively. In the 3D halide perovskite, the t value must only be within the range of 0.8-1.1. When the t value is 0.9 to 1, the perovskite with cubic structure is formed and a distorted perovskite structure such as rhombohedral, orthorhombic, or tetragonal structures are formed when the t vale is 0.8-0.99. (**Figure 1.3**)

These perovskite materials have unlimited potential as LED materials. The emission wavelength of the perovskite can cover the visible light region with composition control of perovskite. The high color purity of the perovskite is also suitable as an upcoming super-high definition display material. The external photoluminescence quantum efficiencies (PLQEs), which is a typical property of the luminescent materials, is located at 20-50%[4, 23] in the cased of a thin film but it is reported that PLQE

is over 90% if the perovskite defects are passivated[24, 25], low dimensional structure[26-28] is formed or in nanocrystals[29, 30]. The perovskite has both the advantages of organic materials (low cost and solution processability) and inorganic materials (e.g. high charge mobility[31-33]). The perovskite films are fabricated easily by solution-deposition or vapor deposition[34-36]. The quality of the produced films is influenced by the factor of the deposition process such as composition ratio[4], substrate temperature[37, 38], annealing condition[39-41], solvent treatment[42, 43] or additive[44] (**Figure 1.4**). These factors regulate perovskite PLQE, morphology and grain size. Therefore, in order to produce perovskite films of the performance we desire, these factors must be considered with the film.

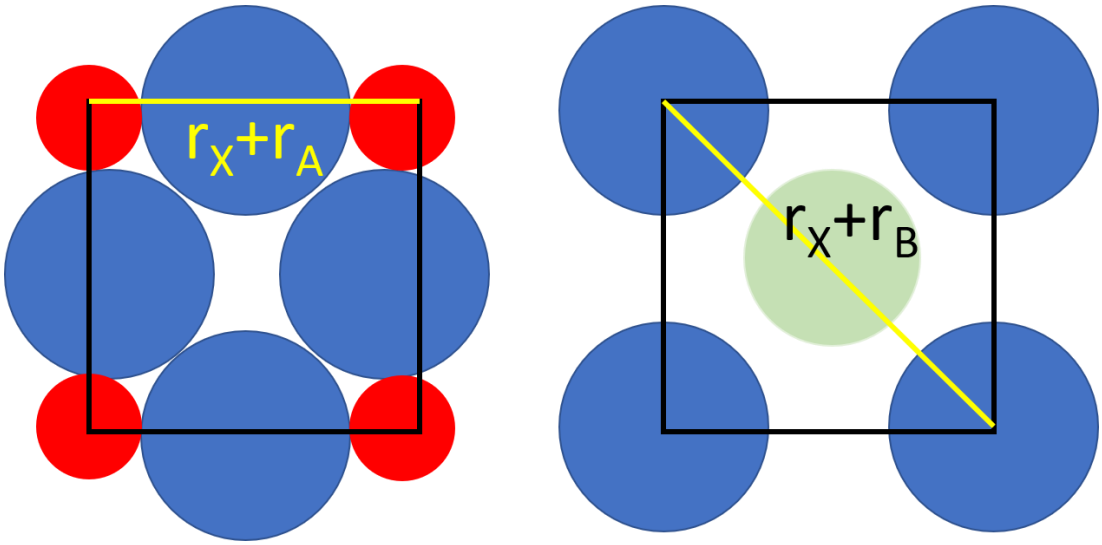

Figure 1.3. Goldschmidt tolerance factor

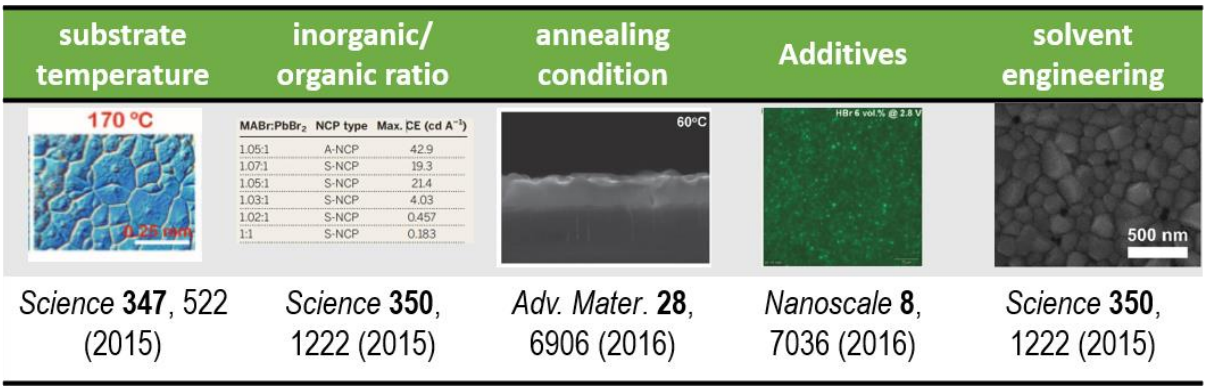

Figure 1.4. Parameters of perovskite film deposition

1.1.1 High color purity of perovskite

The narrow emission linewidth of perovskite is the greatest advantage and is the main cause of the active research in this PeLEDs field. The full width half maximum (FWHM) of perovskite is about 20nm at the green emission, which is significantly lower than of organic LEDs (OLEDs, FWHM : ~40nm)[45-47] and quantum dot LEDs (QLEDs, FWHM : ~30nm)[48-51] (**Figure 1.5**).

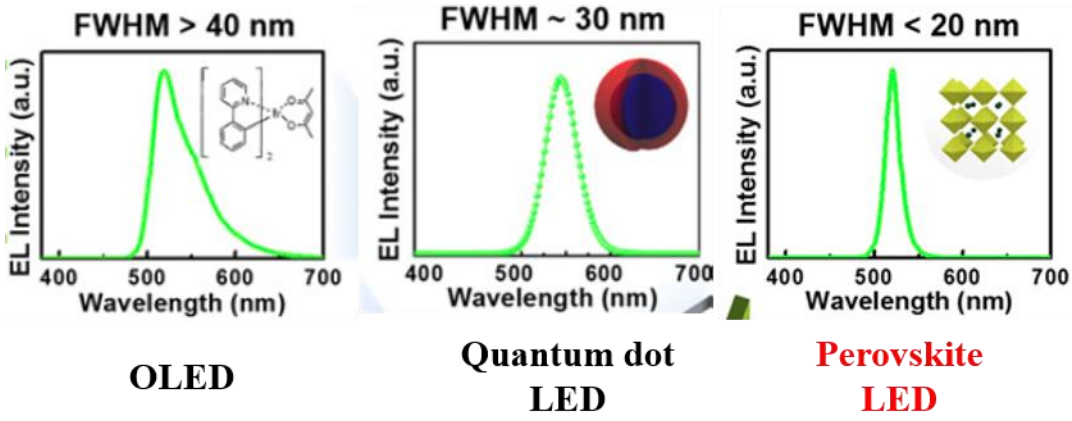

Figure 1.5. FWHM of organic emitters, inorganic quantum dot, perovskite[52]

Though the FHWM of photoluminescence (PL) changes according to the emission wavelength, the emission linewidth does not exceed 100meV. For example, ~12nm linewidth in the blue range ($CsPbCl_3$), ~20nm in green range ($CsPbBr_3$), and ~45nm in red range ($CsPbI_3$)[18]. The narrow FWHM allows the current color purity limits and enables ultra-high definition display implementation. The CIE color spaces were defined as the wavelength distribution of the electromagnetic visible spectrum and the perceptible area of the human eyes. As display and resolution technologies continue to evolve, 4K·UHD professional specifications have emerged to provide higher quality color values. The perovskite emitters reach the end of the edge, this is the widest range in compared to the previous display materials. **Figure 1.6** shows that the Perovskite meet wide color gamut based on narrow FWHM, which exceeds REC. 2020 standard by 103% and exceeds National Television System Committee (NTSC) standard by 138%[53]. The reason why the perovskite emission FWHM is narrow is not studied much, but it is reported that polar lead halide bonds cause Fröhlich interactions between charge carriers and polar longitudinal optical phonon mode such as in organic semiconductors GaAs. In most of the inorganic semiconductors, the emission FWHM is associated with the charge currieries and the phonons and impurities of the lattices. In addition, impurities or traps are not the cause of FWHM changes, since impurities of traps in low-crystallinity perovskites are non-radiative recombination with trap-assisted

recombination[19]. Therefore, perovskite materials show a narrow FWHM regardless of the quality of synthesis or fabrication method, unlike organic materials or quantum dot. (**Figure 1.7**) In particular, perovskite quantum dots can be mass-produced at room temperature because they exhibit constant FWHM values when the size of quantum dot is larger than Bohr radius, which is not affected by the quantum confinement effect[54, 55].

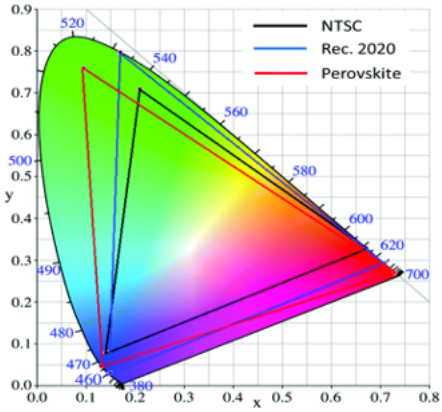

NTSC : Standard primary colors decided by National Television System Committee (NTSC) in 1953

High Color Accuracy

REC. 2020 : Standard primary colors decided by International Telecommunication Union (ITU) for ultra-high-definition television (UHDTV) in 2012

	White Point		Primary Colors					
	X_W	Y_W	X_R	Y_R	X_G	Y_G	X_B	Y_B
NTSC	0.310	0.316	0.67	0.33	0.21	0.71	0.14	0.08
REC. 2020	0.3127	0.3290	0.798	0.292	0.170	0.797	0.131	0.046

Figure 1.6. High color purity of Perovskite

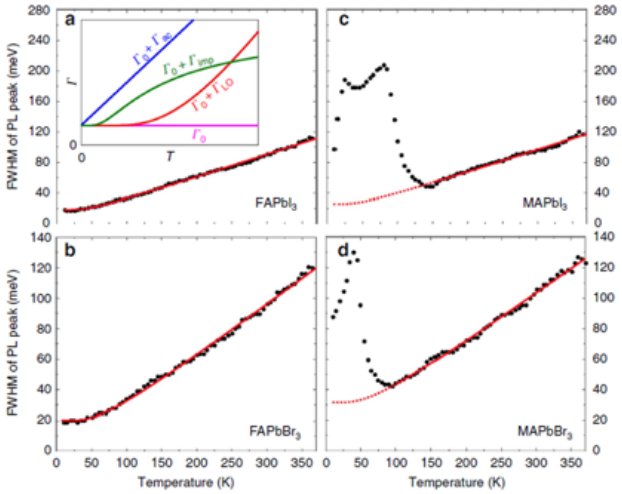

$$\Gamma(T) = \Gamma_0 + \Gamma_{ac} + \Gamma_{LO} + \Gamma_{imp}$$
$$= \Gamma_0 + \gamma_{ac} T + \gamma_{LO} N_{LO}(T) + \gamma_{imp} e^{-E_b/k_B T}.$$

Nat Commun. **2016**. 7, 11755.

Impurity can be negligible

Figure 1.7. Origin of narrow FHWM[19]

Although the luminescence linewidth of perovskite is intrinsic property, it is not easy to control, but some papers on narrow linewidth have been reported. Zhao et al. reported that the orientation of the perovskite crystal is related to the FWHM as well as affecting the charge transport. They have demonstrated an cation exchange techniques for conversion from layered structure (PEA_2PBBr_4) to 3D ($MAPbBr_3$) perovskite with highly aligned crystals. By changing the bulky PEA cation to MA cation, the electro luminescence (EL) linewidth shows about 20nm in the 3D $MAPbBr_3$ PeLEDs with general randomly 3D orientation, but the high-quality $MAPbBr_3$ grown using the layered template show the extremely narrow FWHM (15.3nm) (**Figure 1.8**)[56]. Ruddelsden-Popper perovskite films with multi quantum wells show relatively widely FWHM, however the perovskite films with pre-synthesized controlled the number of PbX_6 layer reported to maintain narrow FWHM[57].

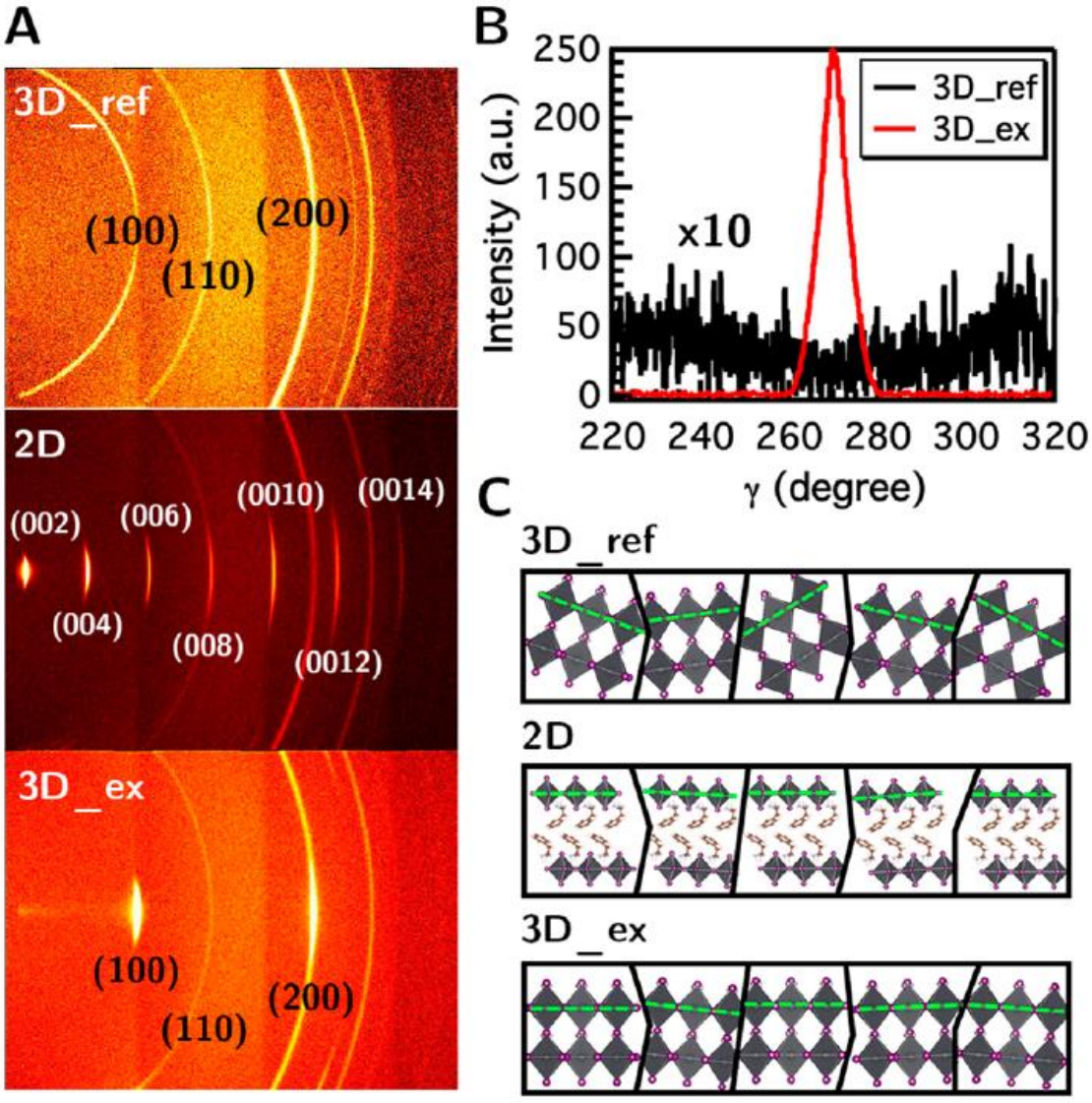

Figure 1.8. FWHM of high orientated perovskite film[56]

1.1.2 Bandgap tunability of Perovskite

Similar to other oxide perovskite, band gap of halide perovskites can be easily controlled by combining various A cation, B cation and X halide anions. The basic properties of the perovskite are governed by the characteristics of the bond of divalent metal cation (M) and X anion. The valence-band maximums (VBMs) are determined by an antibonding hybrid state of the M-*m*s (Pb: $m = 6$) and the X-*n*p ($n = 3$–5) orbitals in the M–X chains. The conduction-band minimums (CBMs) are determined by a non-bonding hybrid state of the M-*m*p (Pb: $m = 6$) and the X-*n*p ($n = 3$–5) orbitals (**Figure 1.10**).

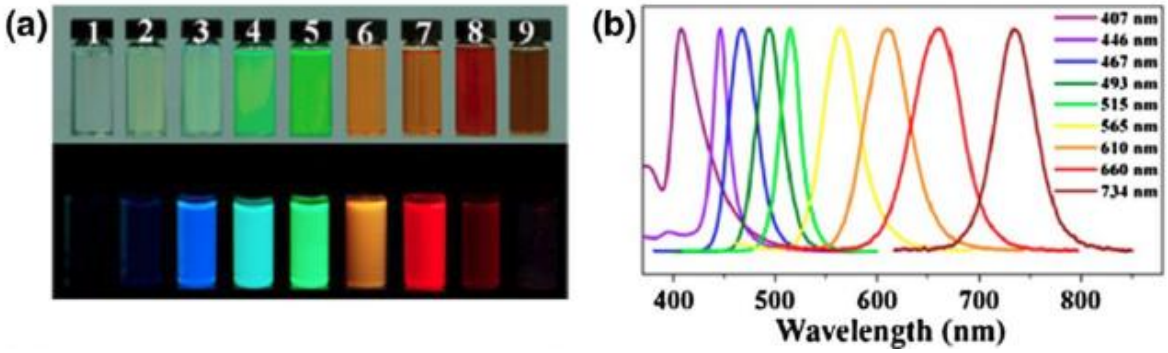

Figure 1.9. Optical photograph of mixed halide perovskite and PL spectra[58]

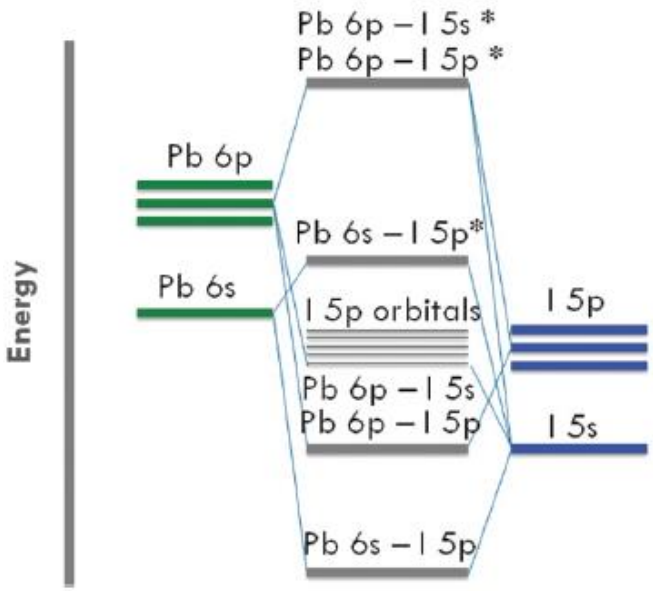

Figure 1.10. Energy diagram of PbI_6^{4-}

1.1.2.1 Influence of A cation

In the perovskite, the A site does not act an critical factor in composing the band gap, however it is known to play a role in balancing charge within the perovskite structure[59]. Nevertheless, it can affect the band gap by changing the MX_6 octahedron frame owing to the different size of A cation. The lattice of perovskite is increased when the cation is larger and smaller when it is smaller. And this affects the B-X bond length, which is an important link in determining the band gap. [60, 61].

Given a specific metal and halide, such as $APbI_3$, as long as the tolerance factor (t) is satisfied, only a relatively small size A cation is allowed to fit between corner-sharing metal halide octahedrons. When $t = 1$, to maintain cubic structure, the value of the ionic radius (R_A^+) cannot be larger than 2.6 Å. If the A cation size is too large, the 3D perovskite structure is difficult to maintain or a perovskite of 2D structure will be formed. Perovskite based on ethyl ammonium cation was previously explored in solar cells and was found to form a wider band gap perovskite due to the 2H type structure. So far, it has been demonstrated that small size A site cations such as K^+, Rb^+, Cs^+, methylammonium (MA^+) or formamidinium (FA^+) can make a 3D framework within the PbI_6 frame. Within the range of this comparison, the effective ionic radius follows a trend of $R_{Cs}^+ < R_{MA}^+ < R_{FA}^+$ as illustrated in **Figure. 1.11.** In summary, as the A site ion radius increases, the perovskite lattice would be expected to increase, the band gap reduce, causing a red-shift in the absorption onset. The inorganic Cs^+ has the relatively better stability than MA or FA cation. In the case of K^+ or Rb^+ ions, which are too small size, they are reported to be located at the grain boundary rather than in lattice (**Figure 1.12**)

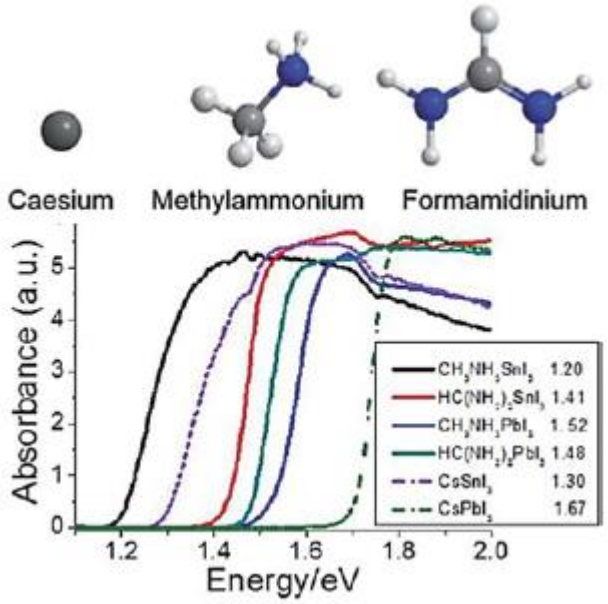

Figure 1.11. The atomic structure of A cation[62]

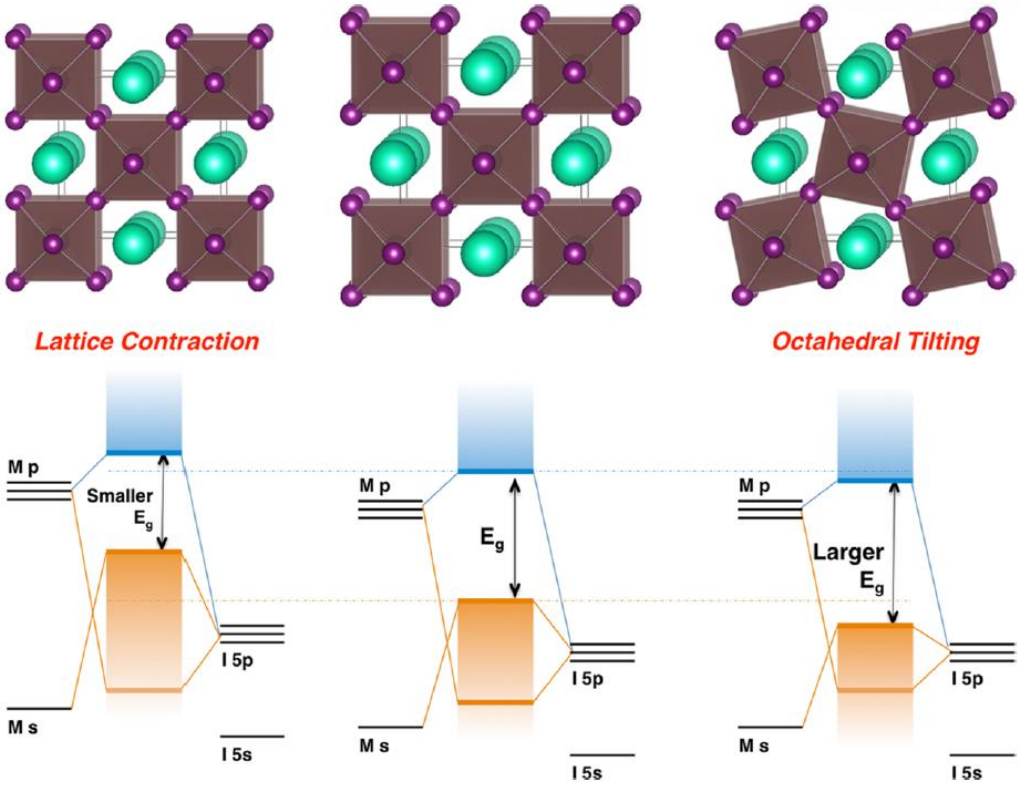

Figure 1.12. Change of energy diagram by A cation[63]

1.1.2.2 Influence of B metal cation

In the B site, numerous studies are limited to Pb(Ⅱ) cation in 3D perovskite. However, due to the environmental toxicity of Pb, another divalent metal ion are being studied to replace Pb. Although tin (Sn) or germanium (Ge) like group 14 element has been reported in a few papers, it is not easy to replace Pb due to the problem of strong oxidation state on exposure to air and slow charge mobility due to lattice mismatch[64-67]. The angle of the X-M-X bond has an important influence on the determination of the bandgap for each individual metal. Taking the structure of AMI_3(M = Pb^{2+}, Sn^{2+}, Ge^{2+}) as an example, the angles of M-I-M bridge are 155.19° for Pb, 159.61° for Sn, 166.27° for Ge[68]. As the size of the metal cation becomes larger, the strength of the covalent bond, which is a bond with the halide, becomes weaker. This means that the difference in electron negativity between the two atoms increase, so that the larger the metal ion size, the larger the band gap.

1.1.2.3 Influence of X halide anion

The halide anion of X site is the element that can control the band gap. In the mixed halide case, many studies have been carried out in order to meet the ideal bandgap for the tandem solar cell. The people have observed an increase in lattice constants with the increasing atomic size of the anions from Cl to Br to I, the emission spectra for perovskite shift to small band gap by changing the halide from Cl to Br and I[5, 60, 69-71]. The electronic states of perovskite are heavily influenced by halide elements. Such that a VBMs transition from 3p → 4p → 5p occurs for substitution of Cl → Br → I. This means that the ionization potential is lower (**Figure 1.13**)[72].

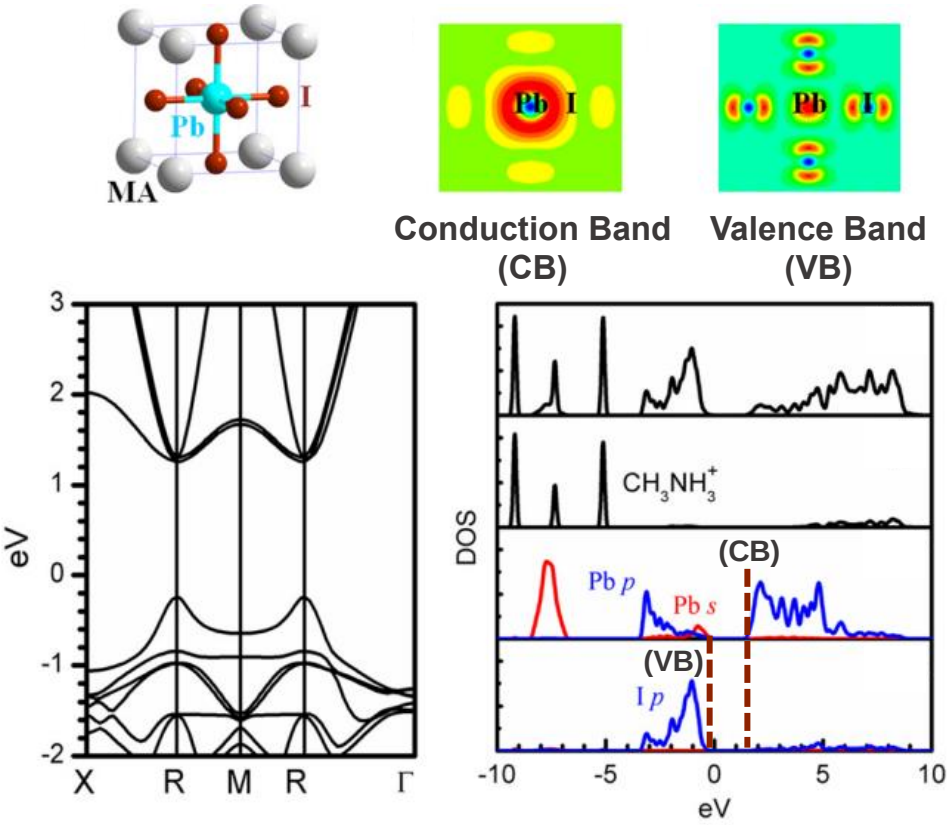

Figure 1.13. Change of energy diagram by halide X anion[63, 73]

1.1.3 PLQY characteristics of perovskite

Increasing radiative recombination in perovskite materials is a prerequisite for achieving a highly efficient optoelectronic devices. In particular, the solution-processed perovskite is not east to achieve high PLQE due to many defect sites on the surface and bulk. Also, the perovskite has low outcoupling efficiencies due to high refractive index of perovskite, so PLQE must be high for device performance improvement. Generally, the germinate electron-hole pairs generated by charge carrier injection or photoexcitation form free carriers or excitons. The binding energy of an exciton is a criterion for whether a geminate electron-hole pair exists as a free carrier or as an exciton. The perovskite forms Wannier-type excitons (**Figure 1.14**) with low exciton binding energy and high dielectric constant (e.g. 2-50meV for $CH_3NH_3PbI_3$) (**Figure1.15**).

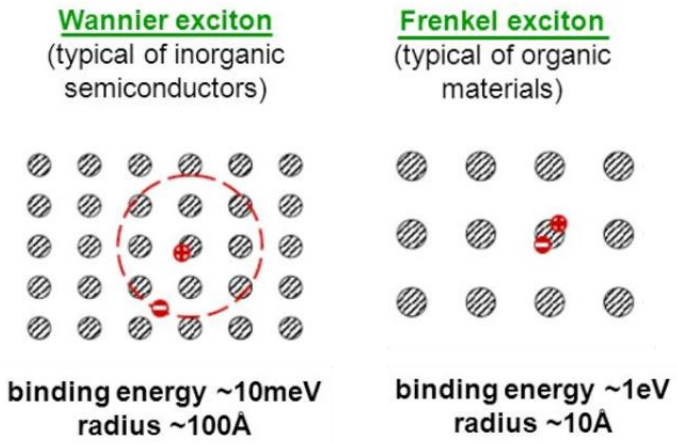

Figure 1.14. Wannier exciton and Frenkel exciton

$$E_b = \frac{\mu}{m_0 \varepsilon_r^2} R_H$$

Equation of Exciton binding energy

Dielectric constant	**Exciton binding energy**
Lead halide perovskite : 30~70	Lead halide perovskite : 30 ~ 100 meV
Organic material : 1~3	Organic material : 300 meV ~ 1 eV

Figure 1.15. Dielectric constant and exciton binding energy relations

Thus, most of the excitons are separated in to free charges at room temperature (RT). Charging trapping by trap states also induces the dissociation of excitons into free carriers and the nonradiative recombination pathway of free carriers and excitons, and thereby limits the luminescence efficiency at

low fluences. In the actual PeLEDs, radiative recombination complements trap-assisted non-radiative recombination and Auger recombination. (**Figure 1.16**)

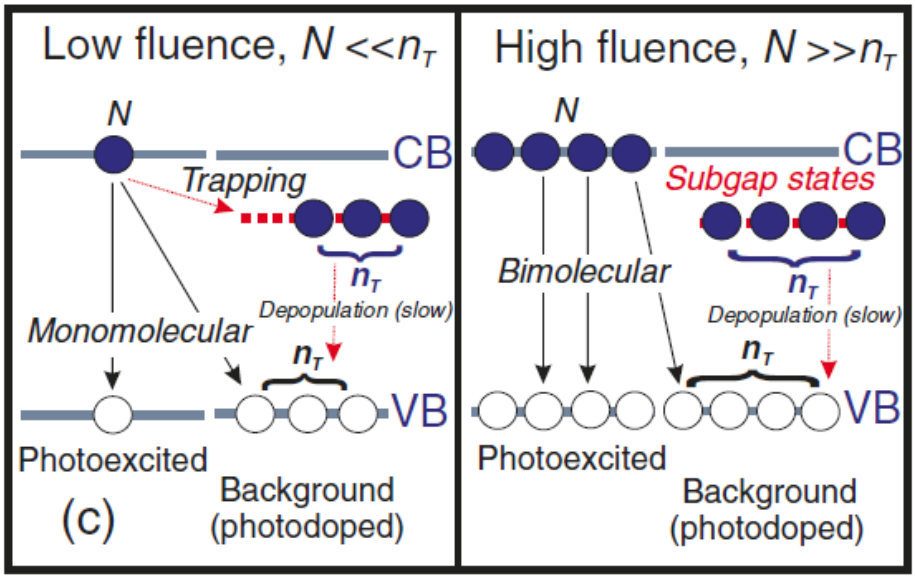

Figure 1.16. Schematic of trap limited recombination scenario[17]

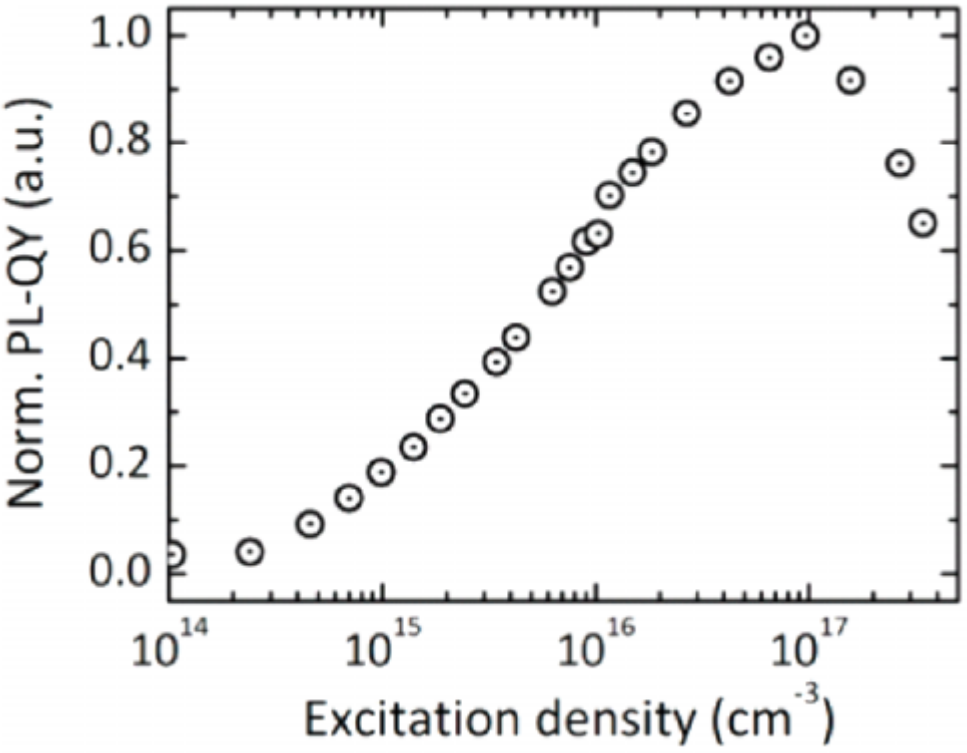

Figure 1.17. Power dependent quantum yield from low exciton binding energy[74]

However, if the excitation density exceeds 10^{20} cm^{-3}, the charge carriers are increased and the wavefunction is overlapped and the trap site is filled. (**Figure 1.17**) Therefore, more excitons are bounded than separated free carriers. Lowering the temperature below 190K deactivates the trap state and increases the ration of excitons to free carriers. The perovskite emitters are known as defect-tolerant semiconductor, and internal PLQEs show over 80% at high photo-excitation density or at low temperature. And perovskite films also have low PLQE value, *ie*, emission from interface between perovskite and air due to low out-coupling efficiency and photon recycling.

There are three mechanism known for charge-carrier recombination pathway in the perovskite. The charge-carrier density (n) over time is expressed by the following equation.

$$\frac{dn(t)}{dt} = -nk_1 - n^2k_2 - n^3k_3$$

Here, K_1, K_2 and K_3 are constants, indicating monomolecular recombination rate constant (trap mediate), bimolecular recombination rate constant and Auger rate const, respectively. In general 3D perovskite, only electron-hole bimolecular recombination is known as the radiative recombination, trap mediate and auger recombination must be avoided in order to increase luminescence efficiency.

In conclusion, perovskite's PLQE is not high due to the low exciton binding energy and the trap created by the solution process, but it can effectively improve the PLQE up to ~95% through various treatment such as small grain size (<10nm), multi-quantum well structure and defect passivation. Thus, the perovskite is the promising next generation of emitters in display and solid-state lighting.

1.1.4 Strategies for improving the luminescence of perovskite

1.1.4.1 Layered perovskite

The basic structure of 2 dimensional perovskite is as follows $A'_2A_{n-1}MX_{3n+1}$. To convert a 3D structure to a 2D structure, A'site generally are occupied by bulky long chain organic molecule. Where n represents the number of layers of PbX_6. The 2D structure of the complete plate (n=1) is represented by A_2MX_4, which is called a Ruddlesden-Popper perovskite. As the number of n increases, the BX6 layer grows along the <100> direction. The number of n is controlled by the stoichiometric molar raio between the bulky organic molecule and the A site molecule. The electronic and optical properties of 2D perovskites begin with a unique structure in which organic and inorganic components are oriented and assembled. They are considered multiple quantum well structures in which semi conductive inorganic sheets alternate periodically into insulating organic layers. (**Figure 1.18**).

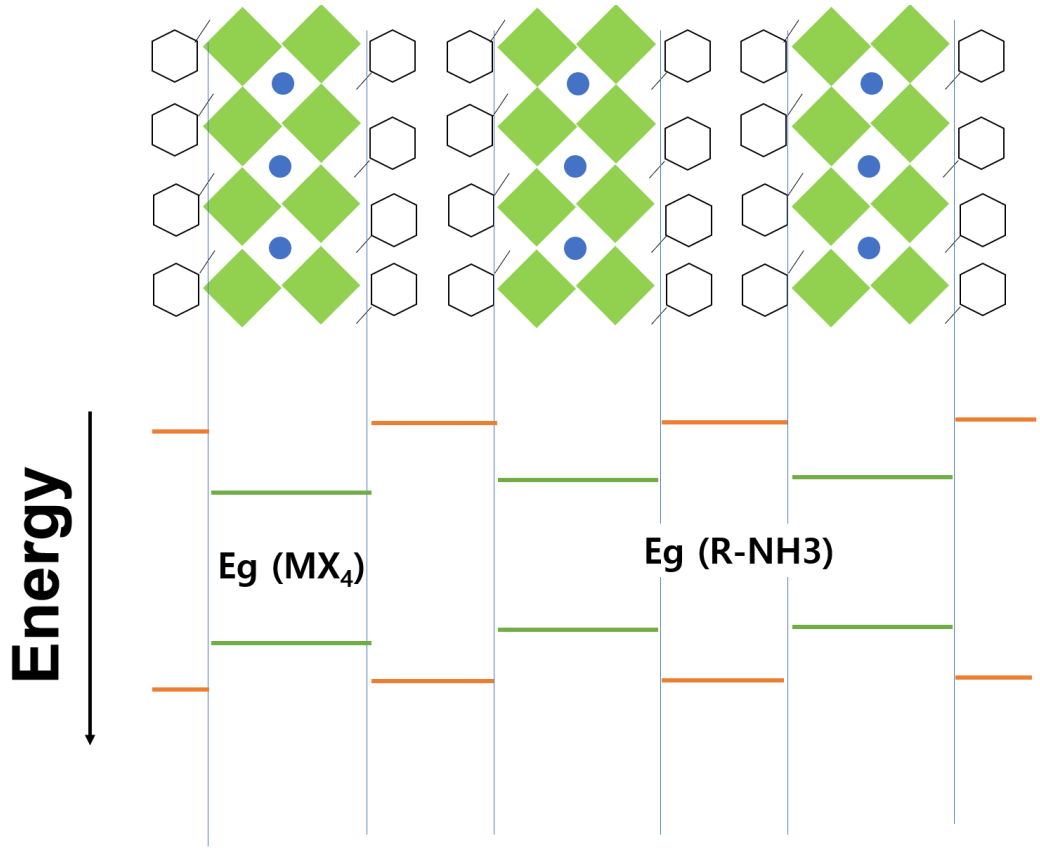

Figure 1.18. Schematic of the oriented 2D perovskite and corresponding band energy diagram

If a photon with energy greater than the band gap of the material is incident, the electron and hole will be in the conduction band and the valance band, respectively, and can form the bounded excitons. Because of the low dielectric constant of the bulky organic layer and the large bandgap, the generated

excitons are trapped in the inorganic well, with increased exciton binding energy on the order of hundreds of millivolts. In particular, the exciton binding energy can be directly controlled by exchanging the organic dielectric layer According to previous reports, the exciton binding energy of a typical metal halide perovskite is known to be several tens of meV. (**Figure 1.19**).

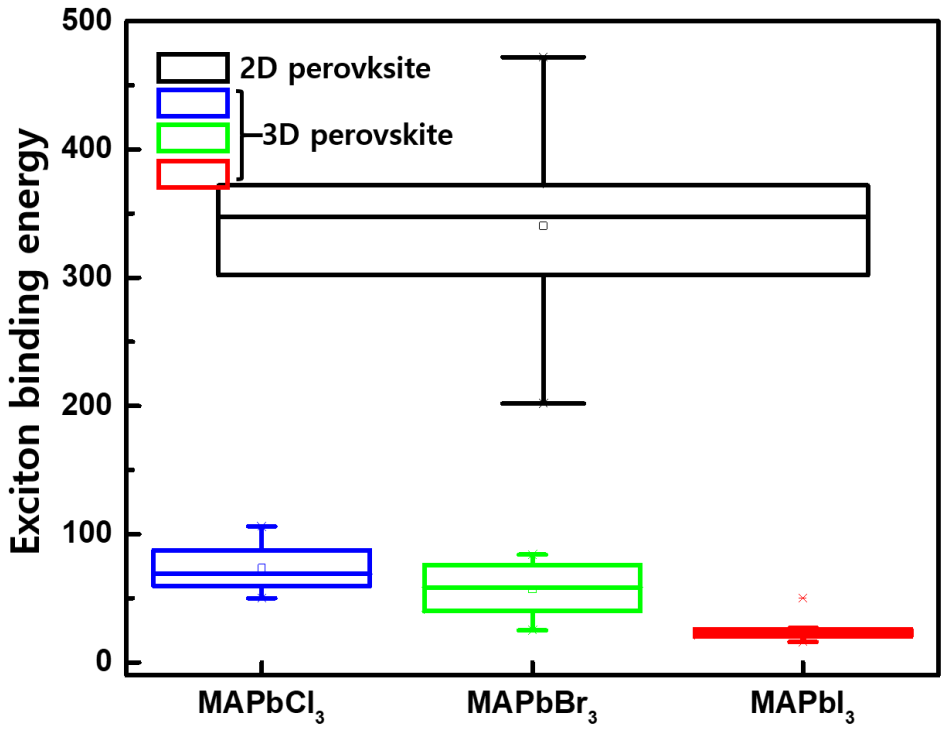

Figure 1.19. Exciton binding energy of 3D and 2D perovskite

Perovskite with a multi-quantum well structure gives another freedom in designing the luminescence properties, since the relative band alignment and the relative band alignment between the inorganic and organic components, will determine the overall material properties. An important feature of such a multiple quantum well structure is the naturally assembled nature of organic and inorganic salt precursor solutions, leading to thin films with high crystallinity, as can be clearly seen in the X-ray diffraction pattern of a series of spin-coated films of (C4H9NH3) 2PbX4 with different halide anions. In a quaisi-2D perovskite film with multi-quantum well of various bandgaps, the excited excitons are transferred to thin quantum well thickness layer, possibly with some Foster resonance energy mechanism. The concentrations of charge at low bandgap can be effective for radiative recombination due to the increased confinement effect. The group of Sargent et al. showed high efficiency near-infra red PeLEDs with an EQE of 8.8%, where bulk organic cation was implemented in to their perovskite layer to give quasi-2D layered structure (**Figure 1.20**).

Compared with the 3D perovskite, layered perovskites show improved photoluminescence quantum

yield, high exciton binding energy and high moisture stability.

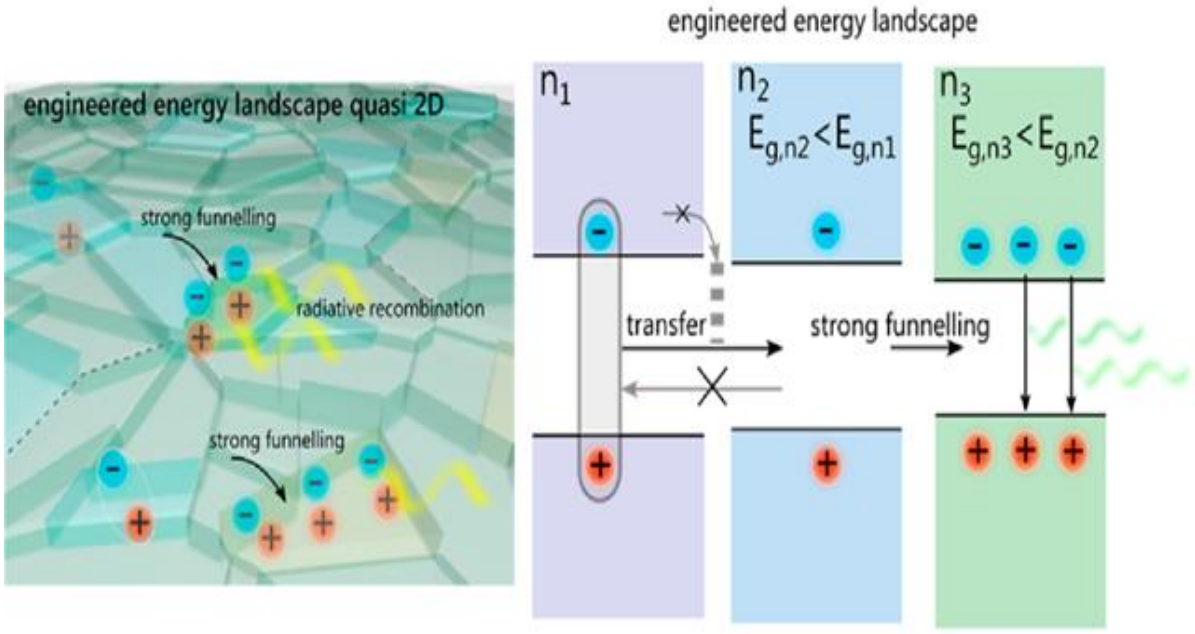

Figure 1.20. Energy cascade system in quasi 2D perovskite

1.1.4.2 Grain size control

Since the grain size of general 3D perovskite fabricated by solution process exceeds over 100nm, the excitons easily dissociated into free carriers. For effective radiative recombination of perovskite, the excitons must be confined in perovskite crystal, since the spatial confinement increases local carrier density and increases radiative recombination. To occur the quantum confinement of charge-carrier, the grain size of the perovskite should be smaller than the Bohr radius of perovskite. The typical of Bohr radius of perovskite have a radius~10nm, below which the electrons and holes do not exist as free carriers and form exciton, which allows monomolecular radiative recombination and can maximum luminous efficiency at low excitation density.

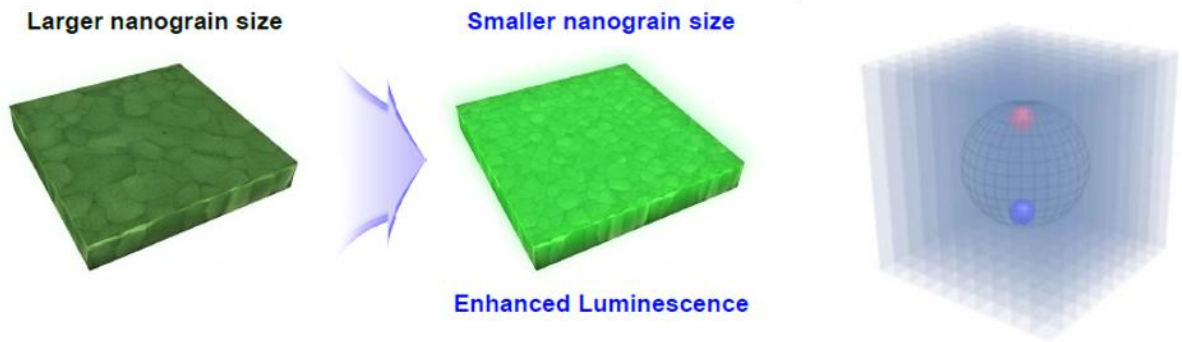

Figure 1.21. PLQE improvements due to charge confinement[4, 75]

Several methods have been proposed for effective exciton confinement. The simplest approach to improve the exciton confinement is to make the perovskite film thinner (< 20nm)[76], which is difficult to form a uniform perovskite films with full coverage because this method uses a ultra-low perovskite precursor concentration. Group of Lee et al. reported a method to uniform perovskite films of small grain size using nanocrystal pinning method and eliminated the factor of lowering the luminous efficiency by preventing the formation of metallic Pb atoms acting exciton quenching site through chemical quantitative control during thin film formation[4]. The most common way to make perovskite crystals smaller is though nanocrystals (NPs) synthesis. The perovskite NPs can effectively passivate surface defects, thus increasing luminous efficiency. Particularly, if the synthesized size is larger than the Bohr radius (> 10nm) the perovskite NPs have no wavelength variation due to size distribution unlike inorganic NPs. Therefore, perovskite NPs have the advantage of showing a monodispersed wavelength using the simple RT ligand assisted reprecipitation (LARP) method as well as hot-injection method. In addition, it is possible to achieve high PLQE using appropriate ligand search and synthesis condition control such as temperature, composition control and film deposition method. Template-assisted growth of perovskite NPs induces a quantum confinement effect by controlling the size of perovskite. Dirin et al. reported the perovskite NPs based on mesoporous SiO_2 templates. In this work,

they observed that the blue shift of emission peak due to the quantum confinement effect by fabricating the size of template porous diameter 2-10 nm, and showed PLQE up to ~90%.

1.2 Perovskite based Light-emitting Diodes

1.2.1 Structure of PeLEDs

PeLEDs are basically similar in structure to organic light-emitting diodes (OLEDs) and quantum-dot light-emitting diodes (QLEDs). They are usually made on a transparent substrates (plastic substrates or glass) coated with a transparent conductive oxide material (TCO) indium tin oxide (ITO) or fluorine doped tin oxide (FTO). PeLEDs has been explored in two types of device architecture, one is p-i-n and the other is n-i-p structure depending on the polarity of the bottom layers.

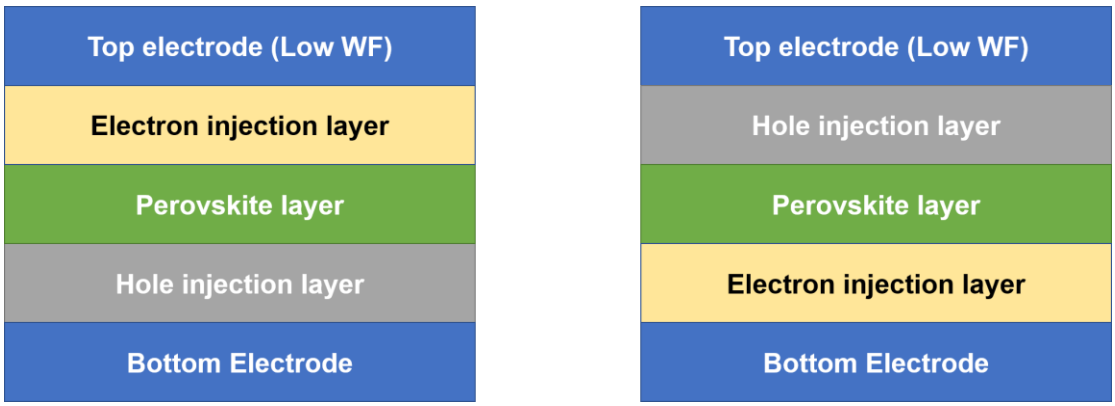

Figure 1.21. Structures of PeLEDs

The PeLEDs of the p-i-n structure, also referred to as the normal structure, use an ITO-coated glass as the anode, where holes are injected into the device. The poly(3,4-ethylenedioxythiophene) doped with polystyrene sulfonate (PEDOT:PSS), which is the organic charge transport layer, is widely used as a hole injection layers (HILs). The interlayer can be deposited on top of PEDOT:PSS to facilitate hole injection or for electron blocking to ensure charge confinement within the perovskite layer. The electron injection layers (EILs) are formed on the perovskite layer, effectively blocking the opposite injected hole and enabling effective electron injection. The electrons of this configuration are injected from the lowest unoccupied molecular orbital (LUMO) of the EIL materials into conduction band of perovskite layer, implying that the cathode should use low work function (WF) metal such as aluminum or silver. PeLEDs of normal p-i-n structure have been studied for various charge transport layers (CTLs) resulting from the development of OLEDs. However, since low WF cathode metal is easily oxidized to surrounding environment, advanced sealing technique is required and operational stability is limited.

In contrast, the inverted structure, n-i-p PeLEDs, can partially overcome the stability limits because high WF gold being the anode is more stable than low WF metal. This strategy has been carried out on

PeLEDs because OLEDs technology has been accomplished, and power conversion efficiency have been successfully recorded in perovskite solar cell. For effective electron injection, n type metal oxide such as ZnO or TiO_2 is used on the perovskite films as EILs. Owing to the chemical instability between active perovskite materials and ZnO, surface modified ZnO has been successfully used as EILs. This also reduces the electron injection barrier at the interface. The hole injection layer on the perovskite layer is mainly based on organic materials and the ohmic hole injection is possible by forming MoO_3 between the top gold electrode and the HIL layer.

1.2.2 Characterization of PeLEDs

PeLEDs are usually made up of a sandwich of emissive perovskite materials between the top and bottom conductive electrodes. When a bias is applied across the two electrodes, the electrons and holes pass through EILs and HILs, respectively, into the perovskite layer. Electrons enter the conduction band minimums of the perovskite through the LUMO levels or conduction band of the EIL and the hole is injected into the valance band of the perovskite through the HIL HOMO levels or valance band. The charge injection characteristics are affected by the energy levels and charge carrier mobility of charge injection layers. In addition, the bandgap of charge injection layer must be large enough to effectively confine injected charge carrier to the emissive layer.

Electroluminescence efficiency is the most important factor of performance of PeLEDs. The factors that measure the characteristic Factors that measure the characteristics of PeLEDs include luminance, current efficiency, external quantum efficiency (EQE), turn on voltage, and FWHM of emission wave length.

EQE is defined as the number of photon emitted from a diode / the number of electrons injected in to the diode, given by this equation

$$\eta_{EQE} = \eta_{outcoupling} \cdot \gamma \cdot \phi, \frac{\text{number of emitted electrons}}{\text{number of injection electrons}} \times 100$$

$$= \frac{\frac{\int_{380}^{780} Spectrum\,(\lambda)}{\frac{hc}{\lambda x 10\hat{}-9}} \cdot \pi \cdot Ad\lambda}{I/q} \times 100$$

$$= \frac{\pi \cdot A}{hc \times 10^{-9}/q} \frac{\int_{380}^{780} Spectrum\,(\lambda) \cdot \lambda d\lambda}{I} \times 100$$

(A : area, h : plank constant, c : light speed, q: electron charge)

Where η_{EQE} is out-coupling factor, γ is balanced charge injection factor, ϕ is related to radiative quantum efficiency. The out-coupling efficiency of perovskite is low due to significant waveguiding loss due to high refractive index. Recently, methods of reducing the optical loss by depositing thin or rough perovskite film. The suitable interfacial charge injection layers can increase the balanced charge injection factor. The radiative quantum efficiency can be achieved by increasing the defect passivation, charge confinement, and carrier density.

Current efficiency (cd/A) is defined as follows.

$$= \frac{Luminance(cd/m^2)}{Current\ density\ (mA/\ cm^2} \times 10^{-1}$$

Where cd is the base unit of luminous intensity in the international System of Units (SI). It means a light flux per unit solid angle of light emitted in a specific direction from a point light source. The one ordinary candle emitted one candela. Candela is a Latin word for candle. If the intensity of the emitted light relative to the injected current is counted, the efficiency also increases.

Power efficiency (lm/W) is defined as follows.

$$= \frac{\pi \times Luminancd(cd/m^2)}{Voltage(V) \times Current\ density\ (mA/cm^2)} \times 10^{-1}$$

The luminous efficiency is the value obtained by dividing the luminous flux by the power consumption. In the case of the same illumination, the luminous flux and the power consumption are constant. If the emission intensity is high at low voltage, the power efficiency is also increased.

The turn-on voltage close to the perovskite bandgap confirms how charge carriers are balanced injection into diode. PeLEDs of most p-i-n structures show a turn-on voltage of 3-4 V in the green region, and ~2 V for iodide base PeLEDs with organic charge transport layer. With the improved charge injection due to proper energy level alignment, the turn-on voltage can be reduced to ~2 V (green) or 1.5 V similar to perovskite bandgap.

FWHM is a term indicating the width of a function and is defined as the difference between two independent variable values which are half of the maximum value of the function. The FWHM is expressed in terms of energy (meV) and in wavelength (nm), and the half width of the perovskite is usually known as 100 meV.

Therefore, it is also important to increase the raiative efficiency of the perovskite film in order to realize a high-efficiency PeLED, but it is also important to increase the charge balance due to the effective charge injection from the contact layer.

1.2.3 Progress in PeLED efficiencies

The development of PeLEDs efficiency can be achieved by exploiting the research of progressive development of existing OLED and quantum dot LEDs and combining the materials, device structures and concepts established in this field with new perovskite active layers. The first report on electroluminescence from perovskite was published using using 2D structured perovskite thin film obtained by spin coating $(C_6H_5C_2H_4NH_3)_2PbI_4$ perovskite dissolved in acetonitrile solution [77]. The bulky phenethyl ammonium iodide cation lowers the perovskite dimension, which allows the formation of stable excitons with large exciton binding energies and allows intense photoluminescence at room temperature. However, the electroluminescence of the device was only observed when the device was driven under liquid nitrogen temperature. Under these conditions, luminance levels up to 10,000 cd/m2 at a current density of 20,000 A/m2, were obtained with an applied bias of 24 V. At room temperature, the initial electroluminescence of the PeLEDs with inverted structure ITO / TiO_2 / $CH_3NH_3PbI_{3-x}Cl_x$ / F8 / MoO_3 / Ag, was reported with a device structure as shown in **Figure 1.22**[16].

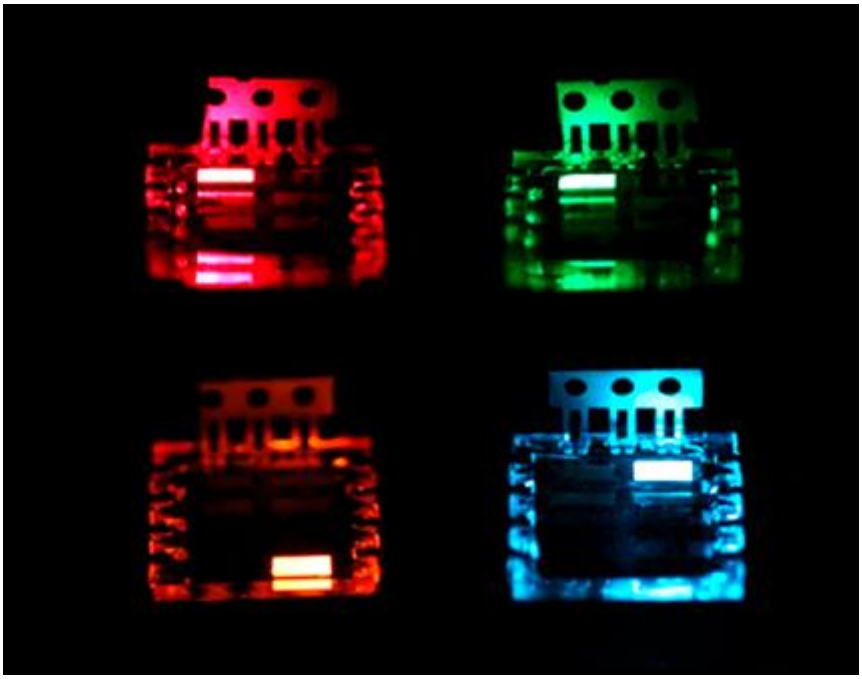

Figure 1.22. Electroluminescence spectra and image of perovskite LEDs[16]

This structure allows excellent charge injection to the infrared emission perovskite. Recently, Yuan et al. Reported an infrared PeLEDs of 8.8% EQE based on quasi-2D-perovskite using this structure [78]. However, this structure did not show a successful efficiency in structure due to the difficulty of charge injection into green or blue perovskites until the surface modification of the metal oxide layer was

introduced or a wider bandgap metal oxide was used. For example, Wang et al. Used ZnO nanocrystals to improve the disadvantages of ZnO being less thermally stable than perovskite and used polyethyleneimine (PEI) to modify the surface of the layer. This improved the morpholgy of the perovskite layer and reduced the energy barrier of the perovskite layer to electrons.

Compared with the conventional inverted-structure PeLEDs, the schematic diagram of the normal-type PeLEDs structure is shown in the **Figure 1.21**. Based on this normal structure, green and red PeLEDs, and later blue PeLEDs, were studied more actively than inverted-structure PeLEDs. Recently, Cho et al. reported a 8.53% EQE green PeLED, which is based on a modified standard structure with a self-organized conducting polymer to improve hole injection[79]. X. Yang et al. reported the defect passivated quasi-ed PeLED. They used $PEA_2(FAPbBr_3)_{n-1}PbBr_4$ (n=3) as the emitting layer for quasi-ed PeLEDs. The quasi-2d perovskite surface was passivated with trioctylphosphine oxide (TOPO) treatment. The result is a very high current efficiency (CE) of 62.4 cd A-1 and an EQE of 14.36%[24]. Recently, more than 20% EQE of PeLEDs studies have been reported using charge balanced core shell PeLEDs, enhanced outcoupling efficiency PeLEDs and polymer composite quasi-2D perovskite film. K. Lin et al. reported that mixed perovskite film with a pre-synthesized $CsPbBr_3$/MABr quasi-core/shell structure[80].

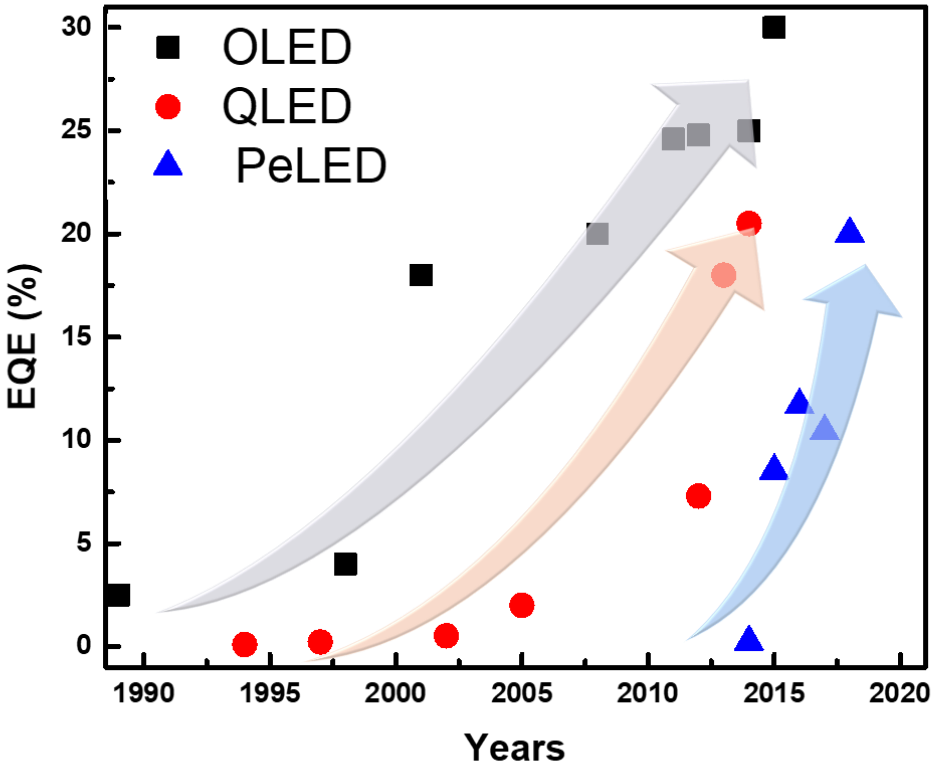

Figure 1.23. Progress in PeLED efficiencies

1.2.4 Stability issues of PeLED operation

Based on steady research, PeLEDs has demonstrated over 20% EQE in the last four years with composition and grain engineering, structural engineering and energy manipulation, but there is still a device operational stability problem. Unlike Perovskite solar cells, PeLEDs operating lifetime is still impractical if the device's lifetime exceeds 1000 hours due to continuous operation and exhibits device stability of less than 100 hours under constant electrical stress. By contrast, conventional QLEDs have a lifetime of 100-1000h when operating at bright brightness (1000 cdm-2). This still does not meet the stringent requirements of commercial displays above 10,000 h at high brightness above 3,000 cd m^{-2}. By contrast, the lifetime of a state-of-the-art OLED commercialized is between 1,000 and 100,000 hours. In the early-generation OLEDs, instability was triggered by burn-in due to the crystallization of the organic material, but device encapsulation and manufacturing optimization overcome stability issues. The origins of PeLEDs instability are connected between fundamental aspects such as the strong ionic character of perovskite, their low formation energy, and the electrochemistry occurring at the interface with consideration at the device level.

1.3 Reference

[1] H. Wu, C. Zhang, K. Ding, L. Wang, Y. Gao, J. Yang, *Organic Electronics* **2017**, 45, 302.

[2] N. J. Jeon, J. H. Noh, Y. C. Kim, W. S. Yang, S. Ryu, S. I. Seok, *Nature Materials* **2014**, 13, 897.

[3] N. Ahn, D.-Y. Son, I.-H. Jang, S. M. Kang, M. Choi, N.-G. Park, *Journal of the American Chemical Society* **2015**, 137, 8696.

[4] H. Cho, S. H. Jeong, M. H. Park, Y. H. Kim, C. Wolf, C. L. Lee, J. H. Heo, A. Sadhanala, N. Myoung, S. Yoo, S. H. Im, R. H. Friend, T. W. Lee, *Science* **2015**, 350, 1222.

[5] Y. H. Kim, H. Cho, J. H. Heo, T. S. Kim, N. Myoung, C. L. Lee, S. H. Im, T. W. Lee, *Advanced materials* **2015**, 27, 1248.

[6] Z. Xiao, R. A. Kerner, L. Zhao, N. L. Tran, K. M. Lee, T.-W. Koh, G. D. Scholes, B. P. Rand, *Nature Photonics* **2017**, 11, 108.

[7] S. D. Stranks, H. J. Snaith, *Nature Nanotechnology* **2015**, 10, 391.

[8] L. Dou, Y. Yang, J. You, Z. Hong, W.-H. Chang, G. Li, Y. Yang, *Nature Communications* **2014**, 5, 5404.

[9] C. Li, C. Han, Y. Zhang, Z. Zang, M. Wang, X. Tang, J. Du, *Solar Energy Materials and Solar Cells* **2017**, 172, 341.

[10] Y. Fang, J. Huang, *Advanced Materials* **2015**, 27, 2804.

[11] G. Xing, N. Mathews, S. S. Lim, N. Yantara, X. Liu, D. Sabba, M. Grätzel, S. Mhaisalkar, T. C. Sum, *Nature Materials* **2014**, 13, 476.

[12] S. D. Stranks, S. M. Wood, K. Wojciechowski, F. Deschler, M. Saliba, H. Khandelwal, J. B. Patel, S. J. Elston, L. M. Herz, M. B. Johnston, A. P. H. J. Schenning, M. G. Debije, M. K. Riede, S. M. Morris, H. J. Snaith, *Nano Letters* **2015**, 15, 4935.

[13] S. Yakunin, L. Protesescu, F. Krieg, M. I. Bodnarchuk, G. Nedelcu, M. Humer, G. De Luca, M. Fiebig, W. Heiss, M. V. Kovalenko, *Nature Communications* **2015**, 6, 8056.

[14] G. Nagamine, J. O. Rocha, L. G. Bonato, A. F. Nogueira, C. H. Brito Cruz, L. A. Padilha, "Size Dependent Ultra-low Upconverted Lasing Threshold in CsPbBr3 Perovskites Quantum Dots", presented at *Conference on Lasers and Electro-Optics*, San Jose, California, 2018/05/13, 2018.

[15] M. S. Alias, Z. Liu, A. Al-atawi, T. K. Ng, T. Wu, B. S. Ooi, *Opt. Lett.* **2017**, 42, 3618.

[16] Z.-K. Tan, R. S. Moghaddam, M. L. Lai, P. Docampo, R. Higler, F. Deschler, M. Price, A. Sadhanala, L. M. Pazos, D. Credgington, F. Hanusch, T. Bein, H. J. Snaith, R. H. Friend, *Nature Nanotechnology* **2014**, 9, 687.

[17] S. D. Stranks, V. M. Burlakov, T. Leijtens, J. M. Ball, A. Goriely, H. J. Snaith, *Physical Review Applied* **2014**, 2, 034007.

[18] L. Protesescu, S. Yakunin, M. I. Bodnarchuk, F. Krieg, R. Caputo, C. H. Hendon, R. X. Yang,

A. Walsh, M. V. Kovalenko, *Nano Letters* **2015**, 15, 3692.

[19] A. D. Wright, C. Verdi, R. L. Milot, G. E. Eperon, M. A. Pérez-Osorio, H. J. Snaith, F. Giustino, M. B. Johnston, L. M. Herz, *Nature Communications* **2016**, 7, 11755.

[20] J. S. Manser, J. A. Christians, P. V. Kamat, *Chemical Reviews* **2016**, 116, 12956.

[21] T. J. Jacobsson, M. Pazoki, A. Hagfeldt, T. Edvinsson, *The Journal of Physical Chemistry C* **2015**, 119, 25673.

[22] G. Kieslich, S. Sun, A. K. Cheetham, *Chemical Science* **2015**, 6, 3430.

[23] S. Lee, J. H. Park, Y. S. Nam, B. R. Lee, B. Zhao, D. Di Nuzzo, E. D. Jung, H. Jeon, J.-Y. Kim, H. Y. Jeong, R. H. Friend, M. H. Song, *ACS Nano* **2018**, 12, 3417.

[24] X. Yang, X. Zhang, J. Deng, Z. Chu, Q. Jiang, J. Meng, P. Wang, L. Zhang, Z. Yin, J. You, *Nature Communications* **2018**, 9, 570.

[25] X. Liu, X. Guo, Y. Lv, Y. Hu, Y. Fan, J. Lin, X. Liu, X. Liu, *Advanced Optical Materials* **2018**, 0, 1801245.

[26] S. Lee, D. B. Kim, I. Hamilton, M. Daboczi, Y. S. Nam, B. R. Lee, B. Zhao, C. H. Jang, R. H. Friend, J. S. J. A. S. Kim, **2018**, 1801350.

[27] B. Zhao, S. Bai, V. Kim, R. Lamboll, R. Shivanna, F. Auras, J. M. Richter, L. Yang, L. Dai, M. Alsari, X.-J. She, L. Liang, J. Zhang, S. Lilliu, P. Gao, H. J. Snaith, J. Wang, N. C. Greenham, R. H. Friend, D. Di, *Nature Photonics* **2018**, 12, 783.

[28] S. A. Kulkarni, G. Han, K. S. Tan, S. G. Mhaisalkar, N. Mathews, *Current Opinion in Electrochemistry* **2018**.

[29] J. Woo Choi, H. C. Woo, X. Huang, W.-G. Jung, B.-J. Kim, S.-W. Jeon, S.-Y. Yim, J.-S. Lee, C.-L. Lee, *Nanoscale* **2018**, 10, 13356.

[30] F. Di Stasio, I. Ramiro, Y. Bi, S. Christodoulou, A. Stavrinadis, G. Konstantatos, *Chemistry of Materials* **2018**, 30, 6231.

[31] S.-H. Turren-Cruz, M. Saliba, M. T. Mayer, H. Juárez-Santiesteban, X. Mathew, L. Nienhaus, W. Tress, M. P. Erodici, M.-J. Sher, M. G. Bawendi, M. Grätzel, A. Abate, A. Hagfeldt, J.-P. Correa-Baena, *Energ Environ Sci* **2018**, 11, 78.

[32] D. H. Kim, J. Park, Z. Li, M. Yang, J.-S. Park, I. J. Park, J. Y. Kim, J. J. Berry, G. Rumbles, K. Zhu, *Advanced Materials* **2017**, 29, 1606831.

[33] H. Oga, A. Saeki, Y. Ogomi, S. Hayase, S. Seki, *Journal of the American Chemical Society* **2014**, 136, 13818.

[34] M. M. Tavakoli, L. Gu, Y. Gao, C. Reckmeier, J. He, A. L. Rogach, Y. Yao, Z. Fan, *Scientific Reports* **2015**, 5, 14083.

[35] M. R. Leyden, M. V. Lee, S. R. Raga, Y. Qi, *Journal of Materials Chemistry A* **2015**, 3, 16097.

[36] M. R. Leyden, L. K. Ono, S. R. Raga, Y. Kato, S. Wang, Y. Qi, *Journal of Materials Chemistry A* **2014**, 2, 18742.

[37] A. T. Mallajosyula, K. Fernando, S. Bhatt, A. Singh, B. W. Alphenaar, J.-C. Blancon, W. Nie, G. Gupta, A. D. Mohite, *Applied Materials Today* **2016**, 3, 96.

[38] W. Nie, H. Tsai, R. Asadpour, J.-C. Blancon, A. J. Neukirch, G. Gupta, J. J. Crochet, M. Chhowalla, S. Tretiak, M. A. Alam, H.-L. Wang, A. D. Mohite, *Science* **2015**, 347, 522.

[39] J. C. Yu, D. W. Kim, D. B. Kim, E. D. Jung, J. H. Park, A.-Y. Lee, B. R. Lee, D. Di Nuzzo, R. H. Friend, M. H. Song, *Advanced Materials* **2016**, 28, 6906.

[40] J. Liu, C. Gao, X. He, Q. Ye, L. Ouyang, D. Zhuang, C. Liao, J. Mei, W. Lau, *ACS Applied Materials & Interfaces* **2015**, 7, 24008.

[41] S. R. Raga, M.-C. Jung, M. V. Lee, M. R. Leyden, Y. Kato, Y. Qi, *Chemistry of Materials* **2015**, 27, 1597.

[42] J. C. Yu, D. B. Kim, G. Baek, B. R. Lee, E. D. Jung, S. Lee, J. H. Chu, D.-K. Lee, K. J. Choi, S. Cho, M. H. Song, *Advanced Materials* **2015**, 27, 3492.

[43] N. Cheng, P. Liu, S. Bai, Z. Yu, W. Liu, S.-S. Guo, X.-Z. Zhao, *Journal of Power Sources* **2016**, 319, 111.

[44] J. C. Yu, D. B. Kim, E. D. Jung, B. R. Lee, M. H. Song, *Nanoscale* **2016**, 8, 7036.

[45] C. W. Tang, S. A. VanSlyke, C. H. Chen, *Journal of Applied Physics* **1989**, 65, 3610.

[46] C. Adachi, M. A. Baldo, M. E. Thompson, S. R. Forrest, *Journal of Applied Physics* **2001**, 90, 5048.

[47] Y. L. Chang, Z. B. Wang, M. G. Helander, J. Qiu, D. P. Puzzo, Z. H. Lu, *Organic Electronics* **2012**, 13, 925.

[48] S. Coe-Sullivan, *Nature Photonics* **2009**, 3, 315.

[49] S. Coe-Sullivan, J. S. Steckel, W. K. Woo, M. G. Bawendi, V. Bulović, *Advanced Functional Materials* **2005**, 15, 1117.

[50] M. C. Schlamp, X. Peng, A. P. Alivisatos, *Journal of Applied Physics* **1997**, 82, 5837.

[51] S. Coe, W.-K. Woo, M. Bawendi, V. Bulović, *Nature* **2002**, 420, 800.

[52] Y.-H. Kim, H. Cho, T.-W. Lee, *Proceedings of the National Academy of Sciences* **2016**, 113, 11694.

[53] D. Wang, D. Wu, D. Dong, W. Chen, J. Hao, J. Qin, B. Xu, K. Wang, X. Sun, *Nanoscale* **2016**, 8, 11565.

[54] X. Li, Y. Wu, S. Zhang, B. Cai, Y. Gu, J. Song, H. Zeng, *Advanced Functional Materials* **2016**, 26, 2435.

[55] S. Sun, D. Yuan, Y. Xu, A. Wang, Z. Deng, *ACS Nano* **2016**, 10, 3648.

[56] T. Zhao, H. Liu, M. E. Ziffer, A. Rajagopal, L. Zuo, D. S. Ginger, X. Li, A. K. Y. Jen, *ACS Energy Letters* **2018**, 3, 1662.

[57] J. Si, Y. Liu, Z. He, H. Du, K. Du, D. Chen, J. Li, M. Xu, H. Tian, H. He, D. Di, C. Lin, Y. Cheng, J. Wang, Y. Jin, *ACS Nano* **2017**, 11, 11100.

[58] F. Zhang, H. Zhong, C. Chen, X.-g. Wu, X. Hu, H. Huang, J. Han, B. Zou, Y. Dong, *ACS Nano* **2015**, 9, 4533.

[59] I. Borriello, G. Cantele, D. Ninno, *Physical Review B* **2008**, 77, 235214.

[60] J. H. Noh, S. H. Im, J. H. Heo, T. N. Mandal, S. I. Seok, *Nano Letters* **2013**, 13, 1764.

[61] S. A. Kulkarni, T. Baikie, P. P. Boix, N. Yantara, N. Mathews, S. Mhaisalkar, *Journal of Materials Chemistry A* **2014**, 2, 9221.

[62] C. C. Stoumpos, C. D. Malliakas, M. G. Kanatzidis, *Inorganic Chemistry* **2013**, 52, 9019.

[63] R. Prasanna, A. Gold-Parker, T. Leijtens, B. Conings, A. Babayigit, H.-G. Boyen, M. F. Toney, M. D. McGehee, *Journal of the American Chemical Society* **2017**, 139, 11117.

[64] D. B. Mitzi, *Chemistry of Materials* **1996**, 8, 791.

[65] G. C. Papavassiliou, I. B. Koutselas, *Synthetic Metals* **1995**, 71, 1713.

[66] L.-y. Huang, W. R. L. Lambrecht, *Physical Review B* **2013**, 88, 165203.

[67] D. Sabba, H. K. Mulmudi, R. R. Prabhakar, T. Krishnamoorthy, T. Baikie, P. P. Boix, S. Mhaisalkar, N. Mathews, *The Journal of Physical Chemistry C* **2015**, 119, 1763.

[68] J. L. Knutson, J. D. Martin, D. B. Mitzi, *Inorganic Chemistry* **2005**, 44, 4699.

[69] H. Ayatullahah, G. Murtaza, S. Muhammad, S. Naeem, M. Khalid, A. Manzar, *Acta Phys. Polym* **2013**, 124, 102.

[70] A. Kojima, K. Teshima, Y. Shirai, T. Miyasaka, *Journal of the American Chemical Society* **2009**, 131, 6050.

[71] J.-H. Im, C.-R. Lee, J.-W. Lee, S.-W. Park, N.-G. Park, *Nanoscale* **2011**, 3, 4088.

[72] T. Krishnamoorthy, H. Ding, C. Yan, W. L. Leong, T. Baikie, Z. Zhang, M. Sherburne, S. Li, M. Asta, N. Mathews, S. G. Mhaisalkar, *Journal of Materials Chemistry A* **2015**, 3, 23829.

[73] W.-J. Yin, T. Shi, Y. Yan, *Applied Physics Letters* **2014**, 104, 063903.

[74] V. D'Innocenzo, A. R. Srimath Kandada, M. De Bastiani, M. Gandini, A. Petrozza, *Journal of the American Chemical Society* **2014**, 136, 17730.

[75] X. Gong, O. Voznyy, A. Jain, W. Liu, R. Sabatini, Z. Piontkowski, G. Walters, G. Bappi, S. Nokhrin, O. Bushuyev, M. Yuan, R. Comin, D. McCamant, S. O. Kelley, E. H. Sargent, *Nature Materials* **2018**, 17, 550.

[76] D. N. Congreve, M. C. Weidman, M. Seitz, W. Paritmongkol, N. S. Dahod, W. A. Tisdale, *ACS Photonics* **2017**, 4, 476.

[77] M. Era, S. Morimoto, T. Tsutsui, S. Saito, *Applied Physics Letters* **1994**, 65, 676.

[78] M. Yuan, L. N. Quan, R. Comin, G. Walters, R. Sabatini, O. Voznyy, S. Hoogland, Y. Zhao, E. M. Beauregard, P. Kanjanaboos, Z. Lu, D. H. Kim, E. H. Sargent, *Nat Nanotechnol* **2016**, 11, 872.

[79] L. Zhang, X. Yang, Q. Jiang, P. Wang, Z. Yin, X. Zhang, H. Tan, Y. Yang, M. Wei, B. R. Sutherland, E. H. Sargent, J. You, *Nature Communications* **2017**, 8, 15640.

[80] K. Lin, J. Xing, L. N. Quan, F. P. G. de Arquer, X. Gong, J. Lu, L. Xie, W. Zhao, D. Zhang, C.

Yan, W. Li, X. Liu, Y. Lu, J. Kirman, E. H. Sargent, Q. Xiong, Z. Wei, *Nature* **2018**, 562, 245.

[81] K. Galkowski, A. Mitioglu, A. Miyata, P. Plochocka, O. Portugall, G. E. Eperon, J. T. W. Wang, T. Stergiopoulos, S. D. Stranks, H. J. Snaith, R. J. Nicholas, *Energ Environ Sci* **2016**, 9, 962.

[82] A. Miyata, A. Mitioglu, P. Plochocka, O. Portugall, J. T. W. Wang, S. D. Stranks, H. J. Snaith, R. J. Nicholas, *Nat Phys* **2015**, 11, 582.

[83] B. R. Lee, E. D. Jung, Y. S. Nam, M. Jung, J. S. Park, S. Lee, H. Choi, S.-J. Ko, N. R. Shin, Y.-K. Kim, S. O. Kim, J. Y. Kim, H.-J. Shin, S. Cho, M. H. Song, *Advanced Materials* **2013**, 26, 494.

[84] B. R. Lee, S. Lee, J. H. Park, E. D. Jung, J. C. Yu, Y. S. Nam, J. Heo, J.-Y. Kim, B.-S. Kim, M. H. Song, *Advanced Materials* **2015**, 27, 3553.

[85] B. R. Lee, E. D. Jung, J. S. Park, Y. S. Nam, S. H. Min, B.-S. Kim, K.-M. Lee, J.-R. Jeong, R. H. Friend, J.-S. Kim, S. O. Kim, M. H. Song, *Nature Communications* **2014**, 5, 4840.

[86] X. Zhang, H. Lin, H. Huang, C. Reckmeier, Y. Zhang, W. C. H. Choy, A. L. Rogach, *Nano Letters* **2016**, 16, 1415.

[87] A. S. Subbiah, A. Halder, S. Ghosh, N. Mahuli, G. Hodes, S. K. Sarkar, *The Journal of Physical Chemistry Letters* **2014**, 5, 1748.

[88] X. Zhou, J. Blochwitz, M. Pfeiffer, A. Nollau, T. Fritz, K. Leo, *Advanced Functional Materials* **2001**, 11, 310.

[89] Y.-K. Chih, J.-C. Wang, R.-T. Yang, C.-C. Liu, Y.-C. Chang, Y.-S. Fu, W.-C. Lai, P. Chen, T.-C. Wen, Y.-C. Huang, C.-S. Tsao, T.-F. Guo, *Advanced Materials* **2016**, 28, 8687.

[90] S. Lee, D. B. Kim, I. Hamilton, M. Daboczi, Y. S. Nam, B. R. Lee, B. Zhao, C. H. Jang, R. H. Friend, J.-S. Kim, M. H. Song, *Advanced Science* **2018**, 5, 1801350.

[91] W. Nie, H. Tsai, J.-C. Blancon, F. Liu, C. C. Stoumpos, B. Traore, M. Kepenekian, O. Durand, C. Katan, S. Tretiak, J. Crochet, P. M. Ajayan, M. Kanatzidis, J. Even, A. D. Mohite, *Advanced Materials* **2017**, 30, 1703879.

[92] P. Liu, X. Liu, L. Lyu, H. Xie, H. Zhang, D. Niu, H. Huang, C. Bi, Z. Xiao, J. Huang, Y. Gao, *Applied Physics Letters* **2015**, 106, 193903.

[93] M.-H. Park, S.-H. Jeong, H.-K. Seo, C. Wolf, Y.-H. Kim, H. Kim, J. Byun, J. S. Kim, H. Cho, T.-W. Lee, *Nano Energy* **2017**, 42, 157.

[94] S. Zhuang, X. Ma, D. Hu, X. Dong, B. Zhang, *Ceramics International* **2018**, 44, 4685.

Chapter 2. Improved performance of perovskite light-emitting diodes using a PEDOT:PSS and MoO_3 composite layer

2.1 Research back ground

Over the past few years, organic–inorganic hybrid perovskite materials have received significant amounts of attention due to their excellent properties such as high photoluminescence quantum efficiency (PLQE) of 70% at low temperatures, a narrow emission spectrum, tunability of the band-gap, excellent charge carrier mobility, and easy solution processing.[1–8] In addition, inorganic cesium lead halide perovskite ($CsPbX_3$) nanocrystals have been studied intensively due to their superior properties such as high PLQE levels reaching 95% at room temperature and tunability of the emission wavelength depending on the type of halide.[9–12] Thus, these perovskite materials are promising in light-emitting diodes (LEDs), solar cells, photodetectors, and lasing applications.[13–17] The remarkable and rapid improvement of the external quantum efficiency (EQE) of perovskite LEDs (PeLEDs) up to 8.5% for green emission was recently realized, revealing the great potential of these devices for use in low-cost displays and lighting applications.[18] Recently, PeLEDs based on perovskite nanocrystals have made impressive progress in just a few years with the maximum EQE jumping from 0.12% to 3.8%.[12,19,20] The morphological control of perovskite film and themaximized recombination of charge carriers via the matching of the energy barriers between the contacts are critical to achieving highly efficient PeLEDs.[21–24] The addition of HBr in the perovskite precursor solution[22] and the fabrication of composite films which mixes of polymer and perovskite materials in a solution[25–27] have been widely adopted to obtain uniform perovskite films, leading to improved PeLED efficiency. In this context, Cho et al. reported highly efficient PeLEDs by manipulating the morphology of methyl ammonium lead tribromide ($CH_3NH_3PbBr_3$) through nanocrystal pinning[20] and modifying the work function of the hole transport layer (HTL) to fabricate a composite layer of PEDOT:PSS and with perfluorinated polymeric acid, which reduced the hole-injection barrier and balanced the injection of charge carriers.[28] Moreover, Zhang et al. reported that the device efficiency of perovskite nanocrystal LEDs have been significantly enhanced by introducing a perfluorinated ionomer (PFI) between the PEDOT:PSS and perovskite layers due to the improvement of the hole injection efficiency.

2.2 Experimental

Materials

The methyl ammonium bromide (MABr) was synthesized as described by previous reported. The SPW-111 polymer (white copolymer) was purchased from Merck Co. All reagent were used as purchased without further purification

PEDOT:MoO3 composite solution

PEDOT:MoO3 composite solution was realized by following process. A water dispersion PEDOT:PSS (AI 4083, Celvios) was filtered by 0.45 μm hydrophilic filter (PVDF filter), and then ammonium molybdate (NH4)2MoO4 (Sigma Aldrich) powder was added into PEDOT:PSS dispersion varying weight percent ratio from 0.001 wt.% to 0.007 wt.% under stirring.

Device fabrication

ITO/glass substrates were cleaned in sonication bath of distilled water, acetone, isopropyl alcohol, respectively for 10 min. And then treated UV-ozone for 10 min. PEDOT:PSS and PEDOT:MoO3 composite solution were spin-coated onto ITO/glass substrates as HTL and subsequently annealed at 145 oC for 10 min. The perovskite precursor (37.8 wt.%) with an aqueous HBr (48 wt.%) solution were spin-coated onto the PEDOT:PSS, PEDOT:MoO3-coated ITO/glass substrates at 3,000 rpm for 60 s and subsequently annealed at 60 oC for 2 hr under nitrogen (N2) atmosphere. The electron transport layer was spin-coated from SPW-111 dissolved in chlorobenzene. Finally, LiF (1 nm) and silver (80 nm) were deposited by the vacuum thermal evaporation method using a 5-pixel mask. The devices were encapsulated and legged before testing.

Characterisation of PEDOT:MoO3 composite film and PeLEDs

The PeLEDs tested using a keithely 2400 source measurement unit and a Konica Minolta spectroradiometer (CS-2000, Minolta Co.) under ambient air conditions. To observe morphology of MAPbBr3 films on the PEDOT:PSS and PEDOT:MoO3 composite layer were measured via scanning electron microscopy. The surface morphology of PEDOT:PSS and PEDOT:MoO3 composite layers was measured using atomic force microscopy (DI-3100, Veeco Co.). XPS and UPS spectra of PEDOT:MoO3 composite layer were conducted using ESCALAB 250XI (Thermo Fisher Scientific Co.)

2.3 Result and discussion

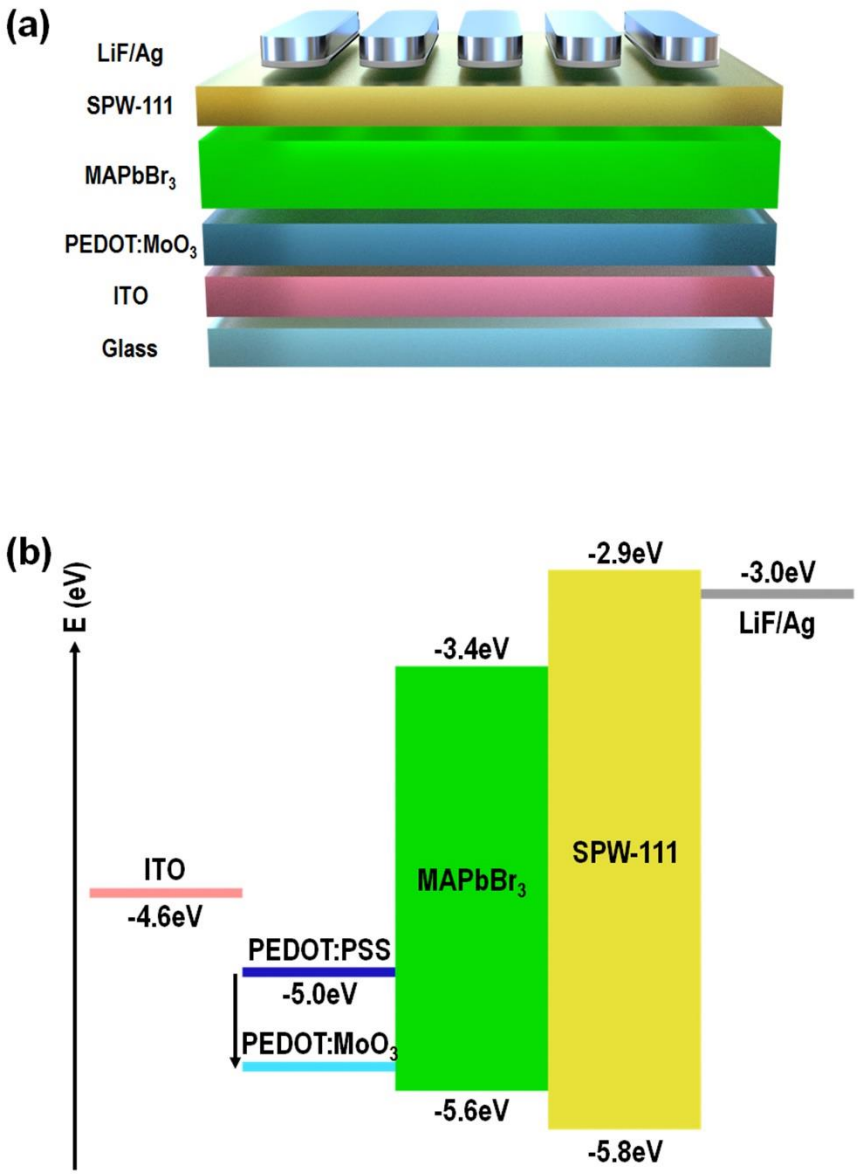

Figure 2.1 schematic of (a) PeLEDs device structure and (b) the energy levels diagram of each layer.

Figure 2.1 describe the device structure of PeLEDs (ITO/PEDOT:MoO_3/$MAPbBr_3$/SPW-111/LiF/Ag), which consisted of ITO as transparent anode, PEDOT:MoO_3 composite as a HTL, $MAPbB_3$ as the emissive layer, SPW-111 as the electron transfer layer (ETL), and LiF/Ag as the cathode. To obtain the uniform and full coverage of the $MAPbBr_3$ films, which were prepared by a spin-casting procedure of a $MAPbBr_3$ precursor with HBr on PEDOT:MoO_3-coated ITO substrate. The fabrication of PeLEDs are described in details in the Experimental Section. **Figure 2.1** b shows the energy-level diagrams of the PeLEDs. The energy barrier at the interface between the PEDOT:PSS and $MAPbBr_3$ emissive layer prevents hole injection and thus results in lower device efficiency

UPS measurement

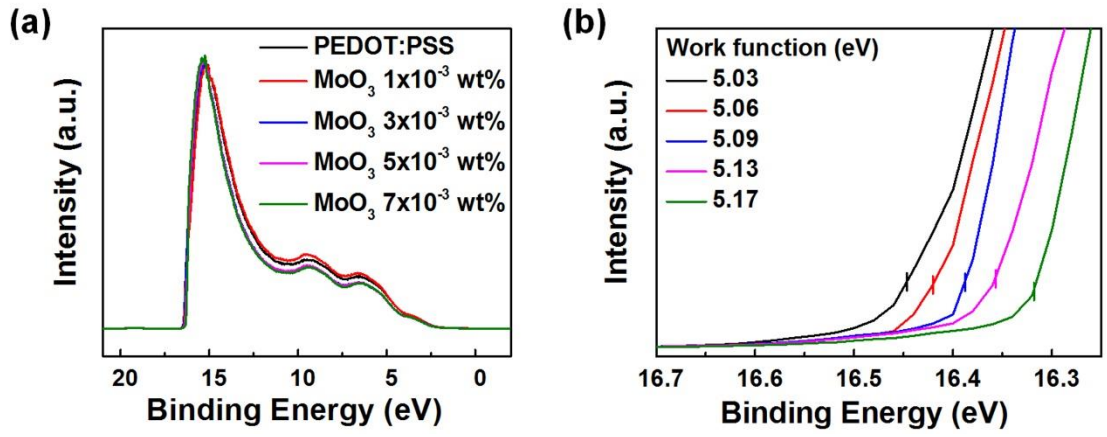

Figure 2.2 (a) UPS Spectra and (b) secondary electron cutoff of PEDOT:MoO3 films using 0-0.007 wt.% of MoO3 powder in the PEDOT:PSS dispersion.

The method of introducing the PEDOT:PSS/MoO_3 composite layer have been suggested as one way to solve the problem of the energy barrier mismatch between emissive layer and anode.[27-29] Thus, we introduced the PEDOT:MoO_3 composite layer between $MAPbBr_3$ and ITO layer by spin coating a mixture solution of ammonium molybdate $(NH_4)_2MoO_4$ powder (MoO_3 powder) and PEDOT:PSS water dispersion (AI 4083) to reduce the hole injection barrier. The work function of PEDOT:MoO_3 composite layers was measured via ultraviolet photoelectron spectroscopy (UPS) measurement using the different concentration of MoO_3 powder in PEDOT:PSS dispersion (0-0.007 wt.%), as shown in Figure 2. The work function of the pure PEDOT:PSS film was measured to be 5.03 eV, in good agreement with previous reports.[30, 31] As shown in Figure 2b, the work function of PEDOT:MoO_3 composite film increases linearly with increasing concentration of MoO_3 powder in PEDOT:PSS dispersion, indicating the increase of the work function from 5.06 to 5.17 eV. It facilitates to minimize the energy barrier between the ITO and the $MAPbBr_3$ emissive layer for efficient hole injection. In addition, the adsorption of the MoO_3 in the PEDOT:PSS of the PEDOT:MoO_3 composite layer was confirmed via X-ray photoelectron spectra measurements by tracking position and shape of the Mo $3d_{5/2}$ peaks at 233.0 eV and Mo $3d_{3/2}$ peaks at 236.1 eV, which is consistent with literature values for MoO_3, as shown in **Figure 2.3**.[29, 32]

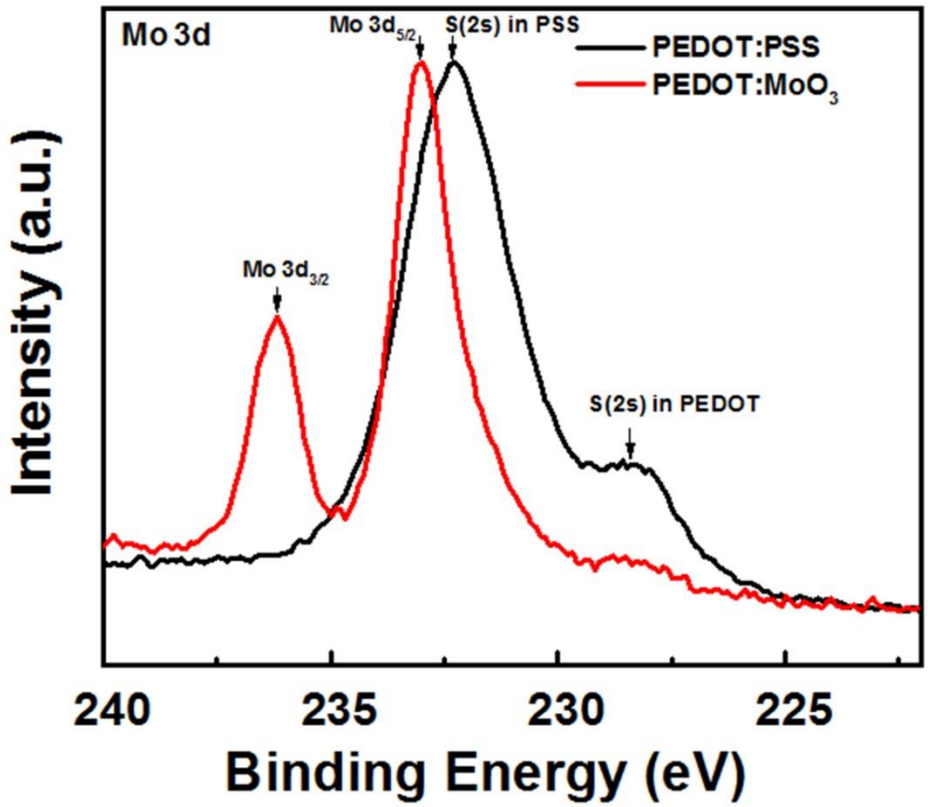

Figure 2.3. XPS spectra of Mo 3d and S 2s core level for PEDOT:PSS (black line) and PEDOT:MoO_3 composite (red line) films.

Scanning electron microscopy and X-ray drffraction

To confirm the surface of the $MAPbB_3$ film, the $MAPbBr_3$ films prepared on PEDOT:PSS, PEDOT:MoO_3 composite and the MoO_3 layer was observed via a scanning electron microscope (SEM), as shown in **Figure 2.4** a-c, respectively. The $MAPbBr_3$ film grown on PEDOT:MoO_3 (0.3 wt%) layer exhibited full surface coverage, similar to the $MAPbBr_3$ film grown on pristine PEDOT:PSS layer, whereas the $MAPbBr_3$ film grown on the pristine MoO_3 layer exhibited lower surface coverage with many pinholes. The surface of the PEDOT:PSS, PEDOT:MoO_3 composite (0.3 wt%), and the MoO_3 layer was also confirmed by atomic force microscopy (AFM), as shown in **Figure 2.4** d-f. The pristine MoO_3 layer showed a very rough surface with a root-mean-square (RMS) value of 2.23, whereas the pristine PEDOT:PSS layer and PEDOT:MoO_3 layers showed a flatter surface with low RMS roughness values of 0.88 nm and 1.51 nm, respectively. In fact, the poor surface coverage of perovskite films deposited on to pure MoO_3 film is a similar result to that in a previous report.[36] To confirm the crystallinity of $CH_3NH_3PbBr_3$ films prepared under different conditions of PEDOT:MoO_3 (0–0.7 wt%) composite layers, the X-ray diffraction (XRD) patterns of the resulting films were collected, as shown

in **Figure 2.5**. The intensity of the peak diffracted by the (100) planes in the XRD spectrum of the perovskite film on the PEDOT:MoO_3 composite layer (0.7 wt%) was improved by 220% compared with that of the perovskite film on the pristine PEDOT:PSS layer. The enhanced crystallinity of the perovskite film on the PEDOT:MoO_3 composite layer can be explained by the role of MoO_3 particles as crystal nuclei for perovskite growth during spin casting.[37] However, the $CH_3NH_3PbBr_3$ film prepared on the PEDOT:MoO_3 (0.7 wt%) composite layer exhibited unfavorable surface coverage with many pinholes, as shown in Figure 3. The lower surface coverage of the $CH_3NH_3PbBr_3$ film prepared on the PEDOT:MoO_3 (0.7 wt%) composite layer may originate from the unfavorable morphology of the PEDOT:MoO_3 composite layer with high RMS roughness. In short, as the amount of MoO_3 powder was increased in the PEDOT:PSS dispersion solution, the contact barrier between the HTL and the amount of MoO_3 powder in the PEDOT:PSS dispersion solution decreased while the morphology of the $CH_3NH_3PbBr_3$ film grown on the PEDOT:MoO_3 composite layer became worse. Thus, the optimum wt% of MoO_3 in the PEDOT:MoO_3 composite was required to obtain highly efficient PeLEDs

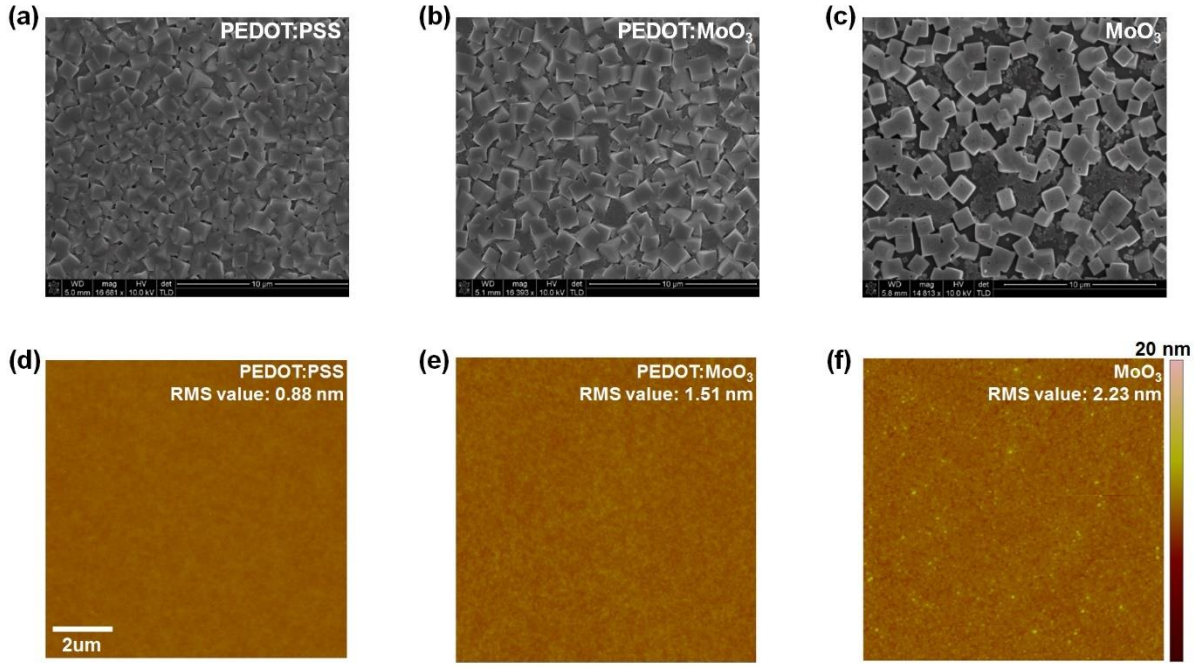

.

Figure 2.4. SEM images of the top surfaces of the $MAPbBr_3$ film on (a) PEDOT:PSS, (b) PEDOT:MoO_3, and (c) MoO_3 layer. AFM images and RMS value of the (d) PEDOT:PSS surface, (e) PEDOT:MoO_3 surface, (f) MoO_3 surface.

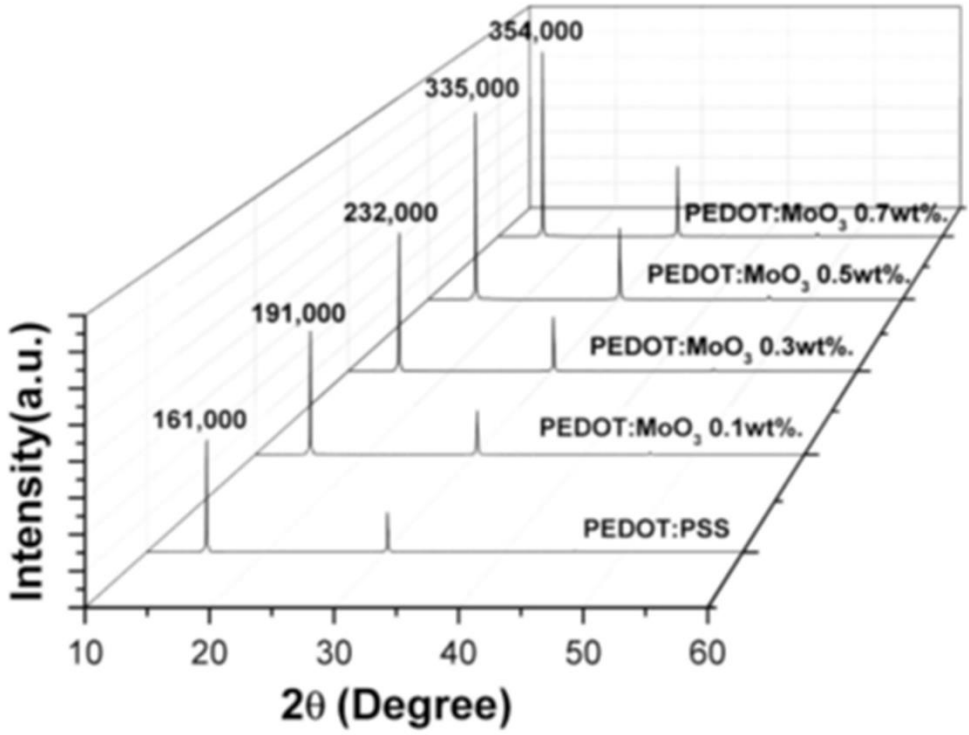

Figure 2.5. XRD patterns of the $CH_3NH_3PbBr_3$ films prepared on different condition of PEDOT:MoO_3 composite layers.

Device performance

To observe the correlation between the improved hole injection and the device performance capabilities, $MAPbBr_3$-based PeLEDs with PEDOT:MoO_3 film deposited using different amount of MoO_3 powder in the PEDOT:PSS dispersion (0-0.007 wt.%) were fabricated and measured. **Figure 2.6** shows (a) the current-density *vs*. voltage (*J-V*), (b) the luminance *vs*. voltage (*L-V*), the luminance efficiency *vs*. luminance (*LE-L*), and (d) external quantum efficiency (*EQE*) *vs*. luminance (*EQE-L*) outcomes for the PeLEDs. The inset figure shows the electroluminescence (EL) spectra of the $MAPbBr_3$ PeLED. The basic device with the pure PEDOT:PSS film showed a maximum luminance level of 5500 cd m^{-2} (at 4.8 V), LE of 0.46 cd A^{-1} (at 4.8 V), and an EQE value of 0.098% (at 4.8 V). In contrast, the optimized PeLEDs with the PEDOT:MoO3 (0.3 wt%) layer exhibited a significantly improved maximum luminance of 9200 cd m^{-2} (at 3.8 V), LE of 0.98 cd A^{-1} (at 3.8 V), and an EQE value of 0.21% (at 3.8 V) due to the reduced energy barrier and the enhanced hole injection. To confirm the reduction of the

contact barrier between the HTL and the $CH_3NH_3PbBr_3$ layer after introducing the PEDOT:MoO_3 composite layer, the current densities of hole only devices using different concentrations of MoO_3 powder in the PEDOT:PSS dispersion were compared, as shown in Fig. S2. In particular, the current density of the hole-only device increased as the amount of the MoO_3 powder in the PEDOT:PSS dispersion increased. This result confirmed that the hole injection in the PeLEDs with the PEDOT:MoO_3 composite layer was enhanced by the reduction of the contact barrier at the $CH_3NH_3PbBr_3$/HTL interface. However, the addition of an excessive amount of the MoO_3 powder material in the PEDOT:PSS dispersion (0.7 wt%) decreased the device efficiency level, possibly due to the non-uniform morphology of the $CH_3NH_3PbBr_3$ films that formed after the addition of the excessive amount of MoO_3 powder into the PEDOT:MoO_3 composite layer. The detailed device performance capabilities of the PeLEDs are summarized in Table 1. To support the device performance results, as shown in Fig. S3 (ESI†), the morphologies of $CH_3NH_3PbBr_3$ films grown on PEDOT:MoO_3 composite layer with different amounts of MoO_3 powder were observed using SEM. As the amount of MoO_3 in the PEDOT:MoO_3 composite layer increased, nonuniform perovskite films with pinholes (red circle) were created by the unfavorable growth of the perovskite crystal on MoO_3. These results represent that the critical factor influencing the surface coverage of $CH_3NH_3PbBr_3$ films is the concentration of MoO_3 in the PEDOT:MoO_3 composite. It should be noted that a PeLED with only a MoO_3 layer shows no luminance with a large leakage current due to the unfavorable morphology of the $CH_3NH_3PbBr_3$ film, as shown in Fig. 4a and b. Therefore, the optimal amount of MoO_3 powder in the PEDOT:PSS dispersion is necessary to obtain highly efficient PeLEDs. The inset in Fig. 4b shows the electroluminescence (EL) spectra of $CH_3NH_3PbBr_3$-based PeLEDs using different amounts of MoO_3 powder in the PEDOT:PSS dispersion for HTLs, where every PeLED shows an EL spectrum identical to that of $CH_3NH_3PbBr_3$ and not SPW-11, indicating that the recombination zone of every PeLED is within the $CH_3NH_3PbBr_3$ emissive layer (see Fig. S4, ESI†). Therefore, the hole carrier injection improved by reducing the contact barrier between the HTL and the perovskite emissive layer led to enhanced performance of PeLEDs due to the increased recombinations of holes and electrons.

2.4 Conclusion

In this work, we demonstrated an improved performance of PeLEDs using a solution-processable PEDOT:MoO_3 composite layer by reducing the energy barrier at the HTL/$CH_3NH_3PbBr_3$ interface and enhancing the crystallinity of $CH_3NH_3PbBr_3$. PeLEDs with an optimal concentration of MoO_3 in the PEDOT: MoO_3 composite layer presented a maximum luminance of 9200 cd m^{-2} and maximum LE of 0.98 cd A^{-1} (at 3.8 V). The significantly improved efficiency of PeLEDs with an optimum PEDOT:MoO_3 layer originates from the enhanced recombination of charge carriers by better hole injection and the increased crystallinity of the perovskite layer. The introduction of the PEDOT:MoO_3

layer is an effective and simple route to achieving high-efficiency perovskite optoelectronic devices such as LEDs, thin-film transistors, laser devices, and photovoltaic applications.

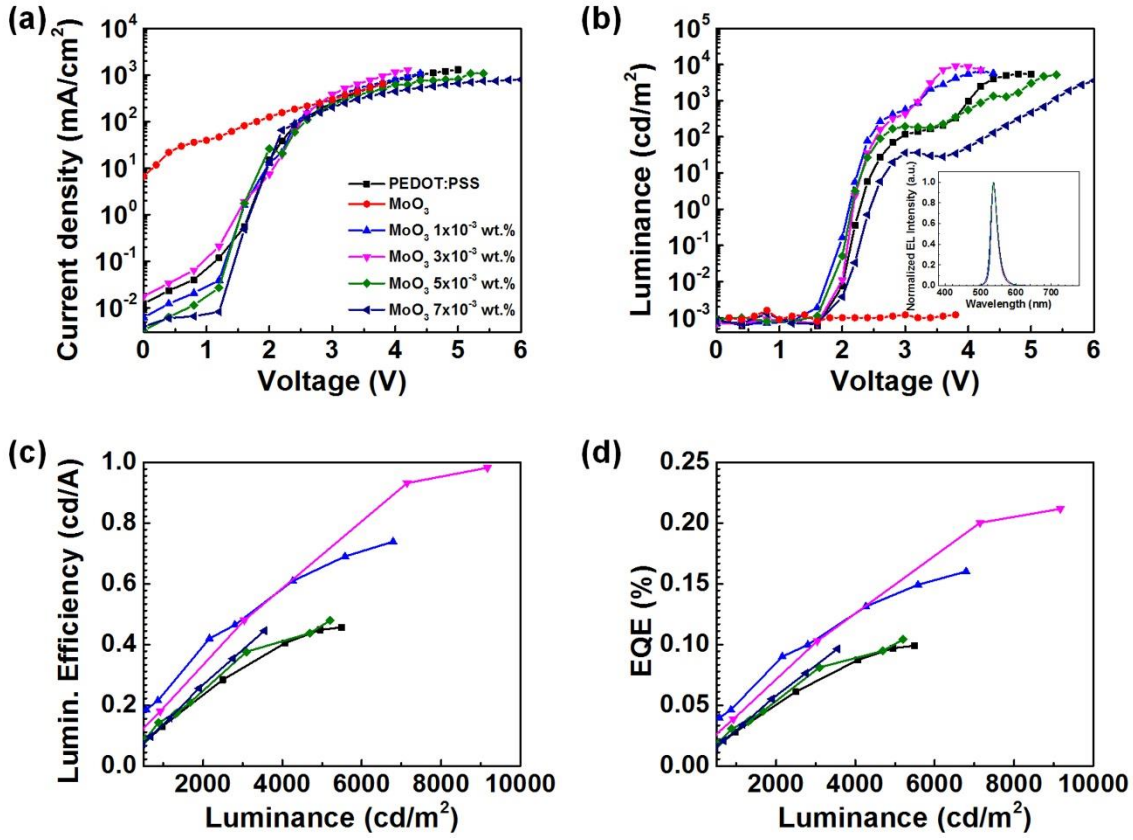

Figure 2.6. PeLEDs light-emitting characterization with different concentration of PEDOT:MoO_3 composite presented in terms of (a) current density vs. voltage (J-V), (b) luminance vs. voltage (L-V), (c) luminance efficiency vs. luminance (LE-L), and external quantum efficiency vs. luminance (EQE-L) curves. The inset shows the electroluminescence spectrum from the PeLEDs.

2.5 References

1 C. Wehrenfennig, G. E. Eperon, M. B. Johnston, H. J. Snaith and L. M. Herz, Adv. Mater., 2014, 26, 1584–1589.

2 S. D. Stranks, G. E. Eperon, G. Grancini, C. Menelaou, M. J. P. Alcocer, T. Leijtens, L. M. Herz, A. Petrozza and H. J. Snaith, Science, 2013, 342, 341–344.

3 C. S. Ponseca, T. J. Savenije,M. Abdellah, K. Zheng, A. Yartsev, T. Pascher, T. Harlang, P. Chabera, T. Pullerits, A. Stepanov, J.-P. Wolf and V. Sundstro¨m, J. Am. Chem. Soc., 2014, 136, 5189–5192.

4 G. Xing, N. Mathews, S. Sun, S. S. Lim, Y.M. Lam, M. Gra¨tzel, S. Mhaisalkar and T. C. Sum, Science, 2013, 342, 344–347.

5 J. H. Noh, S. H. Im, J. H. Heo, T. N. Mandal and S. I. Seok, Nano Lett., 2013, 13, 1764–1769.

6 F. Deschler,M. Price, S. Pathak, L. E. Klintberg, D.-D. Jarausch, R. Higler, S. Hu¨ttner, T. Leijtens, S. D. Stranks, H. J. Snaith, M. Atatu¨re, R. T. Phillips and R. H. Friend, J. Phys. Chem. Lett., 2014, 5, 1421–1426.

7 Z.-K. Tan, R. S. Moghaddam, M. L. Lai, P. Docampo, R. Higler, F. Deschler, M. Price, A. Sadhanala, L. M. Pazos, D. Credgington, F. Hanusch, T. Bein, H. J. Snaith and R. H. Friend, Nat. Nanotechnol., 2014, 9, 687–692.

8 H. Zhu, Y. Fu, F. Meng, X. Wu, Z. Gong, Q. Ding, M. V. Gustafsson, M. T. Trinh, S. Jin and X. Y. Zhu, Nat. Mater., 2015, 14, 636–642.

9 L. Protesescu, S. Yakunin, M. I. Bodnarchuk, F. Krieg, R. Caputo, C. H. Hendon, R. X. Yang, A. Walsh and M. V. Kovalenko, Nano Lett., 2015, 15, 3692–3696.

10 X. Li, Y. Wu, S. Zhang, B. Cai, Y. Gu, J. Song and H. Zeng, Adv. Funct. Mater., 2016, 26, 2435–2445.

11 G. Nedelcu, L. Protesescu, S. Yakunin, M. I. Bodnarchuk, M. J. Grotevent and M. V. Kovalenko, Nano Lett., 2015, 15, 5635–5640.

12 J. Song, J. Li, X. Li, L. Xu, Y. Dong and H. Zeng, Adv. Mater., 2015, 27, 7162–7167.

13 A. Sadhanala, S. Ahmad, B. Zhao, N. Giesbrecht, P. M. Pearce, F. Deschler, R. L. Z. Hoye, K. C. Go¨del, T. Bein, P. Docampo, S. E. Dutton, M. F. L. De Volder and R. H. Friend, Nano Lett., 2015, 15, 6095–6101.

14 A. B. Wong, M. Lai, S. W. Eaton, Y. Yu, E. Lin, L. Dou, A. Fu and P. Yang, Nano Lett., 2015, 15, 5519–5524.

15 G. Xing, N. Mathews, S. S. Lim, N. Yantara, X. Liu, D. Sabba, M. Gra¨tzel, S. Mhaisalkar and T. C. Sum, Nat. Mater., 2014, 13, 476–480.

16 Y. Lee, J. Kwon, E. Hwang, C.-H. Ra, W. J. Yoo, J.-H. Ahn, J. H. Park and J. H. Cho, Adv. Mater., 2015, 27, 41–46. 17 X. Hu, X. Zhang, L. Liang, J. Bao, S. Li, W. Yang and Y. Xie,

Adv. Funct. Mater., 2014, 24, 7373–7380.

18 H. Cho, S.-H. Jeong, M.-H. Park, Y.-H. Kim, C. Wolf, C.-L. Lee, J. H. Heo, A. Sadhanala, N. Myoung, S. Yoo, S. H. Im, R. H. Friend and T.-W. Lee, Science, 2015, 350, 1222–1225.

19 G. Li, F. W. R. Rivarola, N. J. L. K. Davis, S. Bai, T. C. Jellicoe, F. D. L. Pen˜a, S. Hou, C. Ducati, F. Gao, R. H. Friend, N. C. Greenham and Z.-K. Tan, Adv. Mater., 2016, 28, 3528–3534.

20 J. Xing, F. Yan, Y. Zhao, S. Chen, H. Yu, Q. Zhang, R. Zeng, H. V. Demir, X. Sun, A. Huan and Q. Xiong, ACS Nano, 2016, 10, 6623–6630.

21 J. C. Yu, D. B. Kim, G. Baek, B. R. Lee, E. D. Jung, S. Lee, J. H. Chu, D.-K. Lee, K. J. Choi, S. Cho and M. H. Song, Adv. Mater., 2015, 27, 3492–3500.

22 J. C. Yu, D. B. Kim, E. D. Jung, B. R. Lee and M. H. Song, Nanoscale, 2016, 8, 7036–7042.

23 J. C. Yu, D. W. Kim, D. B. Kim, E. D. Jung, J. H. Park, A.-Y. Lee, B. R. Lee, D. D. Nuzzo, R. H. Friend and M. H. Song, Adv. Mater., 2016, DOI: 10.1002/adma.201601105.

24 R. L. Z. Hoye, M. R. Chua, K. P. Musselman, G. Li, M.-L. Lai, Z.-K. Tan, N. C. Greenham, J. L. MacManus-Driscoll, R. H. Friend and D. Credgington, Adv. Mater., 2015, 27, 1414–1419.

25 G. Li, Z.-K. Tan, D. Di, M. L. Lai, L. Jiang, J. H.-W. Lim, R. H. Friend and N. C. Greenham, Nano Lett., 2015, 15, 2640–2644.

26 J. Li, S. G. R. Bade, X. Shan and Z. Yu, Adv. Mater., 2015, 27, 5196–5202.

27 Y. Ling, Z. Yuan, Y. Tian, X. Wang, J. C. Wang, Y. Xin, K. Hanson, B.Ma and H. Gao, Adv. Mater., 2016, 28, 305–311.

28 Y.-H. Kim, H. Cho, J. H. Heo, T.-S. Kim, N. Myoung, C.-L. Lee, S. H. Im and T.-W. Lee, Adv. Mater., 2015, 27, 1248–1254.

29 X. Zhang, H. Lin, H. Huang, C. Reckmeier, Y. Zhang, W. C. H. Choy and A. L. Rohach, Nano Lett., 2016, 16, 1415–1420.

30 H. Sung, N. Ahn, M. S. Jang, J.-K. Lee, H. Yoon, N.-G. Park and M. Choi, Adv. Energy Mater., 2016, 6, 1501873.

31 Y. Zhao, J. Chen, W. Chen and D. Ma, J. Appl. Phys., 2012, 111, 043716.

32 S. Shao, J. Liu, J. Bergqvist, S. Shi, C. Veit, U. Wu¨rfel, Z. Xie and F. Zhang, Adv. Energy Mater., 2013, 3, 349–355.

33 A. J. Ma¨kinen, I. G. Hill, R. Shashidhar, N. Nikolov and Z. H. Kafafi, Appl. Phys. Lett., 2001, 79, 557–559.

34 N. Koch, A. Kahn, J. Ghijsen, J.-J. Pireaux, J. Schwartz, R. L. Johnson and A. Elschner, Appl. Phys. Lett., 2003, 82, 70–72.

35 T. Hiate, N. Miyauchi, Q. Liu, R. Ishikawa, K. Ueno and H. Shirai, J. Appl. Phys., 2014, 115, 123514.

36 F. Hou, Z. Su, F. Jin, X. Yan, L. Wang, H. Zhao, J. Zhu, B. Chu and W. Li, Nanoscale, 2015, 7, 9427–9432.

37 C. Liu, Z. Su, W. Li, F. Jin, B. Chu, J. Wang, H. Zhao, C. S. Lee, J. Tang and B. Kang, Org. Electron., 2016, 33, 221–226.

Devices configuration	L_{max} [cd/m^2] @ bias	LE_{max} [cd/A] @ bias	EQE_{max} [%] @ bias	Turn-on voltage [V] @ 0.1 cd m^{-2}
ITO/PEDOT:PSS/$MAPbBr_3$/SPW-111/LiF/Ag	5488 @ 4.8	0.46 @ 4.8	0.098 @ 4.8	2.2
ITO/PEDOT:MoO_3 (0.001wt.%) /$MAPbBr_3$/SPW-111/LiF/Ag	6791 @ 4.2	0.74 @ 4.2	0.16 @ 4.2	2.0
ITO/PEDOT:MoO_3 (0.003 wt.%)/$MAPbBr_3$/SPW-111/LiF/Ag	9167 @ 3.8	0.981 @ 3.8	0.21 @ 3.8	2.0
ITO/PEDOT:MoO_3 (0.005 wt.%)/$MAPbBr_3$/SPW-111/LiF/Ag	5199 @ 5.4	0.48 @ 5.4	0.10 @ 5.4	2.0
ITO/PEDOT:MoO_3 (0.007 wt.%)/$MAPbBr_3$/SPW-111/LiF/Ag	3545 @ 6.0	0.445 @ 6.0	0.096 @ 6.0	2.4

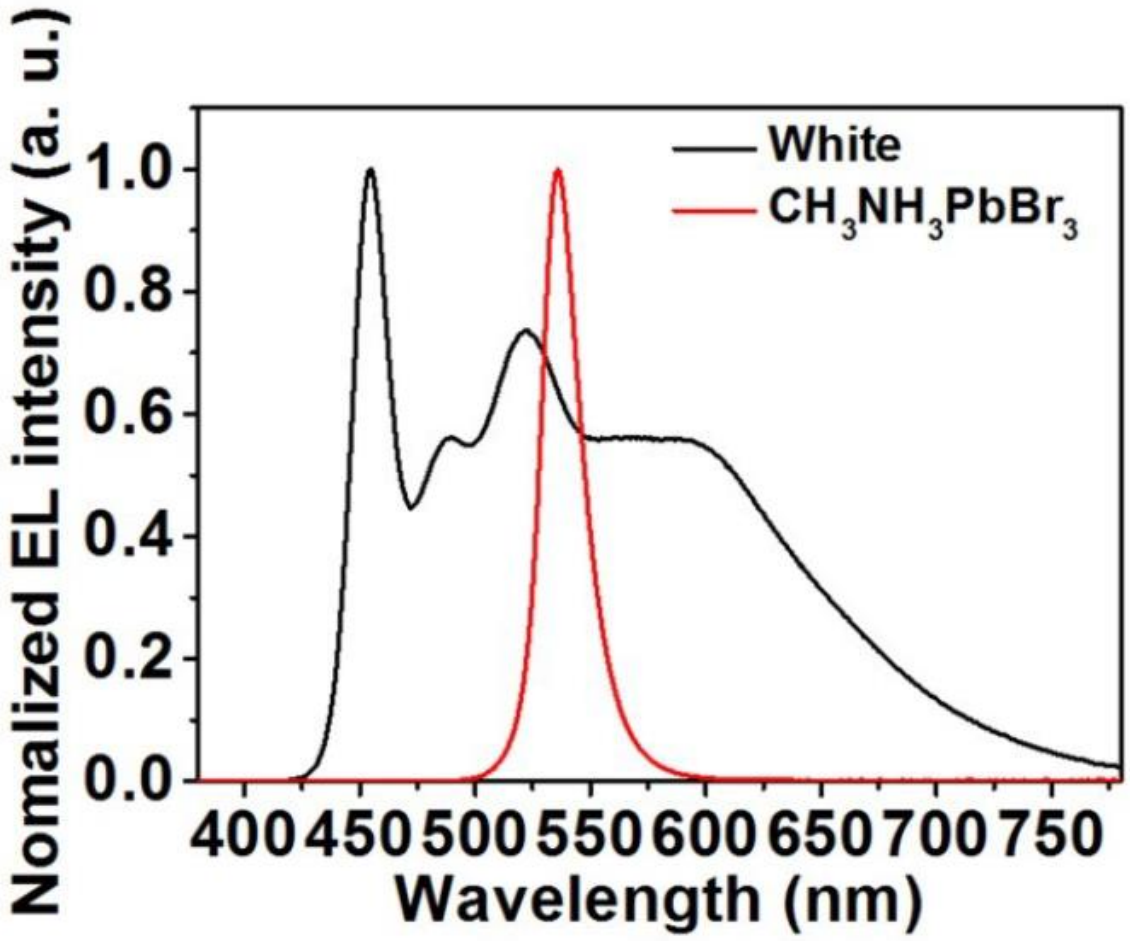

Figure 2.7. Normalized EL spectra of polymer LED (emissive layer: SPW-111 (white)) (black) and PeLED (emissive layer: $CH_3NH_3PbBr_3$ (perovskite) (red))

Chapter 3. Control of Interface Defects for Efficient and Stable Quasi-2D Perovskite Light-Emitting Diodes Using Nickel Oxide Hole Injection Layer

3.1 Research back ground

Metal halide perovskites (MHPs) have emerged as a promising class of materials for optically pumped lasers and light-emitting diodes (LEDs) owing to their narrow emission spectrum and wide range of color tunability.[1-7] To date, perovskite LEDs (PeLEDs) have recorded an external quantum efficiency (EQE) of up to 14.36% for green emissions[6] and 12.7% for near-infrared emissions.[7] However, the low exciton binding energy in MHPs is a fundamental limitation that leads to the generation of free charges at room temperature. The competition between the trap-mediated non-radiative recombination and the electron-hole radiative bimolecular recombination causes a low photoluminescence quantum yield (PLQY) and a PLQY dependence on the excitation intensity.[8,9] Therefore, low trap density in MHPs is required to increase radiative bimolecular recombination rate for high PLQY and EQE values of PeLEDs.

The choice of monovalent organic cation can strongly influence the optical and electrical properties of MHPs.[10-14] Many researchers have reported that formamidinium lead halide shows remarkably enhanced carrier diffusion length compared with methylammonium lead halide.[10-12] Hanusch et al. showed that the carrier lifetime in polycrystalline films of formamidinium lead bromide ($FAPbBr_3$) is much longer than that of methylammonium lead bromide ($MAPbBr_3$).[10] Moreover, Zhumekenov et al. reported that $FAPbBr_3$ single crystals show superior optical and electrical properties, with a much longer carrier diffusion length and a lower dark current, to $MAPbBr_3$,[11] which they attributed to the considerably lower trap density of $FAPbBr_3$. Thus, $FAPbBr_3$ is a potential candidate for light-emitting material for high-performance PeLEDs.

In LED applications, the charge balance injected from charge transport layers (CTLs) is crucial for maximizing the recombination rate in the emitting layer for high LED performance. Ideal CTLs need to meet suitable energy levels for the injection of charges and efficient charge transport by blocking opposite charges.[15,16] The bottom CTL also influences the growth of the perovskite crystal and its quality of interface,[17-21] which is very important for the performance of PeLEDs. Defects in the interface of perovskite form deep-level traps inside the band gap,[20,21] which can be the dominant non-radiative recombination channel. For the organic hole transport layer (HTL), poly(3,4-ethylenedioxythiophene):poly-styrene sulfonate (PEDOT:PSS) is commonly used as a HTL. However, there is evidence that its acidic and hydroscopic nature severely deteriorates long-term stability.[22-24] Moreover, PEDOT:PSS causes the quenching of luminescence at its interface with the perovskite layer, which degrades device performance. As an alternative to PEDOT:PSS, such stable inorganic p-type materials as copper thiocyanate (CuSCN), vanadium oxide (V_2O_5), molybdenum oxide (MoO_3), and

nickel oxide (NiO_x) have been introduced as promising HTLs.[25-33] These metal oxides have the advantages of good air stability, high transparency, and high carrier mobility. Furthermore, crystalline metal oxides can facilitate the growth of highly crystalline perovskite and improve the quality of interface between metal oxides and perovskite,[34,35] leading to a reduced path for non-radiative recombination.

In this study, we control the trap density of perovskite through compositional, dimensional, and interfacial modulations, which substantially increase bimolecular radiative recombination by outcompeting trap-mediated non-radiative recombination. Owing to the low trap density, long-living free carriers of formamidinium (FA) based perovskite are allowed to recombine in small radiative domains through efficient and fast energy transfer by modulating the dimensionality. Moreover, we investigate interfacial defects of perovskite deposited on NiO_x and PEDOT:PSS through ambient pressure air photoemission spectroscopy (APS), the Kelvin probe (KP), and surface photovoltage (SPV) for perovskite films of varying thicknesses. Crystalline NiO_x enables the growth of highly crystalline perovskite with fewer interface defects, which enhances the optical properties and photostability of perovskite as well as the operational stability of PeLEDs. Through effective control over the trap density of perovskite, we demonstrate efficient and stable green emissive PeLEDs with a maximum luminance of 24,100 cd m^{-2}, maximum current efficiency (CE) of 62.4 cd A^{-1}, and maximum EQE of 14.6%.

3.2 Experimental

Materials: PEDOT:PSS (AI 4083, Clevios) and nickel acetate tetrahydrate (99.998%, Sigma Aldrich) were used without being subjected to any purification. $PbBr_2$ (99.999%, Alfa Aesar), FABr (Dyesol), BABr (98%, Tokyo Chemical Industry), and TPBi (99.9%, OSM) were used without further purification.

Device fabrication: A patterned ITO/glass substrate was cleaned using an ultrasonic bath in deionized water, acetone, and isopropanol for 10 minutes. PEDOT:PSS dispersion was spin-coated at 5000 rpm for 40 s onto the ultraviolet-ozone treated ITO substrate, and was then annealed at 140 °C for 10 min at in a nitrogen-filled glove box. To prepare NiO_x precursor, nickel acetate tetrahydrate with ethanolamine (mole ratio of 1:1) was dissolved in 2-Methoxyethanol string 80 °C for 4 h (1.2M). The precursor was spin-coated at 4,000 rpm for 45 s and annealed at 500 °C for one hour in ambient conditions. To prepare the precursors, $PbBr_2$, FABr, and BABr at a molar ratio of 1:1:0 (3D), 1:0.50:1 (n = 2), 1:0.67:0.67 (n = 3), and 1:0.80:0.40 (n = 5) were dissolved in a dimethylformamide /dimethyl sulfoxide (7:3 v/v) co-solvent (0.3 M) at 60 °C. The perovskite precursor was first spin-coated onto the substrate at 3000 rpm for 80 s on the HTL using a hydrophilic filter (pore size 0.45 μm). After a delay of 30 s, 80 μL of the chlorobenzene anti-solvent solution was dropped and spin-cast onto the precursor film in the nitrogen-filled glove box. TPBi as electron transport layers (60 nm) were deposited using a thermal evaporation

system at an evaporation rate of 0.5 Å s^{-1}. Finally, for electrode formation, LiF (1 nm) and Al (100 nm) were successively deposited using a thermal evaporation system at the high vacuum of ~1 x 10^{-6} torr.

Device characterization: The *J-V-L* and device efficiencies of the PeLEDs with encapsulation were obtained using a computer-controlled Keithley 2400 Source Meter and a Konica Minolta spectroradiometer (CS-2000, Minolta) under ambient conditions.

Time-resolved and steady-state PL measurements: Time-resolved and steady-state PL spectra were measured using a time-correlated single-photon counting (TCSPC) setup (FluoTime 300), described elsewhere.[3] The excitation source was a 450-nm continuous wave and pulsed diode laser head (LDH-D-C-450) coupled with a laser diode driver (PDL 820) with a pulse width of < 70 ps and a repetition rate of 196 kHz–40 MHz. The time-resolved PL signal was obtained using a TCSPC module (PicoHarp) with a photomultiplier tube (PMA-C 182-N-M). Each exponential decay curve was deconvoluted using the associated fitting software (FluoFit) to calculate the time constant associated with each curve.

SEM measurements: SEM measurements were performed using a Nanonova 230 FEI SEM with an accelerating voltage of 10 kV. A 5-nm platinum layer was deposited on each perovskite film to prevent any charging effects using a sputter coater (Emitech K575x, Tescan).

XRD measurements: XRD measurements were performed using a D/MAX2500V/PC (Rigaku, Japan) equipped with a Cu Kα radiation source (λ = 1.5405 Å). The step size was 0.02°, with an acquisition time of 60 s deg^{-1}.

PLQY measurement: The PLQY of the perovskite films were obtained using an integrating sphere method. The samples were excited using a 407-nm continuous wave diode laser with a focused beam spot of ~0.3 mm^2 and an excitation intensity of 48 mW. An Andor iDus DU490A InGaAs detector was used to measure emission. The details have been described elsewhere.[1]

Confocal fluorescence imaging: Confocal PL images of the perovskite films were measured using an LSM 780 NLO laser scanning confocal microscope (Carl Zeiss) with a 100x oil immersion objective (a Plan-APO, NA = 1.46). The excitation source was a 405-nm diode laser.

EL microscopy: EL microscopy images of the PeLED samples fabricated with quasi-2D perovskite film with n = 3 deposited on NiO_x and PEDOT:PSS were obtained using an inverted microscope (IX81, Olympus).

Measurements of APS, KP, and SPV: Measurements of APS, KP, and SPV were made using the KP technology APS-04 instrument. For APS measurements, the sample was illuminated with UV light from a monochromatic deuterium lamp source (4–7 eV). The raw photoemission data were corrected for offset and the cube root was taken, with the HOMO value found from the extrapolated intersection of the straight-line fit of the cube root of the photoemission with the baseline.

KP WF measurements were taken by using a 2-mm gold alloy-coated vibrating tip above the surface of the sample, with the resulting contact potential difference between the tip and the sample added to the

WF of the gold tip to find the resultant WF of the sample. For SPV measurements, the sample was illuminated with a 150-W quartz halogen lamp coupled by fiber optic and focused on the sample.

3.3 Results and discussion

To investigate the optical properties and thermal stability of perovskites using FA and methylammonium (MA), we obtained $FAPbBr_3$ and $MAPbBr_3$ films with similar morphologies and grain sizes using the same fabrication method and condition (**Figure 3.1**). Despite their similar morphologies, the $FAPbBr_3$ and $MAPbBr_3$ films showed significantly different properties. Although the reason for the remarkable difference in the properties of perovskites using FA and MA is unclear, previous reports have proposed that the outstanding properties of FA-based perovskite can be attributed to its low trap density.[10,11]

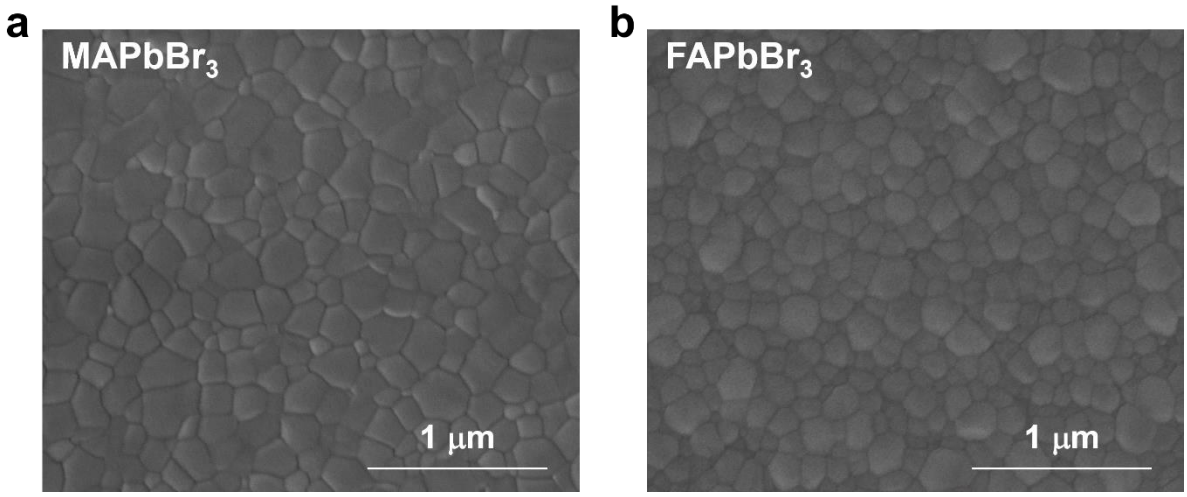

Figure 3.1 SEM images of $FAPbBr_3$ and $MAPbBr_3$. SEM images of a) 3D $MAPbBr_3$ and b) 3D $FAPbBr_3$.

$FAPbBr_3$ and $MAPbBr_3$ have similar morphologies and grain sizes obtained through the same fabrication method and conditions. The SEM images of $FAPbBr_3$ and $MAPbBr_3$ showed full coverage and smooth morphologies without any pinhole.

Time-resolved and steady-state photoluminescence (PL) spectra were measured to investigate the optical properties of $FAPbBr_3$ and $MAPbBr_3$ (**Figure 3.2** a,b). The PL lifetime of $FAPbBr_3$ was significantly greater than that of $MAPbBr_3$, indicating that free carriers in $FAPbBr_3$ were able to survive for a long time without being trapped. The long diffusion of the free carriers increased the probability of bimolecular recombination to regain their bound forms for radiative decay. Consequently, $FAPbBr_3$ showed a higher PL intensity than $MAPbBr_3$ (**Figure 3.2** b).

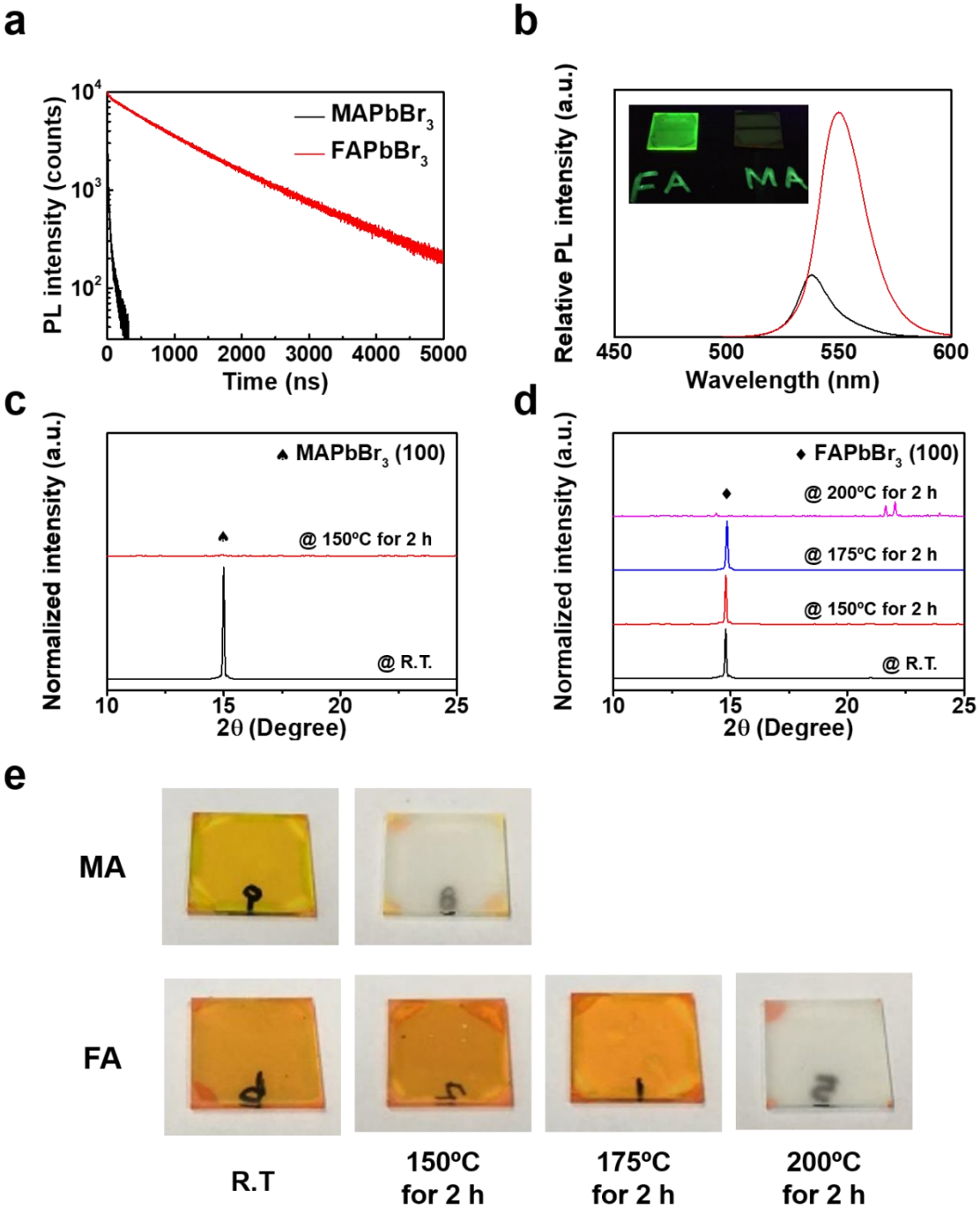

Figure 3.2. Schematic of device structure, chemical structure, cross-sectional SEM image, XRD, absorption and PL. a) Schematic of the structures of PeLED and quasi-2D perovskite (n = 3), and the chemical structure of BA. b) Cross-sectional SEM image of the PeLED device. c) Normalized XRD patterns, d) absorbance, and e) normalized PL spectra of 3D $FAPbBr_3$ and quasi-2D perovskites with n = 2, 3, and 5.

$FAPbBr_3$ exhibited red-shifted band edge absorption and PL emission owing to a smaller band gap than $MAPbBr_3$ (**Figure 3.3**), which can be attributed to a larger lattice constant of $FAPbBr_3$ on account of the large size of FA.

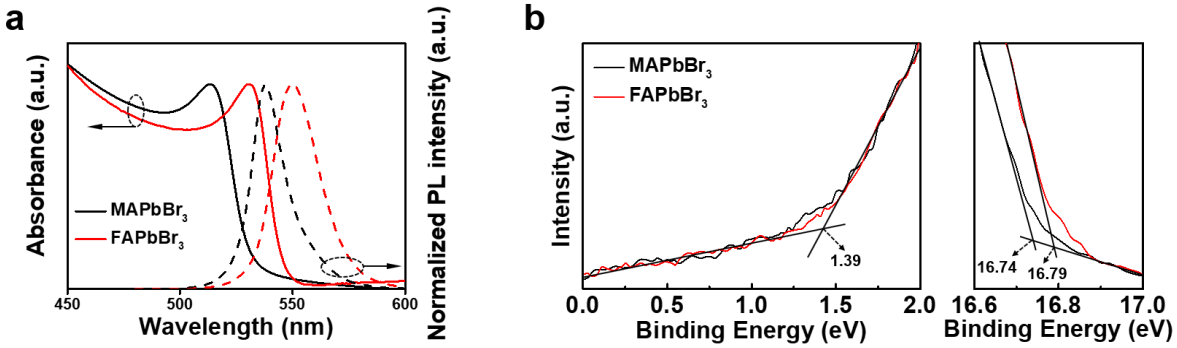

Figure 3.3. Absorbance and UPS of $MAPbBr_3$ and $FAPbBr_3$. a) Absorbance and normalized PL spectra of $MAPbBr_3$ and $FAPbBr_3$. b) UPS data of $MAPbBr_3$ and $FAPbBr_3$.

$FAPbBr_3$ showed red-shifted band edge absorption and PL emission owing to a smaller band gap than $MAPbBr_3$. To investigate the energy levels of the conduction band and valence band of $MAPbBr_3$ and $FAPbBr_3$, we measured absorbance and UPS. We measured the optical band gaps of $MAPbBr_3$ and $FAPbBr_3$ at 2.34 and 2.27 eV, respectively, and the valence bands of $MAPbBr_3$ and $FAPbBr_3$ at 5.87 and 5.82 eV, respectively.

To examine the thermal stability of the perovskite depending on the monovalent organic cation, X-ray diffraction (XRD) patterns and photographs of perovskite films were observed before and after thermal annealing (**Figure 3.2** c–e). The decomposition process can be traced through the disappearance of the (100) peak in the XRD patterns of perovskites and the change in film color. The (100) peak in XRD patterns of $MAPbBr_3$ disappeared, and the $MAPbBr_3$ film turned into a colorless and transparent film after annealing at 150 °C for two hours, which indicated that the $MAPbBr_3$ film had completely decomposed. By contrast, the $FAPbBr_3$ film exhibited relatively good thermal stability, showing still the (100) XRD peak and orange color even after annealing at 175 °C for two hours. However, the $FAPbBr_3$ film was completely decomposed after annealing at 200 °C for two hours, showing no (100) XRD peak or colorless film. The thermal stability of $FAPbBr_3$ can be attributed to the fact that the FA cation has a higher probability of forming a hydrogen bond with the inorganic frame than the MA cation.[36,37]

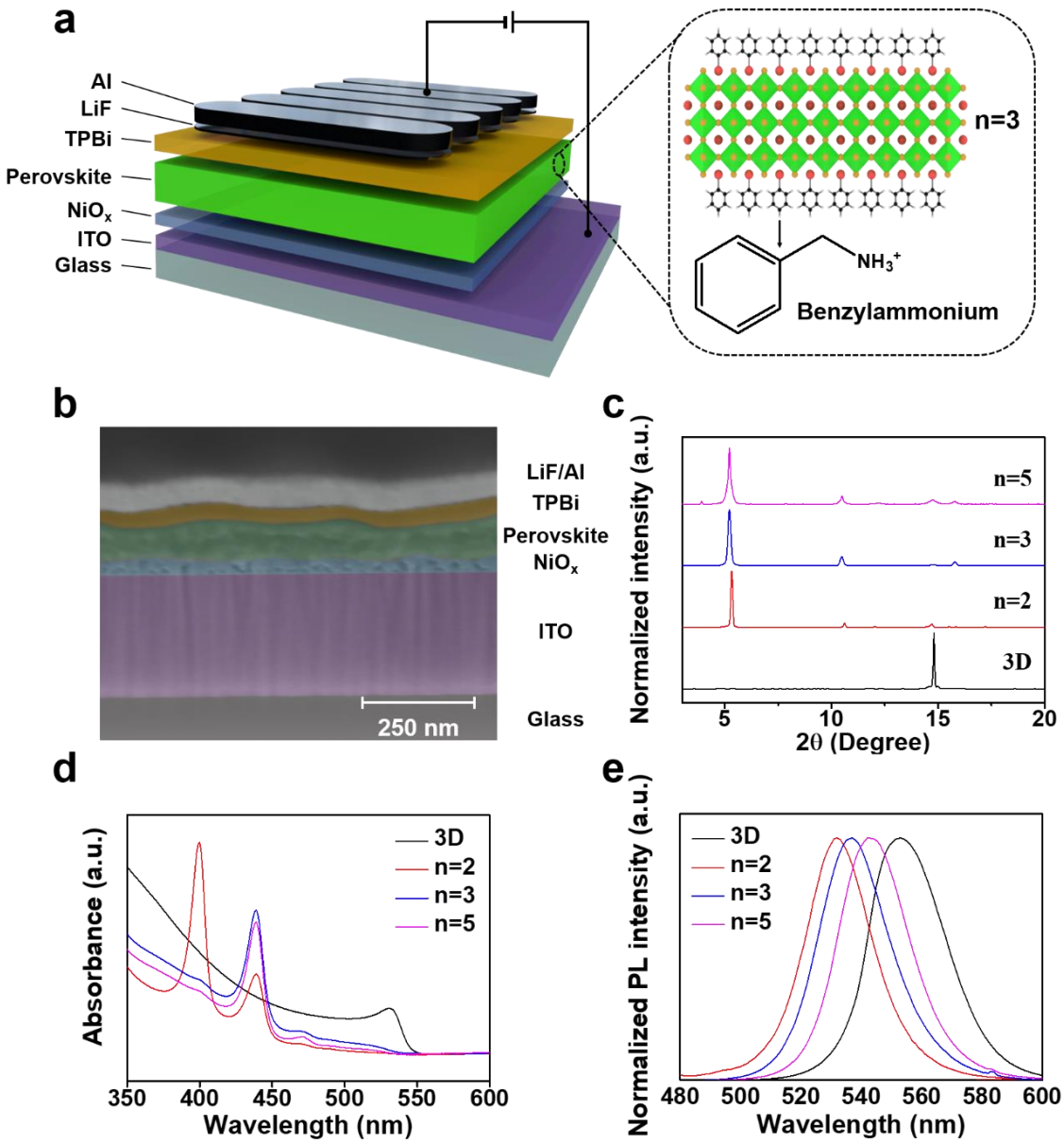

Figure 3.4. Schematic of device structure, chemical structure, cross-sectional SEM image, XRD, absorption and PL. a) Schematic of the structures of PeLED and quasi-2D perovskite (n = 3), and the chemical structure of BA. b) Cross-sectional SEM image of the PeLED device. c) Normalized XRD patterns, d) absorbance, and e) normalized PL spectra of 3D $FAPbBr_3$ and quasi-2D perovskites with n = 2, 3, and 5.

A schematic illustration of the device design and quasi-2D perovskite (average n value = 3) along with the chemical structure of the benzylammonium (BA) incorporated as a bulky ammonium cation to fabricate the quasi-2D perovskite is represented in **Figure 3.4** a. The cross-sectional scanning electron microscopy (SEM) image of PeLEDs with a multi-layered structure of indium tin oxide (ITO)/NiO_x/quasi-2D perovskite (n = 3)/ 2,2′,2″-(1,3,5-benzinetriyl)-tris(1-phenyl-1-H-benzimidazole)

(TPBi)/LiF/Al was observed (**Figure 3.4** b). The dimensional modulation of quasi-2D perovskites can be achieved by adjusting specific stoichiometric quantities of lead bromide ($PbBr_2$), formamidinium bromide (FABr), and benzylammonium bromide (BABr). The structural evolution from 3D to quasi-2D perovskite can be monitored by XRD, and absorption and emission spectra. The XRD patterns of 3D $FAPbBr_3$ showed a peak at 14.80° corresponding to the (100) plane of the cubic phase, whereas the quasi-2D perovskite with n = 2, 3, and 5 showed peaks at small angles ($2\theta < 10°$) owing to their expanded unit cells (**Figure 3.4** c). The absorption spectrum of the 3D $FAPbBr_3$ showed no absorption peaks associated with the large band gap of quasi-2D perovskites, whereas the absorption spectrum of the quasi-2D perovskites clearly showed absorption peaks at high-energy states of the quasi-2D perovskites (**Figure 3.4** d). The quasi-2D perovskite with lower average values of n exhibited stronger absorption peaks at higher energy states as blue-shifted PL spectra owing to their lower dimensionality (**Figure 3.4** d,e). We consider the blue shift of PL to be enabled by recombination at higher energy states of quasi-2D perovskite with smaller n values. Past studies on quasi-2D perovskites have shown that photogenerated excitons are concentrated and confined in the smaller band gap emitters through energy transfer, which increases the local charge density and rate of radiative bimolecular recombination. To confirm the improvement in the optical properties of the quasi-2D perovskites, time-resolved and steady-state PL measurements were performed (**Figure 3.5**).

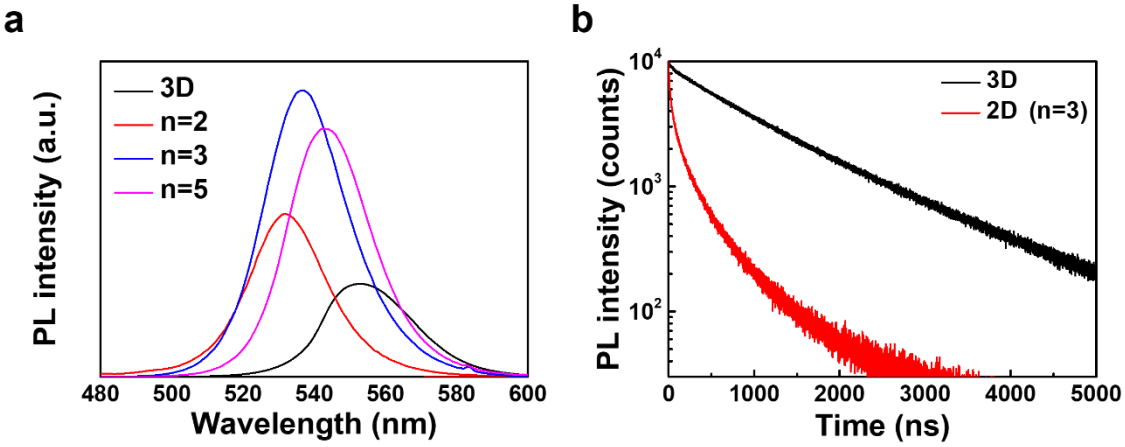

Figure 3.5. Optical properties of 3D $FAPbBr_3$ and quasi-2D perovskite. a) Steady-state PL spectra of 3D $FAPbBr_3$ and quasi-2D perovskite with n = 2, n = 3, and n = 5. b) Time-resolved PL spectra of 3D $FAPbBr_3$ and quasi-2D perovskite with n = 3.

Dimensional modulation concentrates carriers on a smaller band gap emitter through energy transfer, which increases the bimolecular radiative recombination by outcompeting the trap-mediated non-radiative recombination. The PL intensities of the quasi-2D perovskite are higher than that of 3D $FAPbBr_3$, and among th70em, quasi-2D perovskite with n = 3 shows the highest PL intensity through efficient and fast energy transfer. Quasi-2D perovskite with n = 3 shows a substantially shorter PL

lifetime (0.14 μs) than 3D $FAPbBr_3$ (4.66 μs), which indicates that dimensional modulation enables long-living free carriers to recombine in small radiative domains by effectively concentrating them in small radiative domains.

The steady-state PL spectra showed that the PL intensities of the quasi-2D perovskite were higher than those of 3D $FAPbBr_3$. The quasi-2D perovskite with n = 3 showed the highest PL intensity and a high PLQY (53.1%) compared with 3D $FAPbBr_3$ (15.1%). It also yielded a substantially shorter PL lifetime (0.14 μs) than the 3D $FAPbBr_3$ (4.66 μs) (**Table 3.1**), which indicates fast bimolecular recombination by effectively focusing energy on radiative domains.

Table S1. Summarized PL lifetimes of perovskite films deposited on NiO_x and PEDOT:PSS.

Film configuration	τ_{avr} **[μs]**	χ^2
Glass / NiO_x / 3D $MAPbBr_3$	0.01	1.2711
Glass / NiO_x / 3D $FAPbBr_3$	4.66	1.2711
Glass / NiO_x / $BA_2FA_2Pb_2Br_{10}$ (n=3)	0.14	1.2338
Glass / PEDOT:PSS / $BA_2FA_2Pb_2Br_{10}$ (n=3)	0.04	1.3697

To investigate defects in the interface of the perovskite deposited on NiO_x and PEDOT:PSS, APS, KP, and SPV were executed on the perovskite films (at 15 nm, 35 nm, and 120 nm thicknesses) deposited on NiO_x and PEDOT:PSS. The photoemission spectra of the perovskite films deposited on NiO_x and PEDOT:PSS at thicknesses of 15 nm and 120 nm are shown in **Figure 3.6** a,b. The different thicknesses of these films were expected to represent the interface and bulk-like properties. For the 15-nm thick samples, the extrapolated highest occupied molecular orbital (HOMO) values of the perovskite were 5.35 ± 0.05 eV and 5.45 ± 0.05 eV deposited on NiO_x and PEDOT:PSS respectively, whereas those for the 120-nm thick samples increased to 5.50 ± 0.05 eV and 5.55 ± 0.05 eV, respectively. The reduced difference in HOMO values for the 120-nm thick films indicates that while the bulk energy levels of the perovskite remained similar, at the HTL/perovskite interface, the perovskite HOMO was strongly influenced by the HTL underneath. This is most likely caused by the local electronic densities of states of the perovskite altered at/near the HTL. This was further confirmed by the similarities of the APS spectra of the 120-nm thick film to those of the 35-nm thick film, which showed the same extrapolated HOMO values (5.50 ± 0.05 eV and 5.55 ± 0.05 for NiO_x and PEDOT:PSS, respectively) (**Figure 3.7**).

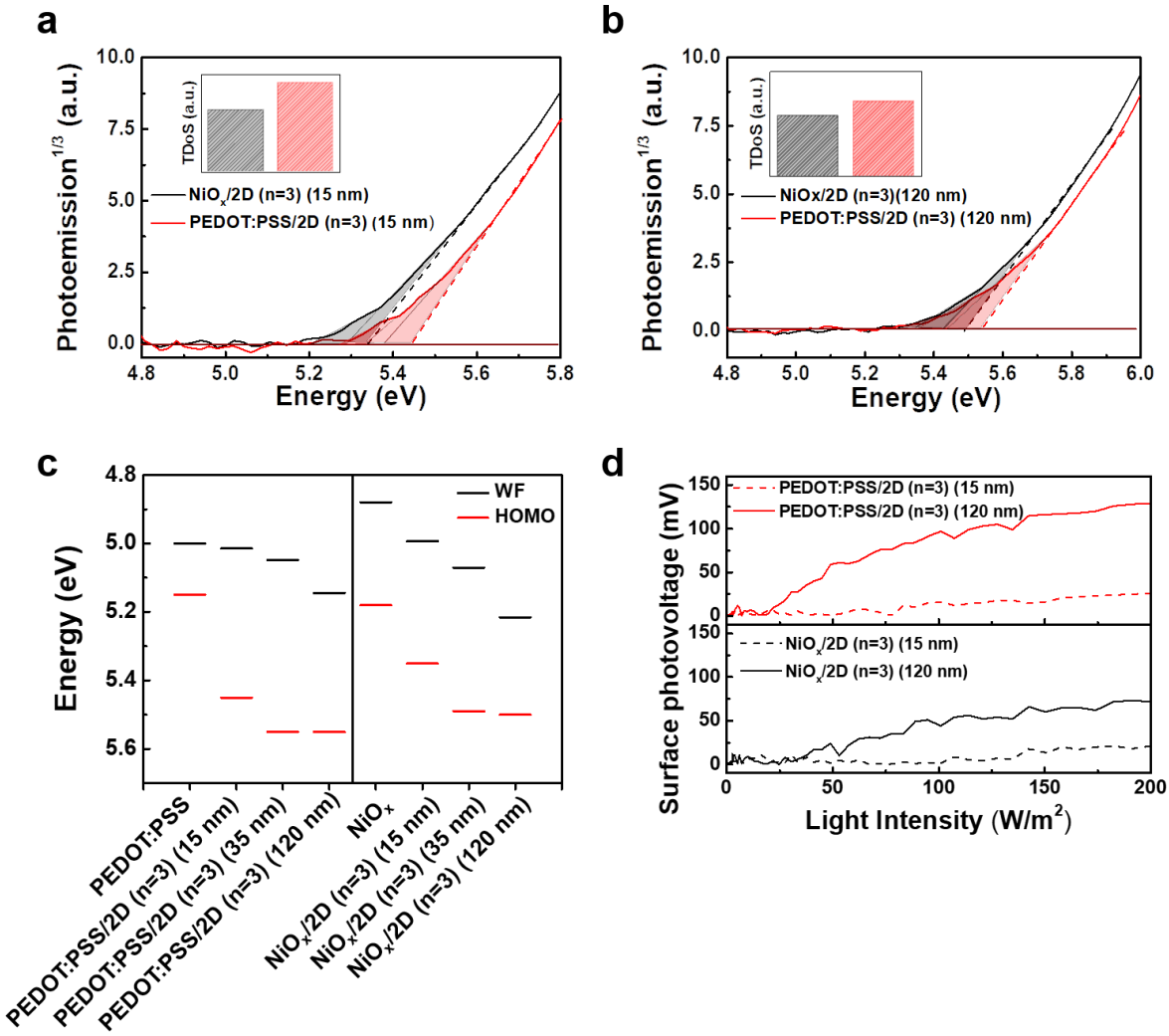

Figure 3.6. APS, WF, HOMO, and SPV measurements for quasi-2D perovskite with n = 3 deposited on NiO_x and PEDOT:PSS. APS spectra for a) 15-nm thick and b) 120-nm thick perovskite films deposited on NiO_x and PEDOT:PSS. c) WFs and HOMO for pristine NiO_x and PEDOT:PSS, as well as perovskite films of 15 nm, 35 nm, and 120 nm deposited on NiO_x and PEDOT:PSS. d) SPV for 15-nm thick (dashed) and 120-nm thick (solid) perovskite films deposited on NiO_x and PEDOT:PSS as a function of light intensity.

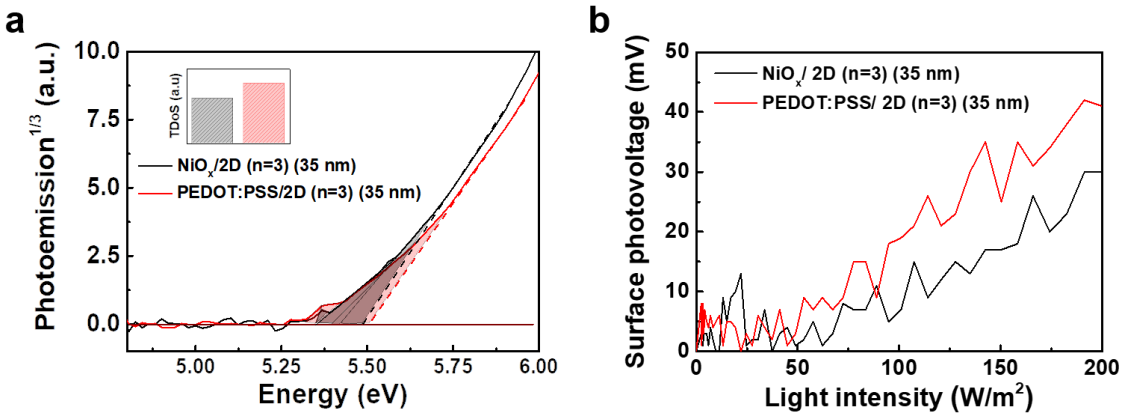

Figure 3.7. APS and SPV measurements for quasi-2D perovskite (35 nm) with n = 3 deposited on NiO_x and PEDOT:PSS. a) APS spectra for 35-nm thick perovskite films deposited on NiO_x and PEDOT:PSS. b) SPV for 35-nm thick perovskite films deposited on NiO_x and PEDOT:PSS.

All the extrapolated HOMO energy levels were shown in **Figure 3.6** c. From the measured HOMO values of the PEDOT:PSS (5.15 eV) and NiO_x (5.18 eV), a relatively larger interfacial energetic barrier for the hole injection is calculated for PEDOT:PSS/perovskite than NiO_x/perovskite samples (0.30 eV vs 0.17 eV), implying that NiO_x would show better hole injection properties when used in perovskite LEDs.

The threshold of energy for photoemission was below the extrapolated HOMO value, which can be attributed to the presence of the sub-band gap trap/defect states within the perovskite.[38,39] Thus, a relative comparison of trap states could be made by comparing the integrated area below the photoemission threshold (shaded area in **Figure 3.6** a,b). We found that 15-nm thick films of perovskite deposited on PEDOT:PSS showed a (~1.45 times) larger area occupied by the sub-gap states (inset in **Figure 3.6** a) than those deposited on NiO_x, indicating that the perovskite deposited on NiO_x had lower trap density than that deposited on PEDOT:PSS. Interestingly, for the 35-nm and 120-nm thick films, the extracted sub-gap area of PEDOT:PSS was only ~1.3 and ~1.2 times greater than that of the NiO_x samples, suggesting that relatively higher density of the trap states was preferentially formed near the interface of PEDOT:PSS and the perovskite.

The work function (WF) values were also measured for 15-nm, 35-nm, and 120-nm thick perovskite films deposited on PEDOT:PSS and NiO_x and shown in **Figure 3.6** c. We observe that the Fermi levels for the 15-, 35- and 120-nm-thick perovskite films deposited on PEDOT:PSS (5.02, 5.05, and 5.15 eV, respectively) were strongly influenced by the WF of the PEDOT:PSS (measured at 5.00 eV), i.e., the Fermi level of the perovskite was “pulled” toward that of PEDOT:PSS.[40,41] This implies that the depletion width of the perovskites on PEDOT:PSS extended through the bulk of the film.[42] On the contrary, perovskite films deposited on NiO_x were slightly less influenced by the WF of the NiO_x film

(measured at 4.88 eV). The Fermi levels of the 15-, 35-, and 120-nm-thick perovskite films deposited on NiO_x were 5.00, 5.07, and 5.21 eV, respectively.

Trap states located on the surface of the semiconductors or the interface of two semiconductors can cause the accumulation of charges, which can develop band bending.[43] Under illumination, surface photovoltage can be generated by the movement of an excessive number of photogenerated charge carriers to fill in these trap states, screening the internal electric field, and reducing band bending. Thus, the magnitude of the SPV can be related to the amount of density of the trap states.[43,44] The SPV values as a function of incident light intensity for 15-nm and 120-nm thick perovskite films deposited on NiO_x and PEDOT:PSS were measured (**Figure 3.6** d). Once the light was turned on, the PEDOT:PSS samples showed an increase in SPV to ~26 mV and 129 mV from the dark values of the 15 nm and 120 nm perovskite films, respectively. The 15 nm and 120 nm perovskite films deposited on NiO_x, however, showed an increase only to ~20 and 72 mV, respectively. The difference in SPV values between the thin and thick films were thus 103 mV for PEDOT:PSS and 52 mV for NiO_x samples. A much larger change in SPV values for PEDOT:PSS samples might indicate a higher density of trap states present at the PEDOT:PSS samples compared with NiO_x samples.

The crystalline NiO_x film enables the growth of highly crystalline perovskite and reduces trap states at the interface of NiO_x and the perovskite layer. The morphologies of the perovskite films deposited on NiO_x and PEDOT:PSS were observed using SEM (**Figure 3.8**). The surface of the perovskite film deposited on NiO_x showed neat morphology without no other shapes of crystallites. In contrast, the surface of the perovskite film deposited on PEDOT:PSS was intricately covered with various shapes of crystallites, which may be attributed to the acidic characteristics of PEDOT:PSS. The morphologies of the perovskite films deposited on PEDOT:PSS with different pH values were compared to investigate the effect of their acidity on the growth of perovskite film. To adjust pH values of PEDOT:PSS, acidic PEDOT:PSS (AI 4083, Celvios) was titrated with imidazole. The pH values of acidic, neutral, and basic PEDOT:PSS were measured to be 1.95, 7.5, and 8.5 using a pH meter. The surface of the perovskite films deposited on pH neutral and basic PEDOT:PSS showed clean morphology without no crystallites, which indicates that the acidic characteristics of PEDOT:PSS have a negative effect on crystal growth.

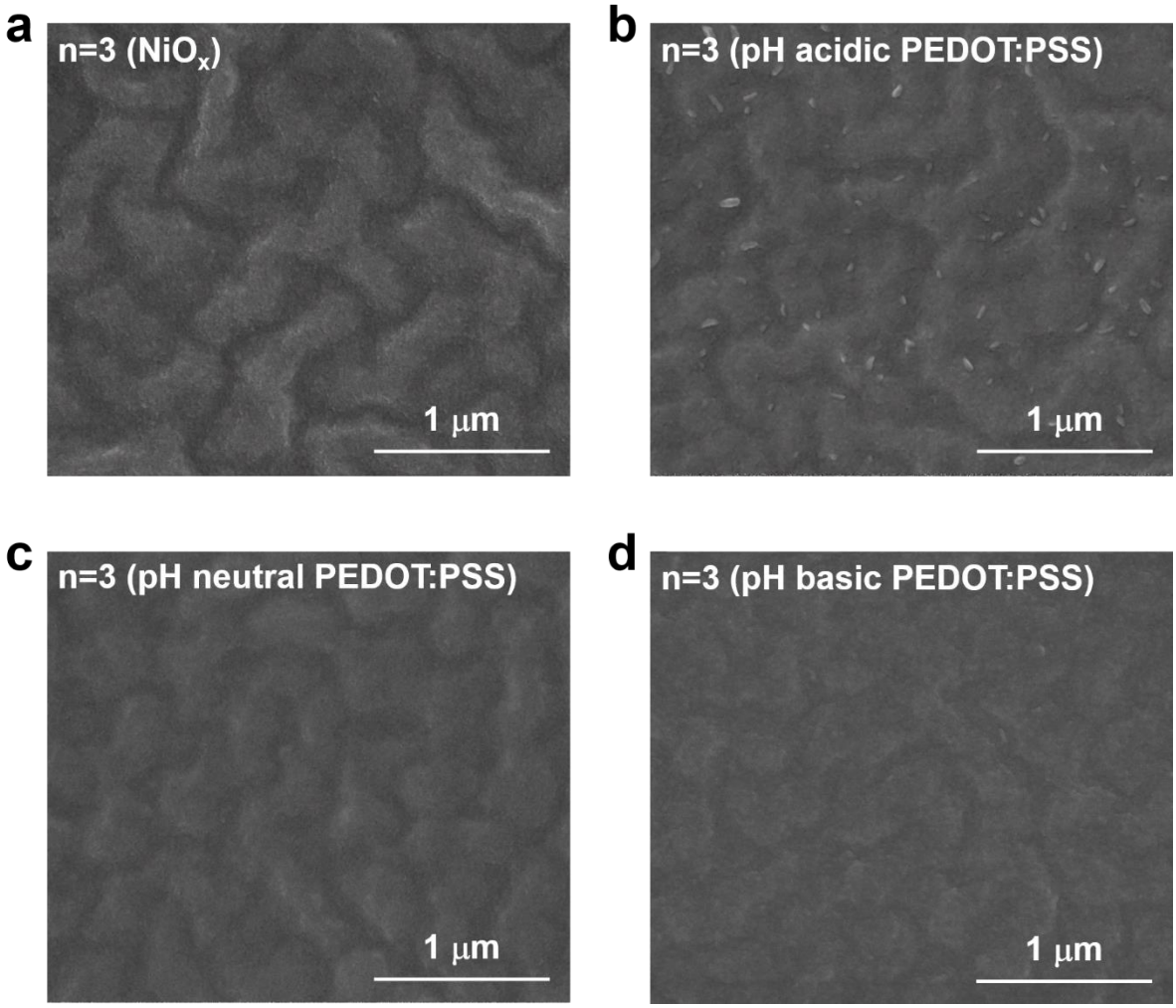

Figure 3.8. SEM images of perovskite films on NiOx and PEDOT:PSS with different pH values. SEM images of quasi-2D perovskite with n = 3 deposited on a) NiO_x, b) pH acidic, c) pH neutral, and d) pH basic PEDOT:PSS.

The crystalline surface can assist the perovskite nucleation process during film formation. The crystalline NiO_x film can enable the growth of highly crystalline perovskite and reduce trap states at the interface of the perovskite and HTL. We measured the morphologies of the perovskite films deposited on NiO_x and PEDOT:PSS. The surface of the perovskite film deposited on NiO_x showed neat morphology without no other shape of crystallite. In contrast, the surface of the perovskite film deposited on PEDOT:PSS was intricately covered with various shapes of crystallites, which may be attributed to the acidic characteristics of PEDOT:PSS. The morphologies of the perovskite films deposited on PEDOT:PSS with different pH values were compared to investigate the effect of its acidity on the growth of perovskite film. PEDOT:PSS (AI 4083, Clevios) was titrated with imidazole to adjust pH values of PEDOT:PSS. The pH values of acidic, neutral and basic PEDOT:PSS were measured to be 1.95, 7.5 and 8.5 using pH meter. The surface of the perovskite films deposited on pH neutral and

basic PEDOT:PSS showed clean morphology without no crystallite, which indicates that the acidic characteristics of PEDOT:PSS have a negative effect on crystal growth.

Moreover, steady-state PL spectra and photographs showing PL emission of perovskite films deposited on NiO_x and PEDOT:PSS with different pH values were observed to investigate the effect of their acidity on optical properties of perovskite (**Figure 3.9**). Perovskite films deposited on pH neutral and basic PEDOT:PSS showed higher PL intensity than that deposited on acidic PEDOT:PSS, but they showed inferior PL intensities to perovskite film deposited on NiO_x. The acidity of PEDOT:PSS have a negative effect on optical properties of the perovskite, and other factors such as hygroscopic and amorphous characteristics may lead to poor interface quality of the perovskite compared with NiO_x.

To further investigate the optical properties of the perovskite films deposited on NiO_x and acidic PEDOT:PSS, their PL lifetimes, PL intensities, and PLQYs were measured (**Figure 3.10** a–c). The perovskite deposited on NiO_x showed a longer PL lifetime, and higher values PLQY compared with the perovskite deposited on PEDOT:PSS. This can be attributed to the fewer trap/defect states. Moreover, the stability of the perovskite deposited on NiO_x and PEDOT:PSS in terms of PL was measured at constant laser excitation using confocal microscopy (**Figures 3.10** and **3.11**). The confocal PL images of the perovskite deposited on NiO_x exhibited bright and full coverage emission, whereas images of the perovskite deposited on PEDOT:PSS showed dark regions dominated by non-radiative recombination. Moreover, highly crystalline perovskite with fewer defects deposited on NiO_x showed better photostability in terms of PL under laser excitation than that deposited on PEDOT:PSS.

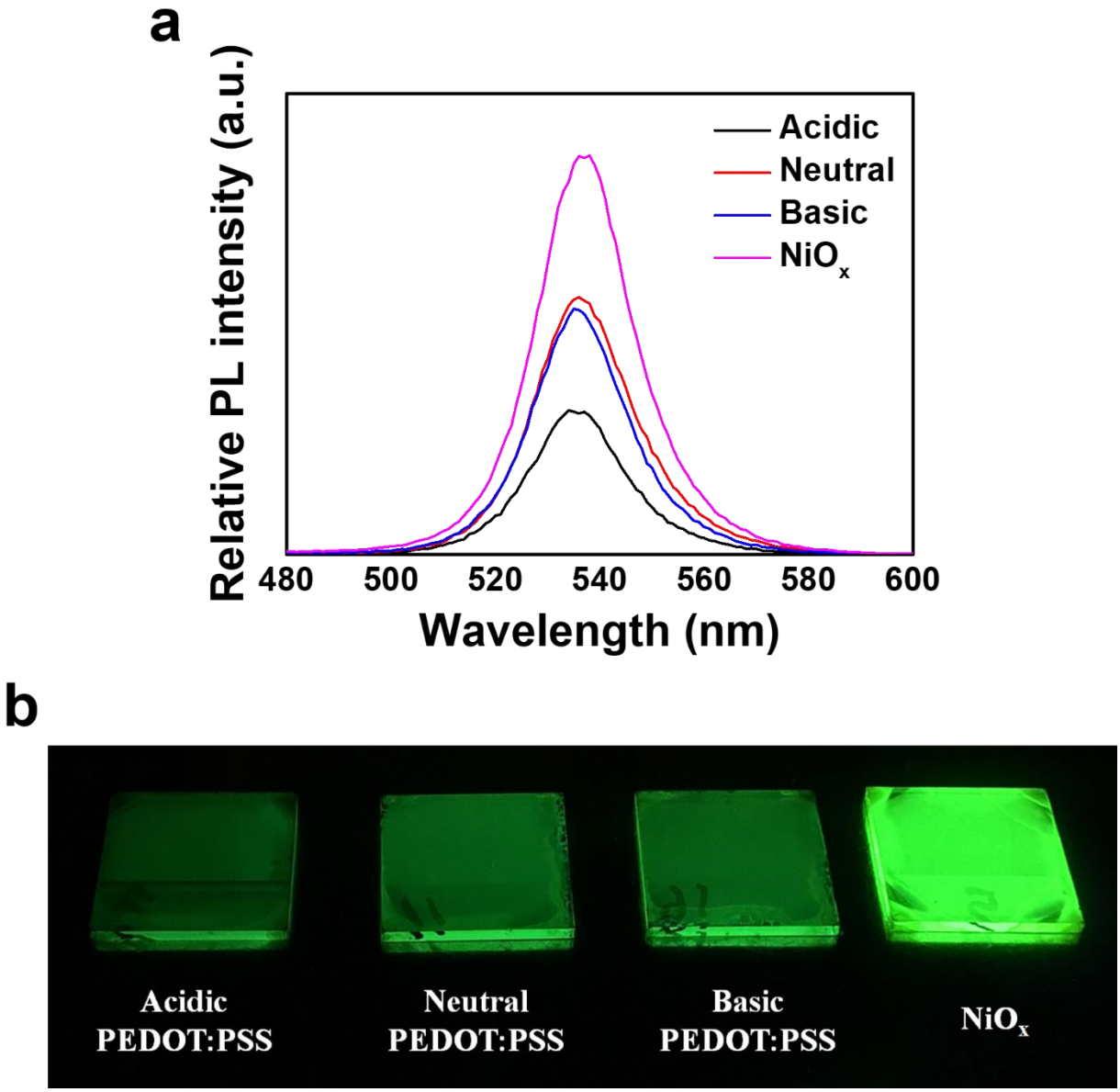

Figure 3.9. Optical properties of perovskite films deposited on NiO_x and PEDOT:PSS with different pH values. a) Steady-state PL spectra and b) photographs showing the green PL emission of perovskite films deposited on NiO_x and PEDOT:PSS with different pH values.

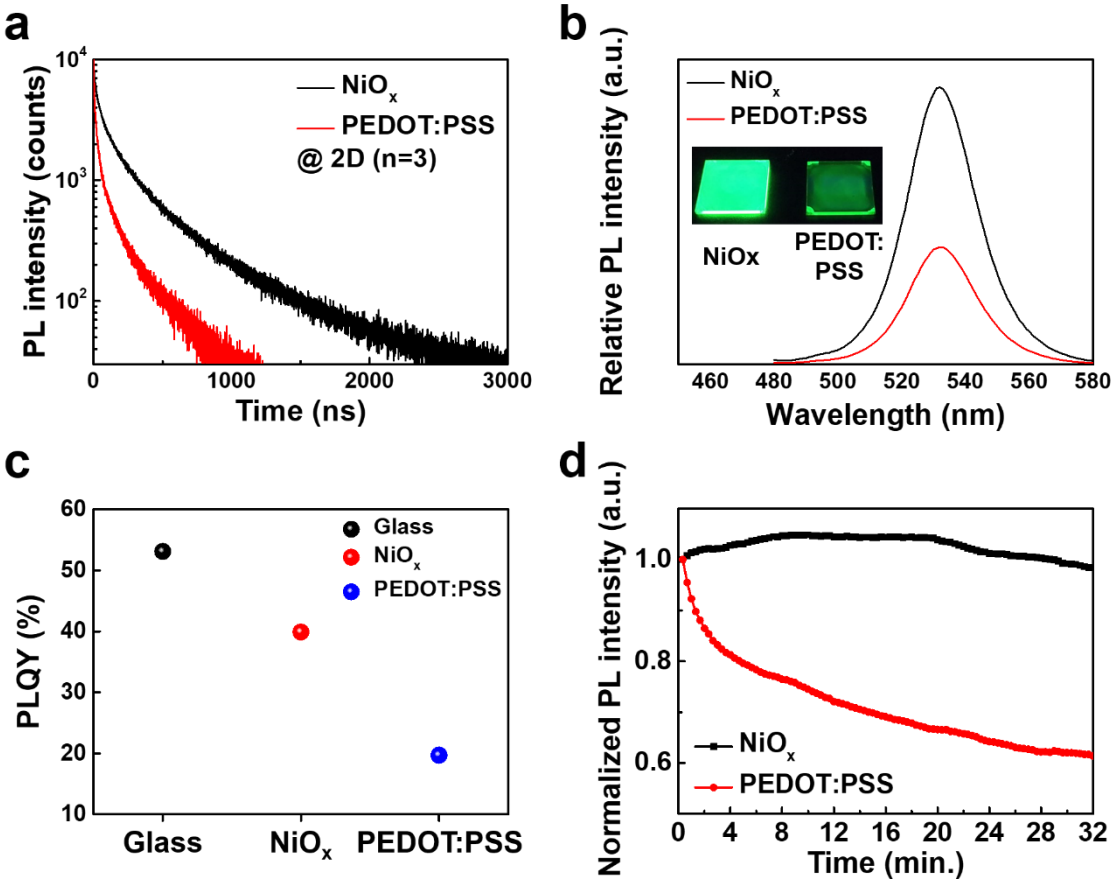

Figure 3.10. Optical properties and stability of perovskite films deposited on NiO_x and PEDOT:PSS. a) Time-resolved PL spectra, and b) steady-state PL spectra of quasi-2D perovskite with n = 3 deposited on NiO_x and PEDOT:PSS. c) PLQYs of quasi-2D perovskite with n = 3 deposited on glass, NiO_x, and PEDOT:PSS. d) Normalized PL intensity of quasi-2D perovskite with n = 3 deposited on NiO_x and PEDOT:PSS during excitation by a 405-nm laser as a function of time.

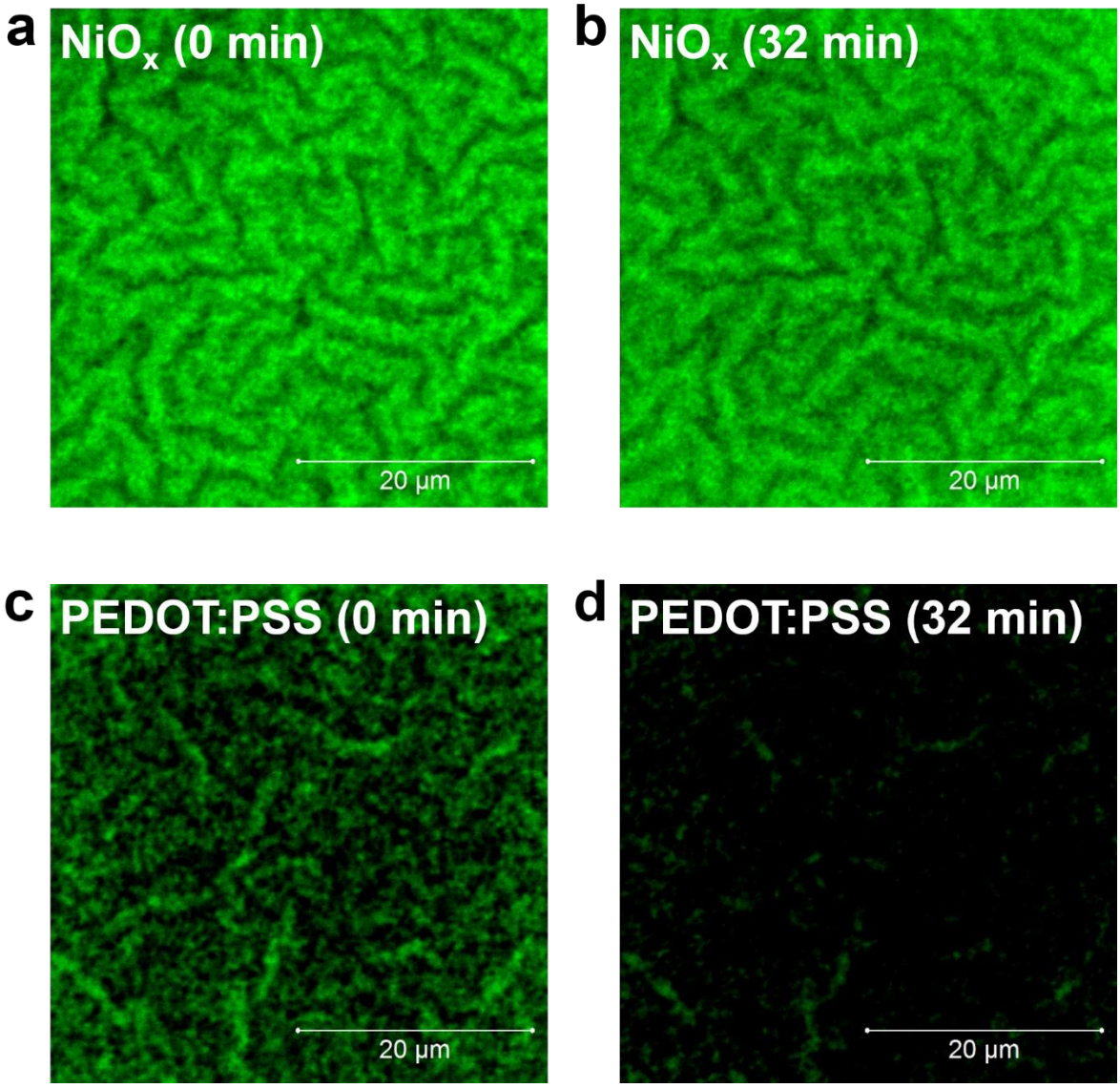

Figure 3.11. Optical Stability of perovskite films on NiO_x and PEDOT:PSS (confocal microscopy). Confocal PL images of quasi-2D perovskite with n = 3 deposited on NiO_x with excitation by a 405-nm laser after a) 0 min, and b) 32 min. Confocal PL images of quasi-2D perovskite with n = 3 deposited on PEDOT:PSS with excitation by a 405-nm laser excitation after c) 0 min, and d) 32 min.

The NiO_x films were optimized by testing different concentrations of precursor NiO_x solutions to balance the charge carriers through efficient hole transport and electron blocking (**Figure 3.12** and Table **3.2**). To investigate improved hole injection properties of NiO_x, We fabricated hole-only devices (ITO/NiO_x or PEDOT:PSS/$BA_2FA_2Pb_3Br_{10}$/TFB/MoO_3/Au) and electron-only device (ITO/ZnO/$BA_2FA_2Pb_3Br_{10}$/TPBi (60 nm)/LiF/Al) (**Figure 3.13**). The hole current density of hole-only device fabricated with NiO_x was higher than that with PEDOT:PSS, showing better hole injection properties when NiO_x is used as HTL in perovskite LEDs. Moreover, hole current density of hole-only

device fabricated with NiO_x was well matched with electron current density of electron-only device at the condition of 60 nm TPBi thickness.

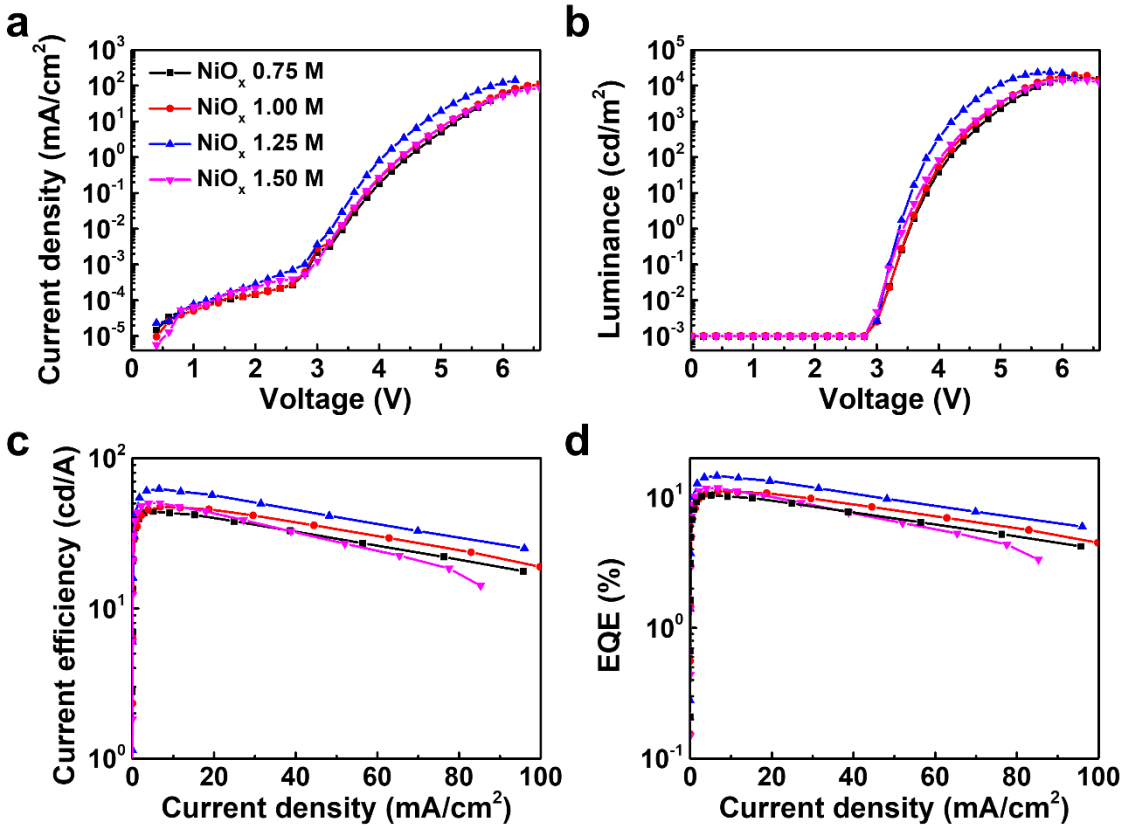

Figure 3.12. Device performance of PeLEDs fabricated with quasi-2D perovskite with n = 3 and different concentrations of NiO_x precursor. a) Current density versus voltage, b) luminance versus voltage, c) CE versus current density, and d) EQE versus current density of the PeLEDs fabricated with quasi-2D perovskite with n = 3 and different concentrations of NiO_x precursor.

The NiO_x films were optimized by testing different concentrations of the precursor NiO_x solution to balance the charge carriers through efficient hole transport and electron blocking. The performance of the device changed with the thickness of NiO_x. PeLEDs with an optimal concentration of the NiO_x precursor (1.25 M) exhibited the maximum luminance and efficiency, with balanced charge carriers in the perovskite layer.

Table 3.2. Summary of device performance of PeLEDs fabricated with quasi-2D perovskite with n = 3 and different concentrations of the NiO_x precursor.

Device configuration (PeLEDs)	L_{max} [cd/m²] @ bias	CE_{max} [cd/A] @ bias	EQE_{max} [%] @ bias	Turn-on voltage [V] @ 0.1 cd/m²
ITO / NiO_x (0.75 M) / $BA_2FA_2Pb_3Br_{10}$ / TPBi / LiF / Al	16,900 @ 6.4 V	44.1 @ 5.0 V	10.4 @ 5.0 V	3.2
ITO / NiO_x (1.00 M) / $BA_2FA_2Pb_3Br_{10}$ / TPBi / LiF / Al	19,600 @ 6.2 V	47.3 @ 5.0 V	11.1 @ 5.0 V	3.2
ITO / NiO_x (1.25 M) / $BA_2FA_2Pb_3Br_{10}$ / TPBi / LiF / Al	24,100 @ 5.8 V	62.4 @ 4.6 V	14.6 @ 4.6 V	3.2
ITO / NiO_x (1.50 M) / $BA_2FA_2Pb_3Br_{10}$ / TPBi / LiF / Al	14,700 @ 6.2 V	50.2 @ 5.0 V	11.8 @ 5.0 V	3.2

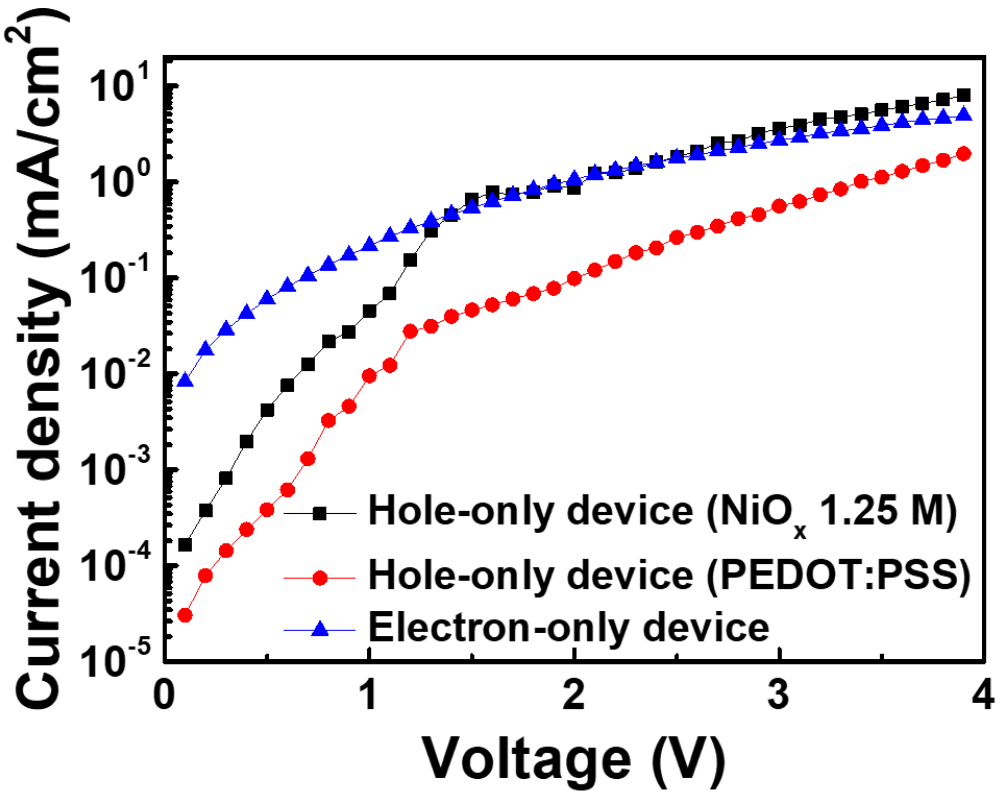

Figure 3.13. *J-V* characteristics of hole-only devices (ITO/NiO_x or PEDOT:PSS/$BA_2FA_2Pb_3Br_{10}$/TFB/MoO_3/Au) and electron-only device (ITO/ZnO/ $BA_2FA_2Pb_3Br_{10}$/TPBi (60 nm)/LiF/Al).

With the optimized precursor NiO_x solution (1.25 M), the current density, luminance, and device efficiency characteristics were measured for PeLEDs fabricated with different dimensionalities of perovskite (3D, n = 2, n = 3, and n = 5) deposited on NiO_x and the optimized dimensionality (n = 3) of the perovskite deposited on PEDOT:PSS (**Figure 3.14** and **Table 3.3**). As the dimensionality of the perovskites decreased, the current densities of the devices gradually decreased because high fraction of 2D to 3D perovskite interrupted charge transport. The optimized dimensionality (n = 3) of the perovskite enabled efficient and fast energy transfer in the radiative domains by outpacing trapping and the subsequent non-radiative recombination, leading to improved luminance and device efficiency. Using the dimensionality (n = 3) of the perovskite, the device characteristics of PeLEDs fabricated with NiO_x and PEDOT:PSS were compared. At low voltage, the PeLED fabricated with NiO_x recorded lower leakage of current density than that with PEDOT:PSS (**Figure 3.14** a). Moreover, the PeLED fabricated with NiO_x showed remarkably improved luminance (from 10,600 to 24,100 cd m^{-2}), CE (from 17.4 to 62.4 cd A^{-1}), and EQE (from 4.2 to 14.6%) compared with the PeLED fabricated with PEDOT:PSS. The obtained EQE of our green emissive device is 14.6%, which is comparable to the results reported so far (**Table 3.4**). Such significantly improved device performance is attributed to the better interface formed at NiO_x/perovskite layers with lower density of traps/defects, as well as more balanced charge carriers in the perovskite layer leading to high recombination yield of carriers.

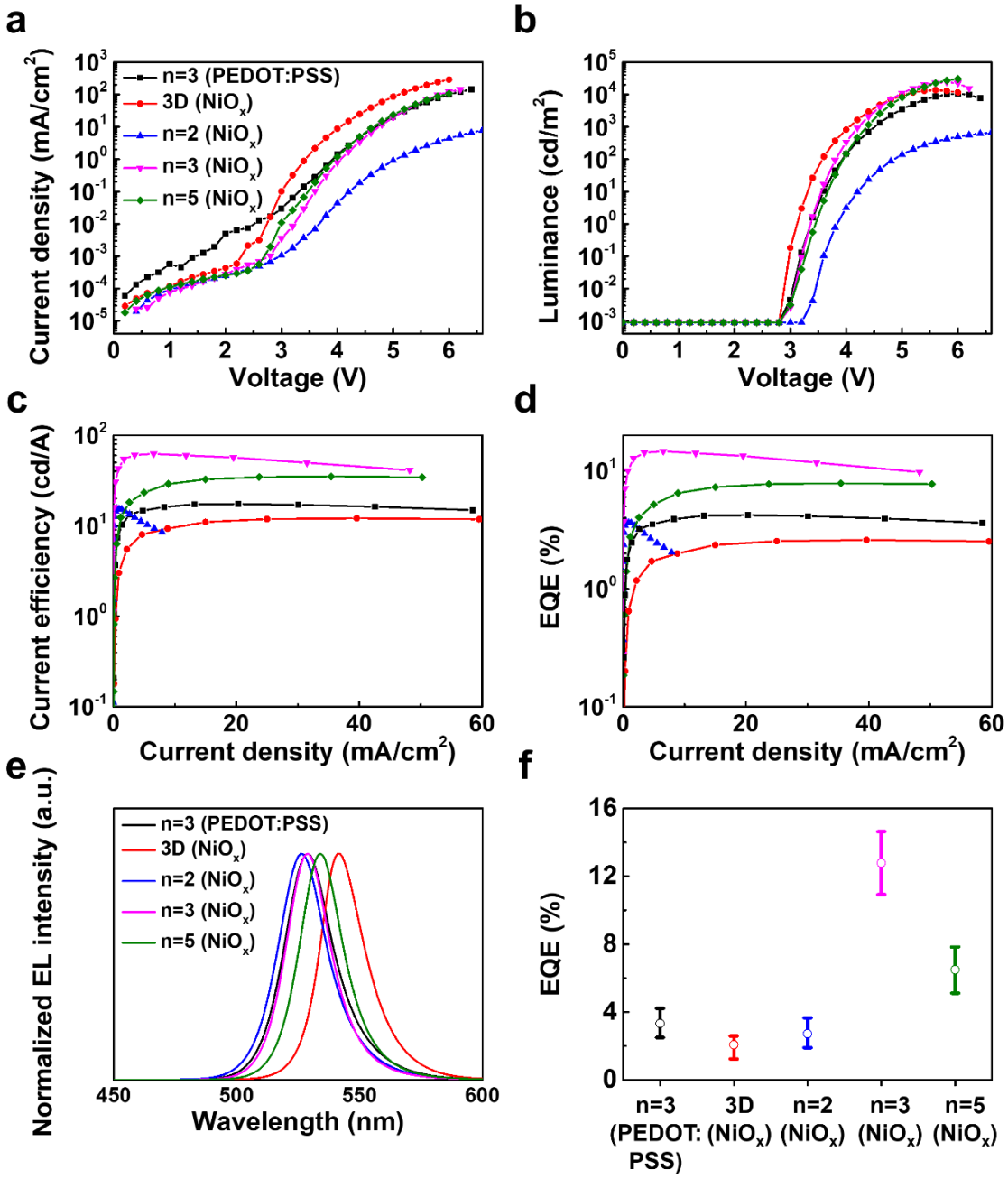

Figure 3.14. Device performance of PeLEDs fabricated with 3D $FAPbBr_3$ and quasi-2D perovskites with n = 2, 3, and 5 deposited on NiO_x and quasi-2D perovskite with n = 3 deposited on PEDOT:PSS. a) Current density versus voltage, b) luminance versus voltage, c) CE versus current density, d) EQE versus current density characteristics, e) normalized EL spectra, and f) EQE mean and deviation from each of 15 devices with 3D $FAPbBr_3$ and quasi-2D perovskites, with n = 2, 3, and 5 deposited on NiO_x and quasi-2D perovskite with n = 3 deposited on PEDOT:PSS.

Table 3.3. Summary of device performance of PeLEDs fabricated with 3D $FAPbBr_3$ and quasi-2D perovskites with n = 2, 3, and 5 deposited on NiO_x and quasi-2D perovskite with n = 3 deposited on PEDOT:PSS

Device configuration (PeLEDs)	**Luminance $_{max}$ [cd/m²] @ bias**	**CE $_{max}$ [cd/A] @ bias**	**EQE $_{max}$ [%] @ bias**	**EQE $_{avr}$ [%] from 15 devices**	**Turn-on voltage [V] @ 0.1 cd/m²**
ITO / PEDOT:PSS / $BA_2FA_2Pb_3Br_{10}$ (n=3) / TPBi / LiF /Al	10,600 @ 6.0 V	17.4 @ 5.0 V	4.22 @ 5.0 V	3.34	3.2
ITO / NiO_x / $FAPbBr_3$ / TPBi / LiF /Al	13,700 @ 5.6 V	12.1 @ 4.6 V	2.59 @ 4.6 V	2.08	3.0
ITO / NiO_x / $BA_2FAPb_2Br_7$ (n=2) / TPBi / LiF /Al	670 @ 6.6 V	15.5 @ 4.8 V	3.66 @ 4.8 V	2.74	3.6
ITO / NiO_x / $BA_2FA_2Pb_3Br_{10}$ (n=3) / TPBi / LiF /Al	24,100 @ 5.8 V	62.4 @ 4.6 V	14.64 @ 4.6 V	12.79	3.2
ITO / NiO_x / $BA_2FA_4Pb_5Br_{16}$ (n=5) / TPBi / LiF /Al	30,600 @ 6.0 V	35.1 @ 5.2 V	7.84 @ 5.2 V	6.50	3.2

The low interaction energy of perovskite allows many defects to easily form, leading to ion migration. The operational instability of PeLEDs may be due to the decomposition and interaction of perovskite with adjacent layers caused by ion migration. Defect-less perovskite and adjacent layers can substantially improve operational stability. The operational stability of PeLEDs fabricated with quasi-2D perovskite with n=3 deposited on NiO_x and PEDOT:PSS with encapsulation was measured at a luminance of 100 cd m^{-2} under ambient conditions as a function of operation time (**Figure 3.15** a). The PeLED fabricated with NiO_x exhibited remarkably improved operational stability compared with the PeLED fabricated with PEDOT:PSS. The PeLEDs fabricated with NiO_x retained up to 90% and 50% of its initial luminance until 95 and 102 minutes, whereas the PeLED fabricated with PEDOT:PSS exhibited a sharp drop to less than 10% of the initial luminance within 8 minutes. Moreover, the EL spectra and CIE coordinates of PeLEDs fabricated with PEDOT:PSS and NiO_x were measured to investigate the phase stability of quasi-2D perovskite (**Figure 3.16**). The EL spectra and CIE coordinates of both devices do not change over operating time, indicating the phase stability of FA-based quasi-2D perovskite. The instability of the PeLED fabricated with PEDOT:PSS may have been due to the acidic and hydroscopic nature of PEDOT:PSS as well as many interface defects between the perovskite and PEDOT:PSS. To investigate the effect of the defects in perovskite on device stability, EL microscope images of PeLEDs fabricated with NiO_x and PEDOT:PSS were recorded over time (**Figure 3.15** b). The EL images of PeLED fabricated with NiO_x showed bright emissions in all regions, where the brightness decreased over time. By contrast, the electroluminescence (EL) images of PeLED

fabricated with PEDOT:PSS revealed large dark regions regarded as defects, and particularly brighter emissions near the dark regions. Brightness in boundaries of the dark regions slowly decreased compared with other regions over time. Regions of brightest near the defects showed a drastic reduction, forming the darkest regions. Although the exact mechanism of the phenomenon is challenging to probe and still under investigation, defects in the perovskite obviously impinge on the operational stability of PeLEDs.

3.4 Conclusion

In summary, we tested a high-quality perovskite emitter with enhanced optical properties and thermal stability through compositional and dimensional modulations. $FAPbBr_3$ showed a longer PL lifetime and higher PL intensity compared to $MAPbBr_3$, owing to its low trap density. The dimensional modulation of FA-based perovskite enabled long-living free carriers to recombine in small radiative domains through efficient and fast energy transfer, which substantially improved the PL intensity with improvement of PLQY to 53.1%. Moreover, we investigated the energetics and trap density of states at the interface between the perovskite and HTL (NiO_x and PEDOT:PSS). The NiO_x film allowed the growth of highly crystalline perovskite with reduced trap density of states compared with PEDOT:PSS, which led to enhanced optical properties, the photostability of perovskite, and the operational stability of the PeLEDs. With effective control over the trap density of perovskite, efficient and stable green emissive PeLEDs with a maximum luminance of 24,100 cd m^{-2}, a maximum CE of 62.4 cd A^{-1}, and a maximum EQE of 14.6% were achieved.

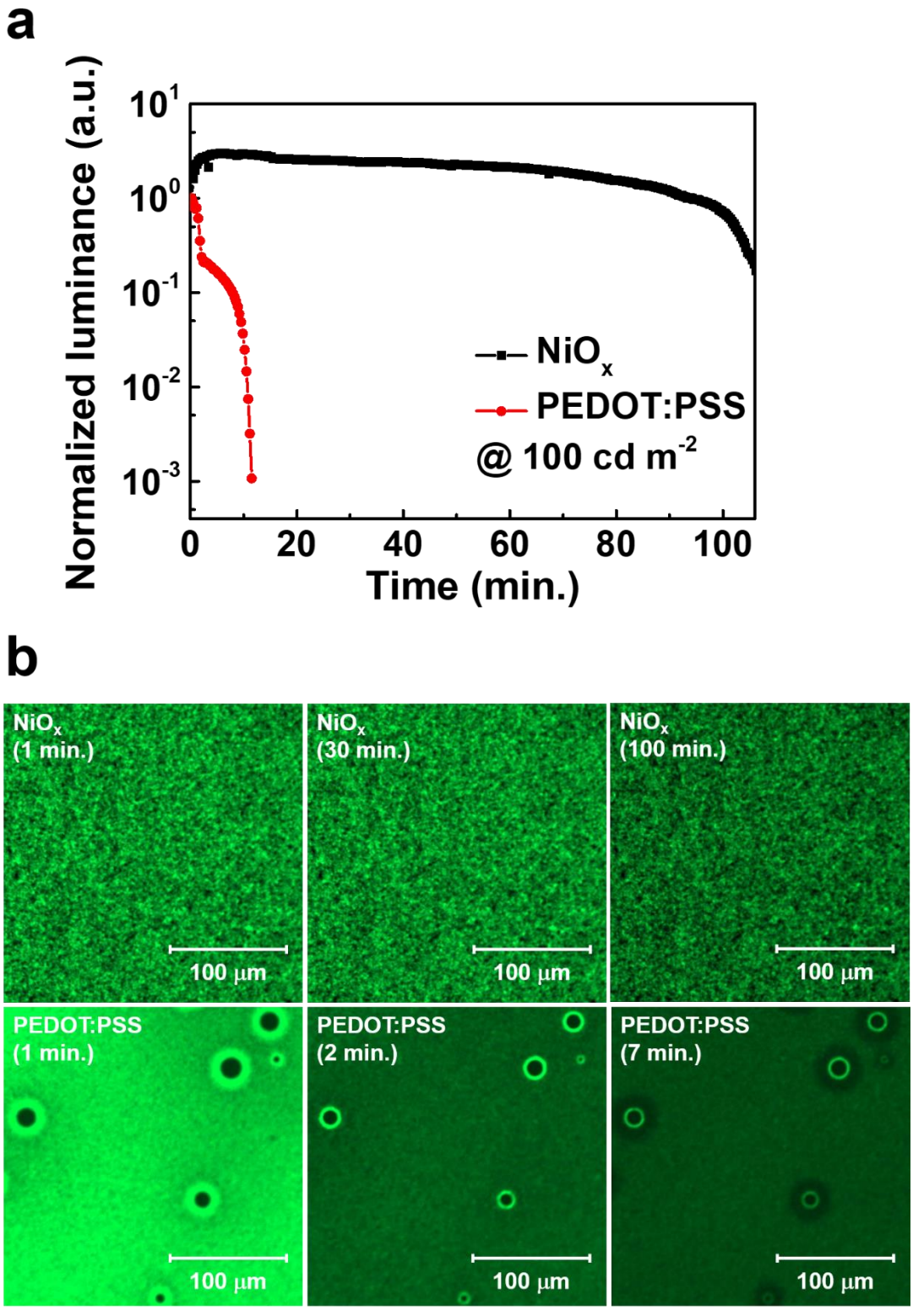

Figure 3.15. Operational stability and EL microscopic images of PeLEDs fabricated with quasi-2D perovskite with n = 3 deposited on NiO_x and PEDOT:PSS. a) Normalized luminance and b) EL microscope images of encapsulated PeLEDs fabricated with quasi-2D perovskite with n = 3 deposited on NiO_x and PEDOT:PSS as a function of operating time under ambient conditions.

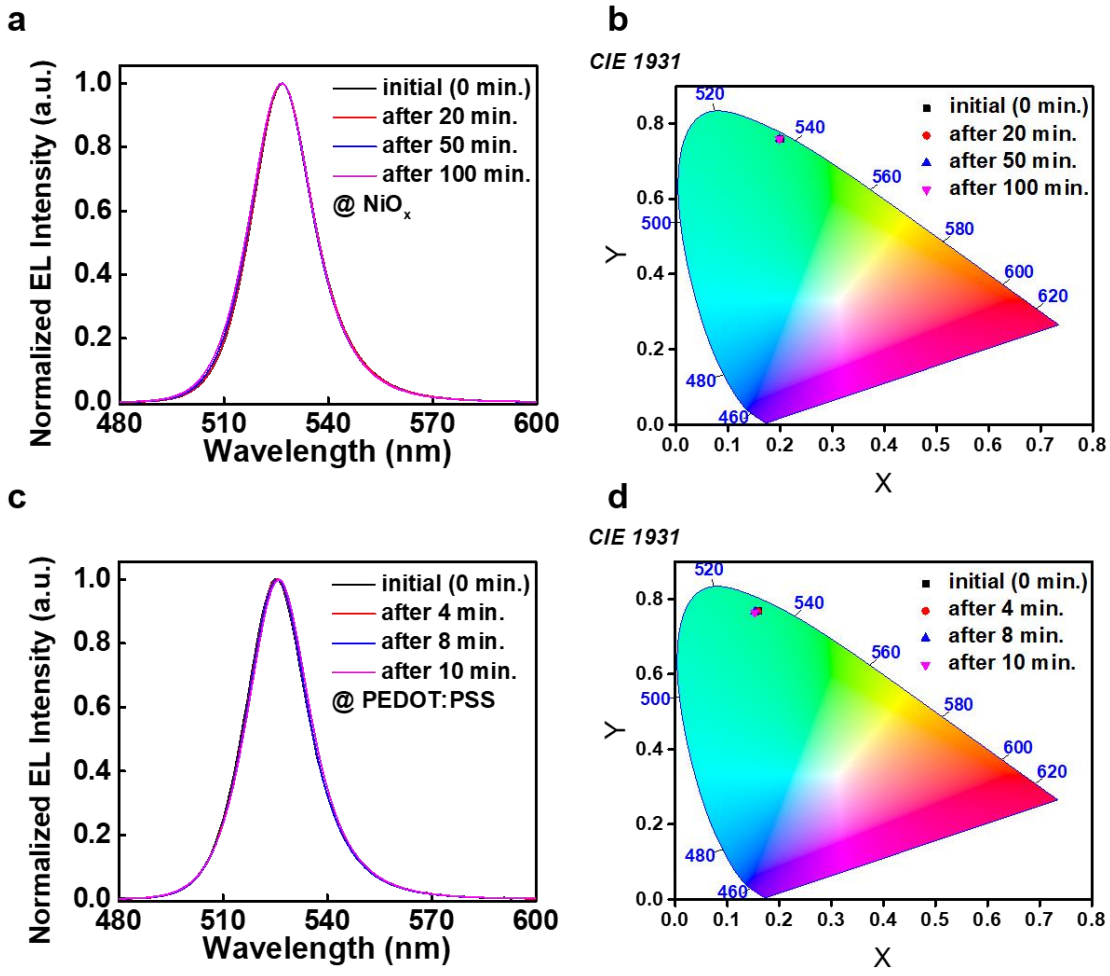

Figure 3.16. EL spectral stability of PeLEDs fabricated with NiO_x as a function of operating time under ambient conditions. a) Normalized EL spectra and b) CIE coordinates of PeLEDs fabricated with NiO_x as over operating time. c) Normalized EL spectra and d) CIE coordinates of PeLEDs fabricated with PEDOT:PSS as over operating time.

Publication year/month	Device structure	Emission wavelength	Max. EQE (%)	Max. CE (cd/A)	Max. L (cd/m^2)	Device Stability	Ref.
	ITO/NiO_x/$BA_2FA_2Pb_3Br_{10}$/ TPBi/LiF/Al	543nm	14.64	62.4	24,100	L_{90}≈95 min. L50≈102 min.	**Our work**
2015/12	PEDOT:PSS:PFI/$CH_3NH_3PbBr_3$/TPBi/LiF/Al	543nm	8.53	45.9	~20,000	-	[1]
2017/01	ITO/PVK/BA($MAPbBr_3$)$_2$PbBr$_4$/TPBi/LIF/Al	513nm	9.3	17.1	2,900	L_{50} ≈ 48min.	[2]
2017/03	ITO/PEDOT:PSS/$MAPbBr_3$/TPBi/LiF/Al	540nm	8.21	34.46	6,950	L_{50} ≈ 100 sec.	[3]
2017/04	ITO/PEDOT:PSS/$MAPbBr_3$/EDA/ SPW-111/LiF/Al	540nm	6.2	28.9	22,800	L_{70} ≈ 4h.	[4]
2017/06	ITO/ZnO/PVP/$Cs_{0.87}MA_{0.13}PbBr_3$/CBP/MoO_3/Al	520nm	10.43	33.9	91,000	L_{50} ≈ 60min.	[5]
2018/02	ITO/mPEDOT:PSS/PEA_2($FAPbBr_3$)$_2$$PbBr_4$/TPBi/LiF/ Al	532nm	14.36	62.43	9,120	L_{50} ≈ 60min.	[6]
2018/05	ITO/PEDOT:PSS/$MAPbBr_3$/TPBi/LiF/Al	538nm	12.1	55.2	55,400	L_{50} ≈ 60min.	[7]

Reference for Supporting Information

[1] H. C. Cho, S. H. Jeong, M. H. Park, Y. H. Kim, C. Wolf, C. L. Lee, J. H. Heo, A. Sadhanala, N. Myoung, S. Yoo, S. H. Im, R. H. Friend, T. W. Lee, *Science* **2015**, *350*, 1222.

[2] Z. G. Xiao, R. A. Kerner, L. F. Zhao, N. L. Tran, K. M. Lee, T. W. Koh, G. D. Scholes, B. P. Rand, *Nat. Photon.* **2017**, *11*, 108.

[3] J. W. Lee, Y. J. Choi, J. M. Yang, S. Ham, S. K. Jeon, J. Y. Lee, Y. H. Song, E. K. Ji, D. H. Yoon, S. Seo, H. Shin, G. S. Han, H. S. Jung, D. Kim, N. G. Park, *ACS Nano* **2017**, *11*, 3311.

[4] S. J. Lee, J. H. Park, B. R. Lee, E. D. Jung, J. C. Yu, D. Di Nuzzo, R. H. Friend, M. H. Song, *J. Phys. Chem. Lett.* **2017**, *8*, 1784.

[5] L. Q. Zhang, X. L. Yang, Q. Jiang, P. Y. Wang, Z. G. Yin, X. W. Zhang, H. R. Tan, Y. Yang, M. Y. Wei, B. R. Sutherland, E. H. Sargent, J. B. You, *Nat. Commun.* **2017**, *8*, 15640.

[6] X. L. Yang, X. W. Zhang, J. X. Deng, Z. M. Chu, Q. Jiang, J. H. Meng, P. Y. Wang, L. Q. Zhang,

Z. G. Yin, J. B. You, *Nat. Commun.* **2018**, *9*, 570.

[7] S. Lee, J. H. Park, Y. S. Nam, B. R. Lee, B. D. Zhao, D. Di Nuzzo, E. D. Jung, H. Jeon, J. Y. Kim, H. Y. Jeong, R. H. Friend, M. H. Song, *ACS Nano* **2018**, *12*, 3417.

3.5 References

[1] H. C. Cho, S. H. Jeong, M. H. Park, Y. H. Kim, C. Wolf, C. L. Lee, J. H. Heo, A. Sadhanala, N. Myoung, S. Yoo, S. H. Im, R. H. Friend, T. W. Lee, *Science* **2015**, *350*, 1222.

[2] Z. K. Tan, R. S. Moghaddam, M. L. Lai, P. Docampo, R. Higler, F. Deschler, M. Price, A. Sadhanala, L. M. Pazos, D. Credgington, F. Hanusch, T. Bein, H. J. Snaith, R. H. Friend, *Nat. Nanotech.* **2014**, *9*, 687.

[3] S. J. Lee, J. H. Park, B. R. Lee, E. D. Jung, J. C. Yu, D. Di Nuzzo, R. H. Friend, M. H. Song, *J. Phys. Chem. Lett.* **2017**, *8*, 1784.

[4] Z. G. Xiao, R. A. Kerner, L. F. Zhao, N. L. Tran, K. M. Lee, T. W. Koh, G. D. Scholes, B. P. Rand, *Nat. Photon.* **2017**, *11*, 108.

[5] M. J. Yuan, L. N. Quan, R. Comin, G. Walters, R. Sabatini, O. Voznyy, S. Hoogland, Y. B. Zhao, E. M. Beauregard, P. Kanjanaboos, Z. H. Lu, D. H. Kim, E. H. Sargent, *Nat. Nanotech.* **2016**, *11*, 872.

[6] X. L. Yang, X. W. Zhang, J. X. Deng, Z. M. Chu, Q. Jiang, J. H. Meng, P. Y. Wang, L. Q. Zhang, Z. G. Yin, J. B. You, *Nat. Commun.* **2018**, *9*, 570.

[7] W. Zou, R. Z. Li, S. T. Zhang, Y. L. Liu, N. N. Wang, Y. Cao, Y. F. Miao, M. M. Xu, Q. Guo, D. W. Di, L. Zhang, C. Yi, F. Gao, R. H. Friend, J. P. Wang, W. Huang, *Nat. Commun.* **2018**, *9*, 608.

[8] S. D. Stranks, V. M. Burlakov, T. Leijtens, J. M. Ball, A. Goriely, H. J. Snaith, *Phys. Rev. Appl.* **2014**, *2*, 034007.

[9] Y. Yang, M. J. Yang, Z. Li, R. Crisp, K. Zhu, M. C. Beard, *J. Phys. Chem. Lett.* **2015**, *6*, 4688.

[10] F. C. Hanusch, E. Wiesenmayer, E. Mankel, A. Binek, P. Angloher, C. Fraunhofer, N. Giesbrecht, J. M. Feckl, W. Jaegermann, D. Johrendt, T. Bein, P. Docampo, *J. Phys. Chem. Lett.* **2014**, *5*, 2791.

[11] A. A. Zhumekenov, M. I. Saidaminov, M. A. Haque, E. Alarousu, S. P. Sarmah, B. Murali, I. Dursun, X. H. Miao, A. L. Abdelhady, T. Wu, O. F. Mohammed, O. M. Bakr, *ACS Energy Lett.* **2016**, *1*, 32.

[12] C. Motta, F. El-Mellouhi, S. Sanvito, *Phys. Rev. B* **2016**, *93*, 235412.

[13] Q. F. Han, S. H. Bae, P. Y. Sun, Y. T. Hsieh, Y. Yang, Y. S. Rim, H. X. Zhao, Q. Chen, W. Z. Shi, G. Li, Y. Yang, *Adv. Mater.* **2016**, *28*, 2253.

[14] W. Rehman, R. L. Milot, G. E. Eperon, C. Wehrenfennig, J. L. Boland, H. J. Snaith, M. B. Johnston, L. M. Herz, *Adv. Mater.* **2015**, *27*, 7938.

[15] J. W. Jung, C. C. Chueh, A. K. Y. Jen, *Adv. Mater.* **2015**, *27*, 7874.

[16] B. R. Lee, S. Lee, J. H. Park, E. D. Jung, J. C. Yu, Y. S. Nam, J. Heo, J. Y. Kim, B. S. Kim, M. H. Song, Adv. Mater. **2015**, *27*, 3553.

[17] M. Moriya, D. Hirotani, T. Ohta, Y. Ogomi, Q. Shen, T. S. Ripolles, K. Yoshino, T. Toyoda, T. Minemoto, S. Hayase, *ChemSusChem* **2016**, *9*, 2634.

[18] T. S. Sherkar, C. Momblona, L. Gil-Escrig, J. Avila, M. Sessolo, H. J. Bolink, L. J. A. Koster, *ACS Energy Lett.* **2017**, *2*, 1214.

[19] J. Peng, Y. Wu, W. Ye, D. A. Jacobs, H. Shen, X. Fu, Y. Wan, T. Duong, N. Wu, C. Barugkin, H. T. Nguyen, D. Zhong, J. Li, T. Lu, Y. Liu, M. N. Lockrey, K. J. Weber, K. R. Catchpolea, T. P. White, *Energy Environ. Sci.* **2017**, *10*, 1792.

[20] H. R. Tan, A. Jain, O. Voznyy, X. Z. Lan, F. P. G. de Arquer, J. Z. Fan, R. Quintero-Bermudez, M. J. Yuan, B. Zhang, Y. C. Zhao, F. J. Fan, P. C. Li, L. N. Quan, Y. B. Zhao, Z. H. Lu, Z. Y. Yang, S. Hoogland, E. H. Sargent, *Science* **2017**, *355*, 722.

[21] W. Y. Nie, H. H. Tsai, J. C. Blancon, F. Z. Liu, C. C. Stoumpos, B. Traore, M. Kepenekian, O. Durand, C. Katan, S. Tretiak, J. Crochet, P. M. Ajayan, M. G. Kanatzidis, J. Even, A. D. Mohite, *Adv. Mater.* **2018**, *30*, 1703879.

[22] M. Jorgensen, K. Norrman, S. A. Gevorgyan, T. Tromholt, B. Andreasen, F. C. Krebs, *Adv. Mater.* **2012**, *24*, 580.

[23] H. Choi, C. K. Mai, H. B. Kim, J. Jeong, S. Song, G. C. Bazan, J. Y. Kim, A. J. Heeger, *Nat. Commun.* **2015**, *6*, 7348.

[24] J. M. Yun, J. S. Yeo, J. Kim, H. G. Jeong, D. Y. Kim, Y. J. Noh, S. S. Kim, B. C. Ku, S. I. Na, *Adv. Mater.* **2011**, *23*, 4923.

[25] Y. K. Chih, J. C. Wang, R. T. Yang, C. C. Liu, Y. C. Chang, Y. S. Fu, W. C. Lai, P. Chen, T. C. Wen, Y. C. Huang, C. S. Tsao, T. F. Guo, *Adv. Mater.* **2016**, *28*, 8687.

[26] W. Chen, Y. Z. Wu, Y. F. Yue, J. Liu, W. J. Zhang, X. D. Yang, H. Chen, E. B. Bi, I. Ashraful, M. Gratzel, L. Y. Han, *Science* **2015**, *350*, 944.

[27] N. Arora, M. I. Dar, A. Hinderhofer, N. Pellet, F. Schreiber, S. M. Zakeeruddin, M. Gratzel, *Science* **2017**, *358*, 768.

[28] J. Y. Jeng, K. C. Chen, T. Y. Chiang, P. Y. Lin, T. D. Tsai, Y. C. Chang, T. F. Guo, P. Chen, T. C. Wen, Y. J. Hsu, *Adv. Mater.* **2014**, *26*, 4107.

[29] Z. Wang, Z. Luo, C. Zhao, Q. Guo, Y. Wang, F. Wang, X. Bian, A. Alsaedi, T. Hayat, Z. a. Tan, *J. Phys. Chem. C* **2017**, *121*, 28132.

[30] Z. Shi, S. Li, Y. Li, H. Ji, X. Li, D. Wu, T. Xu, Y. Chen, Y. Tian, Y. Zhang, C. Shan, G. Du, *ACS Nano* **2018**, *12*, 1462.

[31] H. Ji, Z. Shi, X. Sun, Y. Li, S. Li, L. Lei, D. Wu, T. Xu, X. Li, G. Du, *ACS Appl. Mater. Interfaces* **2017**, *9*, 42893.

[32] M. K. Gangishetty, S. Hou, Q. Quan, D. N. Congreve, *Adv. Mater.* **2018**, *30*, 1706226.

[33] F. Cao, H. Wang, P. Shen, X. Li, Y. Zheng, Y. Shang, J. Zhang, Z. Ning, X. Yang, *Adv. Funct. Mater.* **2017**, *27*, 1704278.

[29] J. A. Venables, G. D. T. Spiller, M. Hanbucken, *Rep. Prog. Phys.* **1984**, *47*, 399.

[30] D. E. Wolf, J. Villain, *Europhys. Lett.* **1990**, *13*, 389.

[31] A. Amat, E. Mosconi, E. Ronca, C. Quarti, P. Umari, M. K. Nazeeruddin, M. Gratzel, F. De Angelis, *Nano Lett.* **2014**, *14*, 3608.

[32] G. E. Eperon, S. D. Stranks, C. Menelaou, M. B. Johnston, L. M. Herz, H. J. Snaith, *Energy Environ. Sci.* **2014**, *7*, 982.

[33] B. I. D., G. Angela, S. James, L. Jamie, *Phys. Status Solidi S* **2015**, *12*, 259.

[34] I. D. Baikie, A. C. Grain, J. Sutherland, J. Law, *Energy Procedia* **2014**, *60*, 48.

[35] J. R. Harwell, T. K. Baikie, I. D. Baikie, J. L. Payne, C. Ni, J. T. S. Irvine, G. A. Turnbull, I. D. W. Samuel, *Phys. Chem. Chem. Phys.* **2016**, *18*, 19738.

[36] E. M. Miller, Y. X. Zhao, C. C. Mercado, S. K. Saha, J. M. Luther, K. Zhu, V. Stevanovic, C. L. Perkins, J. van de Lagemaat, *Phys. Chem. Chem. Phys.* **2014**, *16*, 22122.

[37] C. S. Jiang, M. J. Yang, Y. Y. Zhou, B. To, S. U. Nanayakkara, J. M. Luther, W. L. Zhou, J. J. Berry, J. van de Lagemaat, N. P. Padture, K. Zhu, M. M. Al-Jassim, *Nat. Commun.* **2015**, *6*, 8397.

[38] L. Kronik, Y. Shapira, *Surf. Interface Anal.* **2001**, *31*, 954.

[39] W. Zhang, S. Pathak, N. Sakai, T. Stergiopoulos, P. K. Nayak, N. K. Noel, A. A. Haghighirad, V. M. Burlakov, D. W. deQuilettes, A. Sadhanala, W. Z. Li, L. D. Wang, D. S. Ginger, R. H. Friend, H. J. Snaith, *Nat. Commun.* **2015**, *6*, 10030.

Chapter 4. Efficient Large-Area Cesium-Based Quasi-2D Perovskite Light-Emitting Diodes Using Hot-Casting Mthods.

4.1 Research back ground

Metal halide perovskite have been actively studied for next generation light-emitting diodes (LEDs) and lasing source due to their high color purity, color tunability, low trap density, easy process and high photoluminescence quantum yield (PLQY)[1-7]. Based on these properties, the perovskite LEDs (PeLEDs) has continued to efficiency develop and recently reported an external quantum efficiency (EQE) over 20%[8-11]. The perovskite materials have attracted attention as a next generation display material. However, the low exciton binding energy (<50meV)[12, 13] of perovskite cause defect-induced nonradiative recombination in the trap site during device operation, which has resulted in decreased an EQE of the PeLEDs. Low dimensional quasi-2D perovskite with the multi quantum well using inserting bulky ammonium halide cation can effectively concentrate charge into the smaller band gap through the charge cascade[14-16]. This concentrated charge has been reported to increases the charge recombination probability, allowing a high PLQY which is not dependent on excitation intensity and high efficiency of the PeLEDs.

However, since the perovskites usually have relatively deep valance band maximums (VBMs) (e.g., $CsPbBr_3$: 5.8-6.3 eV)[17-20] compared to ITO anode (~4.7 eV), PeLEDs design for efficient charge balance injection is needed. The charge injection barrier between the charge injection layer and the perovskite film degrades the efficiency of device. Poly(3,4-ethylenedioxythiophene) polystyrene sulfonate (PEDOT:PSS), which is commonly used as a hole injection layer (HIL) in HIL/perovskite/electron injection layer (EIL) device structure, has a limitation of inefficient hole injection into VBMs of perovskite because work function of PEDOT:PSS shows relatively shallow value (5.0-5.2 eV). In this way, various interlayers with high highest occupied molecular orbital (HOMO) level such as Poly(9-vinylcarbazole) (PVK, HOMO: 5.8 eV)[21, 22], Poly(bis-4-butylphenyl-N,N-bisphenyl)benzidine (Poly TPD, HOMO: 5.2 eV)[22, 23], Poly(9,9-di-n-octylfluorenyl-2,7-diyl) (F8, HOMO: 5.8eV)[24], and Poly(9,9-dioctylfluorene-alt-N-(4-sec-butylphenyl)-diphenylamine) (TFB, HOMO: 5.3eV)[25, 26] have been studied. Nevertheless, the perovskites grown on these conjugated HIL with hydrophobic-branched alky group show not uniform with a lot of pinholes because the perovskite precursor solution has hydrophilic nature. The non-continuous perovskite films with pinholes lead to leakage current, therefore, it is necessary to make a dense and uniform morphology, regardless of the surface energy of the bottom layer.

Hot-casting method forming the perovskite film by applying the heat to the bottom substrate and precursor solution during spin casting. This method is advantageous in that it can form the uniform morphology without being affected by surface energy of bottom layer and the grown perovskite film

shows high crystallinity. This is because thermal energy of substrate reduced the surface tension between perovskite precursor solution and bottom layer and increase the diffusion of the precursors. In conclusion, the hot-casting method enables faster perovskite crystal growth. The hot-casting method has succeeded in realizing a high efficiency solar cell by increasing the grain size of perovskite and improving the perovskite crystallinity.[27, 28] Cheng Bi et al. reported that a continuous pinhole-free perovskite film was fabricated on a hydrophobic polymer bottom layer using a pre-heated hot perovskite precursor solution.[29]

This hot-casting method is also applied to fabricate large-area devices because it does not require solvent washing process and can make perovskite films with good morphology and high crystallinity using spin-coating[30], slot-die coating[31], blade-coating[32-34], spray coating[35-37] and dipping coating[30]. Recently, in the case of low dimensional perovskite system (2D and quasi-2d), the pre-heated substrate not only affects morphology and crystallinity, but also helps the orientation of perovskite crystal grow in preferred direction. The preferred aligned perovskite crystals in the vertical direction facilitate charge transport and contribute to radiative recombination enhancement.[38-40]

Here, we introduce the Poly(9-vinylcarbazole) (PVK) interlayer between nickel oxide (NiO_x) layer and perovskite film for increasing the hole injection and recombination of charge carrier in PeLEDs. However, due to the hydrophobic nature of the introduced PVK interlayer, it is difficult to fabricate uniform and pinhole-free perovskite morphology. One of the methods of making perovskite films, a hot-casting method using preheating substrate was used to produce uniform and full coverage of perovskite film morphology on the PVK interlayer. The hot-casting method improved the morphology of the perovskite film and increased the crystallinity and the preferred orientation of perovskite crystals in vertical direction. As a result, the PeLEDs of the optimal preheating substrate temperature shows a considerable enhanced device performance in the maximum EQE value from 3.08 % (at 4.2V) to 8.44 % (at 3.6V) compared to control PeLEDs using unheated substrate. Unlike the conventional anti-solvent dropping method, hot-casting method does not need a solvent washing process. The PeLEDs manufactured by the hot-casting method is advantageous in that the light-emitting surface is uniform and unspotted. We demonstrated the PeLEDs with a clean emitting active area of 12.8 cm^2 using the hot-casting method.

4.2 Experimental

Materials

The methyl ammonium bromide (MABr) was synthesized as described by previous reported. The SPW-111 polymer (white copolymer) was purchased from Merck Co. All reagent were used as purchased without further purification

PEDOT:MoO3 composite solution

PEDOT:MoO3 composite solution was realized by following process. A water dispersion PEDOT:PSS (AI 4083, Celvios) was filtered by 0.45 μm hydrophilic filter (PVDF filter), and then ammonium molybdate (NH4)2MoO4 (Sigma Aldrich) powder was added into PEDOT:PSS dispersion varying weight percent ratio from 0.001 wt.% to 0.007 wt.% under stirring.

Device fabrication

ITO/glass substrates were cleaned in sonication bath of distilled water, acetone, isopropyl alcohol, respectively for 10 min. And then treated UV-ozone for 10 min. PEDOT:PSS and PEDOT:MoO3 composite solution were spin-coated onto ITO/glass substrates as HTL and subsequently annealed at 145 oC for 10 min. The perovskite precursor (37.8 wt.%) with an aqueous HBr (48 wt.%) solution were spin-coated onto the PEDOT:PSS, PEDOT:MoO3-coated ITO/glass substrates at 3,000 rpm for 60 s and subsequently annealed at 60 oC for 2 hr under nitrogen (N2) atmosphere. The electron transport layer was spin-coated from SPW-111 dissolved in chlorobenzene. Finally, LiF (1 nm) and silver (80 nm) were deposited by the vacuum thermal evaporation method using a 5-pixel mask. The devices were encapsulated and legged before testing.

Characterisation of PEDOT:MoO3 composite film and PeLEDs

The PeLEDs tested using a keithely 2400 source measurement unit and a Konica Minolta spectroradiometer (CS-2000, Minolta Co.) under ambient air conditions. To observe morphology of MAPbBr3 films on the PEDOT:PSS and PEDOT:MoO3 composite layer were measured via scanning electron microscopy. The surface morphology of PEDOT:PSS and PEDOT:MoO3 composite layers was measured using atomic force microscopy (DI-3100, Veeco Co.). XPS and UPS spectra of PEDOT:MoO3 composite layer were conducted using ESCALAB 250XI (Thermo Fisher Scientific Co

4.4 Results and discousions

We fabricated cesium based quasi-2D PeLEDs with a configuration of indium tin oxide (ITO) /NiO_x/PVK/quasi-2d perovskite/2,2′,2"-(1,3,5-benzinetriyl)-tris(1-phenyl-1-H-benzimidazole (TPBi)/LiF/Al. **Figure 4.1** shows the cross-section image of PeLEDs. NiO_x (~50nm) was used as HIL, TPBi (~55nm) was used as EIL. ITO and LiF (1nm) / Al (~100nm) were chosen as the anode and cathode, respectively. Quasi-2d perovskite films (~70nm) as emissive layer was prepared by controlling stoichiometric quantity amounts of cesium bromide (CsBr), lead bromide ($PbBr_2$) and benzyl ammonium bromide (BABr). The optimized quasi-2d perovskite precursor molar ratio is used CsBr : $PbBr_2$: BABr of 1 : 1.25 : 0.6. For enhanced hole injection, PVK interlayer was introduced between NiO_x films and quasi-2D perovskite.

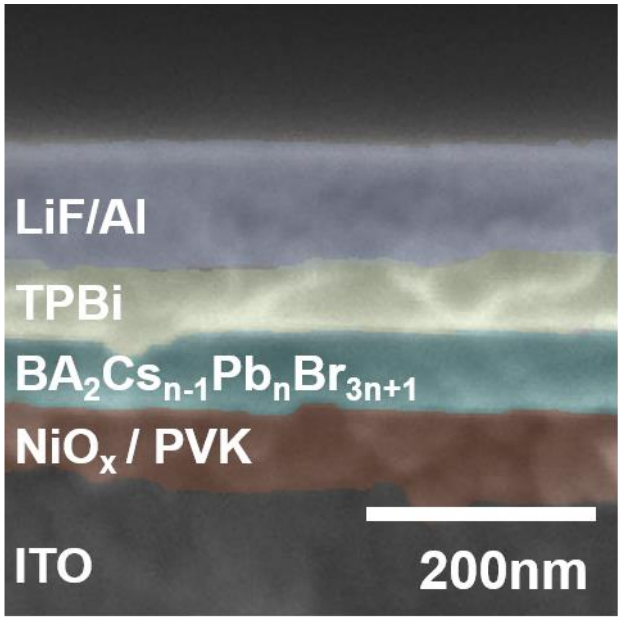

Figure 4.1. Cross section SEM images of Cs based quasi-2D PeLEDs

The ultraviolet photoemission spectroscopy (UPS) spectra of the NiO_x films and PVK layer coated NiO_x films show that HOMO level of PVK layer coated NiO_x films (5.75 eV) was deeper than that VBM of pristine NiO_x films (5.30eV). The measured VBMs value of quasi-2d perovskite film is 5.92 eV (**Figure 4.2**). This value is good agreement with the findings of previous reports. The 0.35 eV downward shifts of HOMO level of PVK layer coated NiO_x films indicate hole injection barrier at interface between HIL and quasi-2D perovskite was reduced. To confirm the enhancement of hole injection at the interface after introducing the PVK layer on NiO_x, the *J-V characteristic* of hole-only devices using different HIL layer were compared, as shown in **Figure 4.3**. The hole-only device with

PVK interlayer shows higher current density than the device without PVK interlayer. The energy level alignment of the PeLEDs is depicted in **Figure 4.4**.

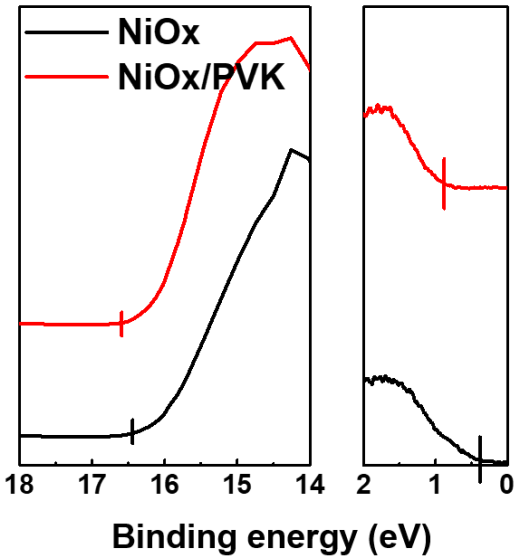

Figure 4.2. UPS spectras of NiOx film and NiOx/PVK film

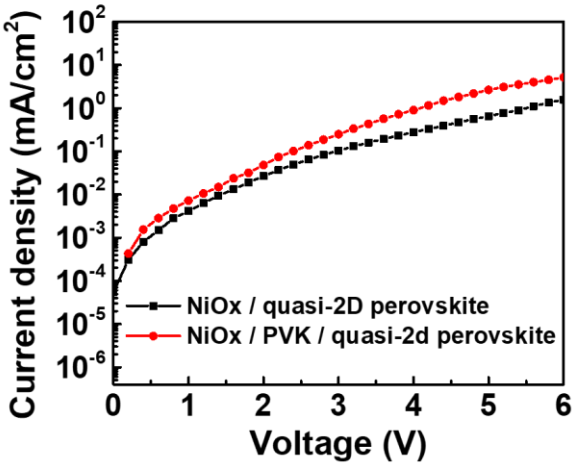

Figure 4.3 *J-V characteristic* of hole-only devices using different HIL layer

The similar absorption spectra of the PVK coated NiO_x films and NiO_x films was observed, as shown in **Figure 4.5**, which indicate that PVK coated NiOx films has only a difference in VBMs compared to NiOx films. However, the PVK layer has typically hydrophobic nature, which reduces the surface wettability between hydrophilic perovskite solution and PVK layer. **Figure 4.6** show the solvent contact angle on each bottom layer. The contact angle was measured on UV ozone treated NiO_x layer and PVK coated NiO_x layer for DMSO solvent. The contact angle of 10.2° on UV ozone treated NiO_x represents hydrophilic nature. In contrast to, the PVK coated NiO_x layer shows a relatively high contact angle of

84.7° and hydrophobic nature. The compatibility between bottom layer and perovskite solution affects the formation of perovskite film. The illustration of how the perovskite solution is coated on wetting NiO_x layer (Fig. 1e) and non-wetting PVK coated NiOx (**Figure 4.6**) is shown.

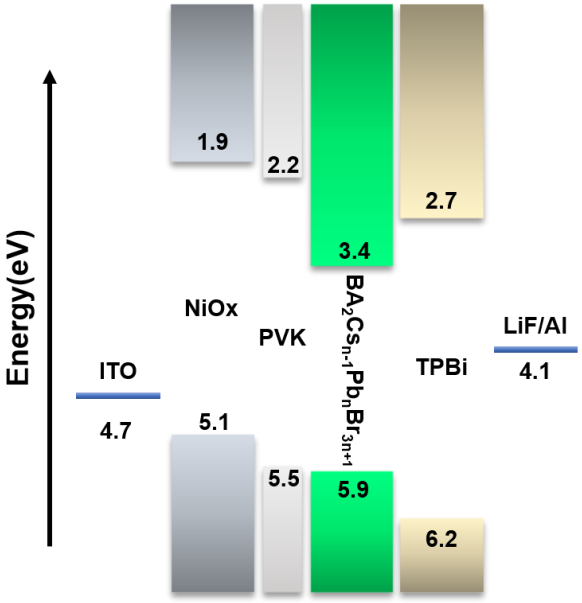

Figure 4.4 Energy level alingment of PeLEDs

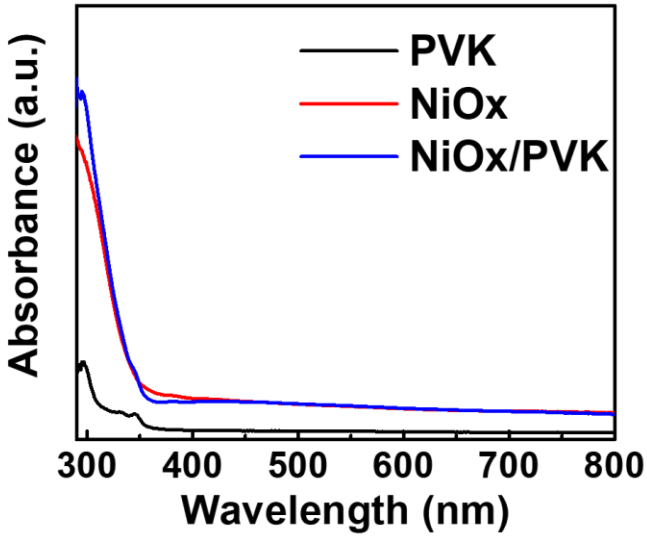

Figure 4.5 Absorption spetras for differnet hole injection layer

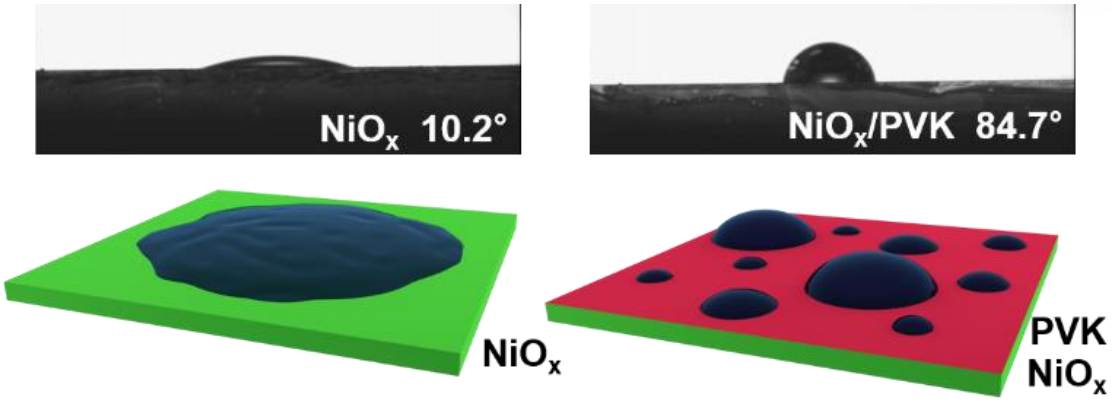

Figure 4.6 Contact angles of water droplet on UV ozone treated NiO_x layer and PVK coated NiO_x layer

To confirm the morphology of the quasi-2D perovskite film., quasi-2D perovskite film fabricated on PVK coated NiO_x layer was observed via a scanning electron microscope (SEM), as shown in **Figure 4.7**. The quasi-2D film grown on the PVK coated NiO_x layer exhibited rough morphology with large pinhole due to the non-wetting nature between the perovskite solution and the bottom PVK coated NiO_x layer. Whereas the quasi-2D perovskite film grown on the UVO treated NiO_x layer exhibited uniform and smooth morphology as shown **Figure 4.7**. To improve the poor morphology caused by the non-wetting nature on the hydrophobic PVK coated NiO_x layer, we introduced a hot casting method using preheated substrate. In the "hot casting" process, perovskite precursor solution with DMSO as a solvent is coated on a preheated substrate to crystalize rapidly. For the detailed hot casting method, see the experiment section. The temperature of the substrate was changed from room temperature (RT) to 120℃. As the temperature is increased on the substrate, the perovskite morphology shows less pinholes and a smoother uniform (**Figure 4.7**). The thermal energy of preheated substrate can accelerate the crystal growth rate and increases the diffusion length of precursor particle to enable uniform film formation. The perovskite films on a substrate with 120℃ or more begins to regenerate the pinhole, which is considered to be due to the thermal instability of the BA molecule and too fast solvent vaporization on the substrates above 120℃.

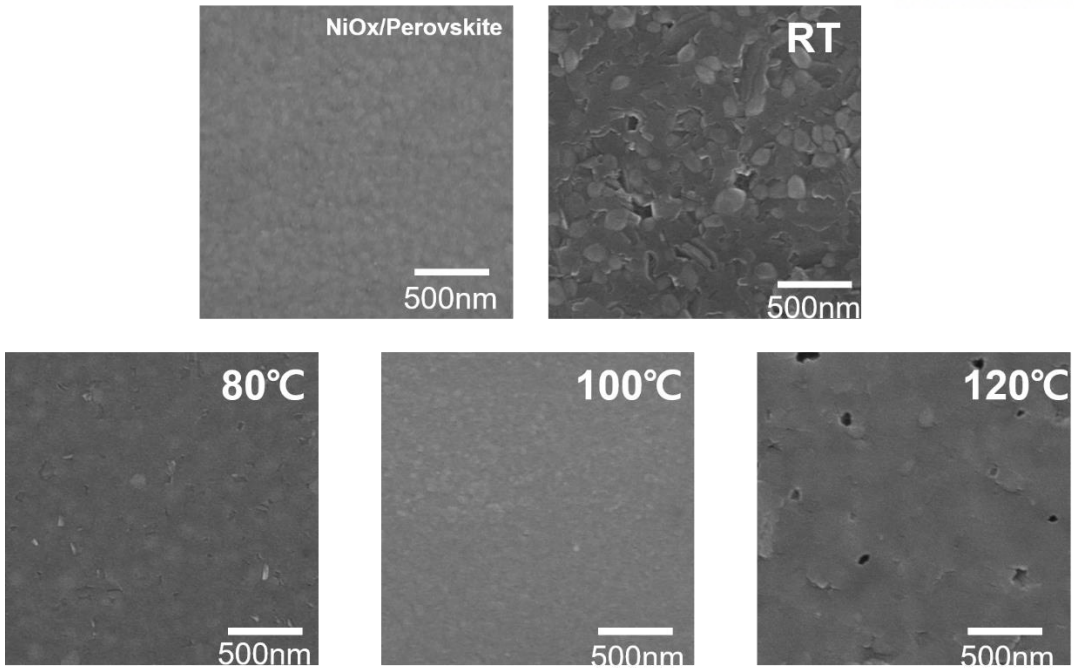

Figure 4.7 Surface morpholgy of quasi-2D perovskite film on the diffirent hot-casting temperautre

To confirm the crystal orientation in quasi-2D perovskite for different hot casting temperatures, we conducted grazing-incidence wide-angle X-ray scattering measurement (GIWAXS). The scattering patterns of different substrate preheating temperature are shown in **figure 4.8**. The RT cast films show ring-like Debye Scherer pattern, which is an indication of a randomly oriented crystal. In contrast, the hot-cast films display clearly the discrete Bragg spots. This indicates that inorganic PbX_6 sheets are highly perpendicular aligned with their increased (100) crystal plane peak in the Z-direction on the preheated substrate. The vertically grown perovskite crystal on the substrate can acts as efficient carrier transport pathway without interruption by insulting bulky organic cation.

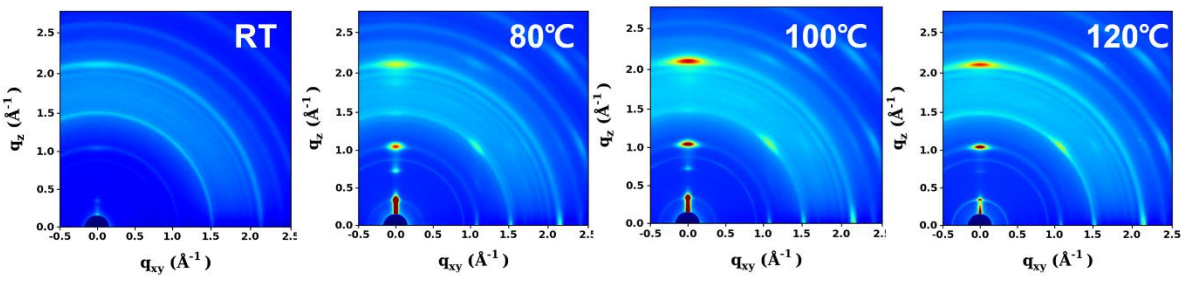

Figure 4.8 GIWAXS pattern images of quasi-2D perovskite film on the diffirent hot-casting temperautre

The X-ray diffraction (XRD) also supported perovskite crystallinity variation on the different preheating temperature of substrate. The diffraction peak at 5.2° and 10.5° are corresponding to (002)

and (004) plane of quai-2D cesium based crystal. The diffraction peaks of 3D $CsPbBr_3$ are observed at 15.1° and 30.2° corresponding to (100) and (200) plane. diffraction peak at 15.1° and 30.2°. As the substrate temperature increases, the intensity of the diffraction peaks also increases. The improved peak intensity of perovskite on preheated substrate means that the thermal energy of substrate during spin casting helps improve the crystallinity (**Figure 4.9**).

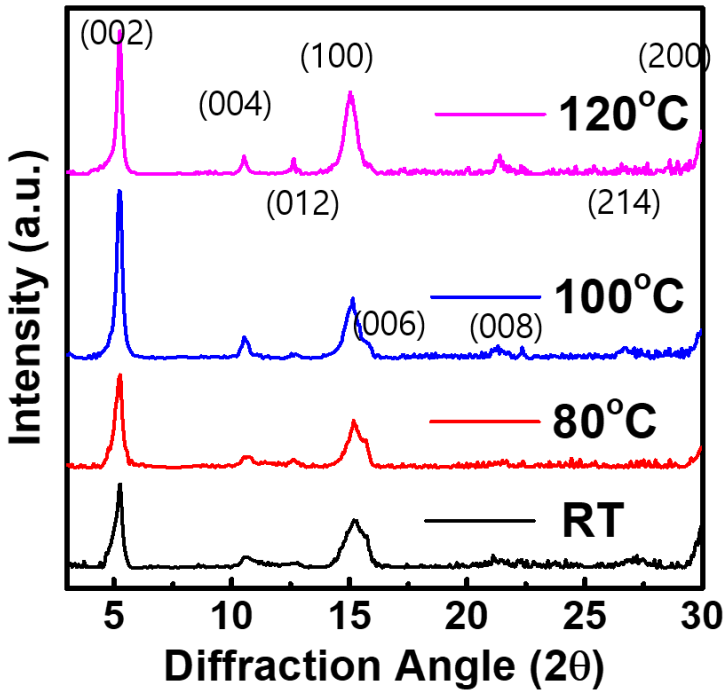

Figure 4.9 XRD intensity of quasi-2D perovskie film on the diffirent hot-casting temperautre

Improved morphology, crystal crystallinity and preferred orientation enhancement also affected optical property of perovskite films. The photoluminescence (PL) of perovskite films of different preheating temperature was measured under ultraviolet lamp excitation at 350nm. The photographs exhibit that the PL of perovskite films grown on a 100℃ substrate is shown to be brighter than PL of perovskite film grown on the other substrate temperature. However, the perovskite films grown on the substrate with 120℃ shows a relatively low PL intensity due to worse morphology (**figure 4.10**). Time-resolved photoluminescence (TRPL) of perovskite film on different substrate temperature was measured for investigation of the excited carriers lifetime. The emission of perovskite film on 100℃ substrates decayed with 5.09 ns, which is approximately 2 times as that of perovskite film on RT substrate. The prolongation of the lifetime in the perovskite on preheated substrate is due to formation of perovskite crystals with low defect density (**Figure 4.11**). The absorption spectra are that of typical a quasi-2D perovskite with low-dimensional multi-quantum well structure. The absorption spectra show that there is no significant difference depending on the temperature variation of the substrate. The

intensity of the exciton peak increases with the improvement of the perovskite crystallinity, but the position of the exciton peak does not change, indicating that the band gap is not affected by substrate temperature. (**Figure 4.12**)

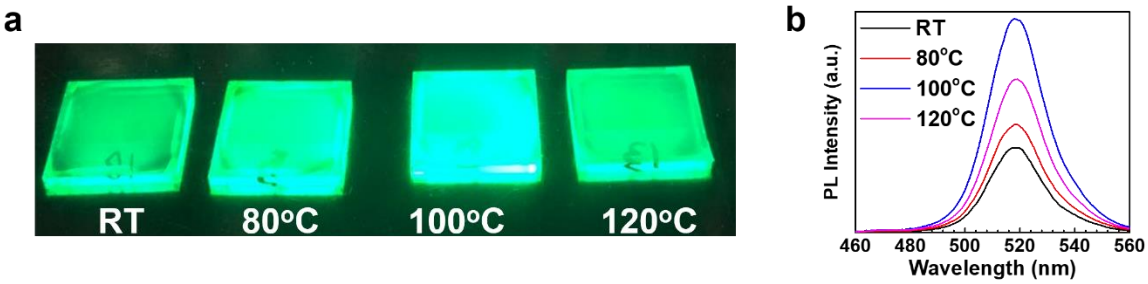

Figure 4.10 (a) Photographs of quasi-2D perovskite film on diffrent hot-casitng temperautre uder ultraviolet lamp excition at 350nm. (b) relativelty PL inteinsity of quasi-2D perovskite films

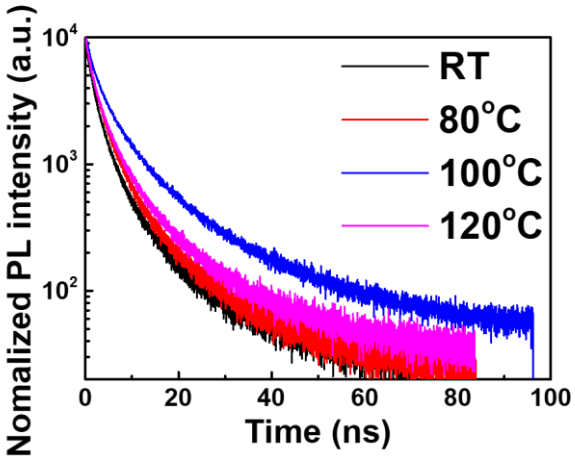

Figure 4.11 TRPL of perovskite film on different hot-casting temperature

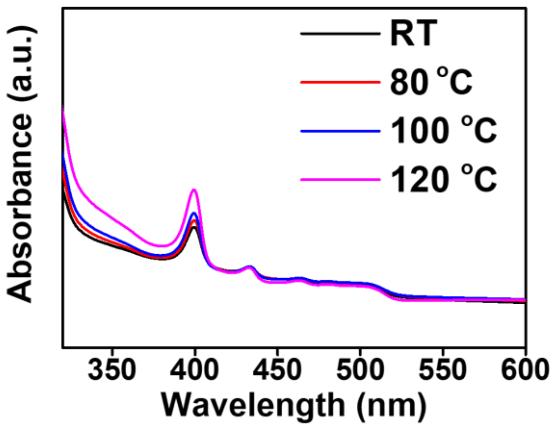

Figure 4.12 Absorbance spectra of quasi-2D perovskite film on different hot-casting temperature

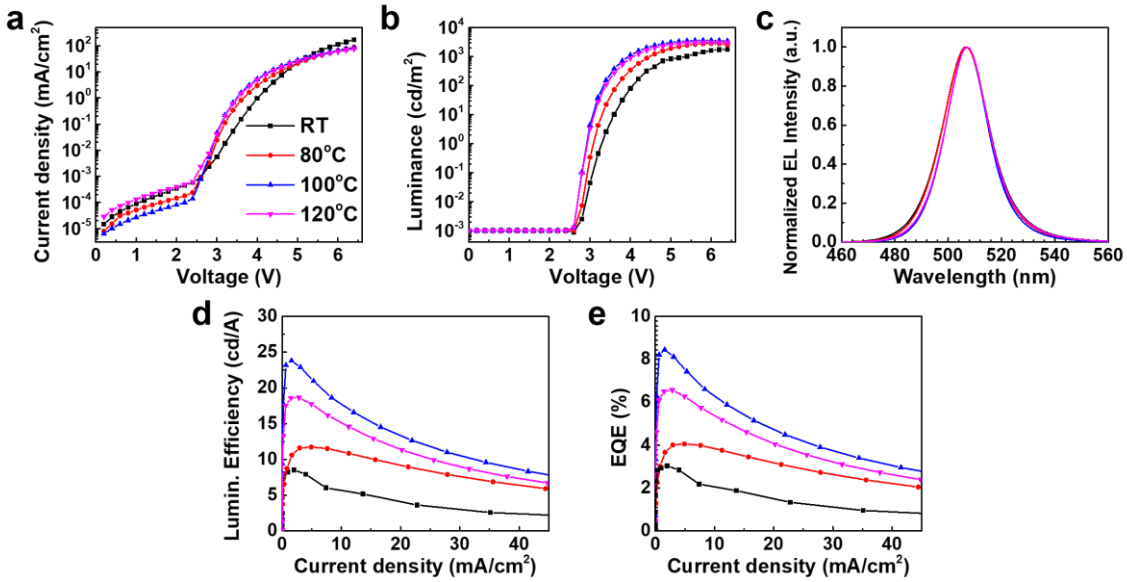

Figure 4.13 Device performance of PeLEDs fabricated don the different hot-casting temperature. a) Current density versus voltage, b) luminance versus voltage, c) normalized EL spectra, d) CE versus current density, e) EQE versus current density characteristics, e) normalized EL spectra.

The PeLEDs performances for the perovskite films on the different preheating temperature substrate were characterized. The PeLEDs characteristics are summarized in **table 4.1**. The J-V curves show that the perovskite film fabricated with RT substrate has a relatively high leakage current due to the not uniform and rough surface. The thermal energy of the substrate contributes to the improvement of the perovskite film morphology, which reduce the leakage current of devices. In the case of the temperature of substrate over 120°C, the pinholes are regenerated in the film, thereby producing a leakage current. Interestingly, the PeLEDs for the perovskite film grown on the preheating substrate show improved current injection than the PeLEDs for RT, which is considered to be caused by the better vertical orientation of PbX_6 sheet mentioned in GIWAXS section. The efficient charge injection has been reported to facilitate radiative recombination in the vertically oriented quasi 2d perovskite film. The maximum luminance increased from 1756 cdm^{-2} to 3607 cdm^{-2} and turn on voltage (V_T) decreases from 3.2 V to 2.8 V for the perovskite film on the 100°C-preheating temperature. Likewise, the measured luminance current efficiency and EQE value of the PeLEDs fabricated on the preheating substrates were 23.80 cd/A and 8.44 %, respectively, which increased to almost 300% compared to 8.52 cd/A and 3.03% for the control PeLEDs. We investigated by cross section SEM image whether the preheating substrate increased the thickness of the perovskite films and caused the performance improvement. Figure S8 shows the perovskite thickness according to the preheating temperature of the substrate. The approximate thickness is 70~80nm and there is no difference between the perovskite thickness grown on the preheating substrate and the perovskite thickness grown on the substrate of RT. The enhanced PeLEDs performance is independent of perovskite film thickness, and is related to better morphology

of perovskite film, high crystallinity and vertically aligned perovskite crystal. Moreover, the PVK layer coated between NiOx and perovskite film influences PeLEDs performance improvement due to a better hole injection (**Figure 4.14**).

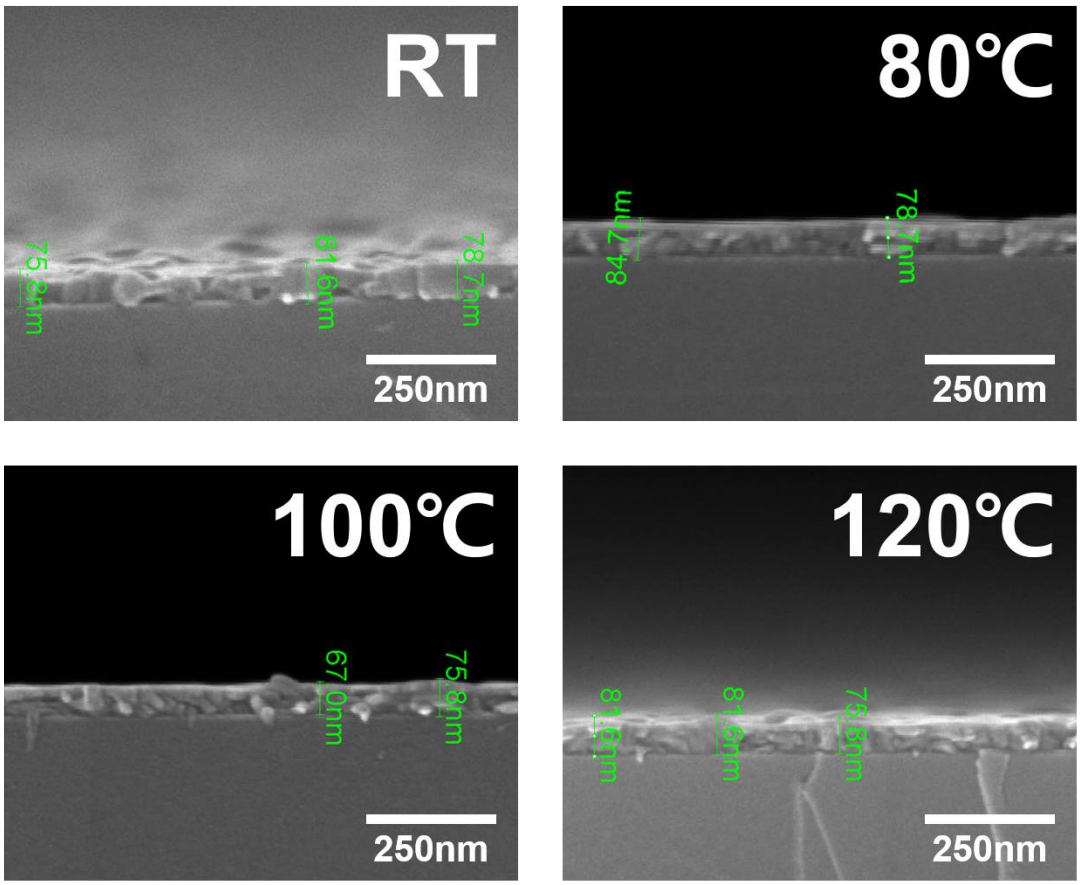

Figure 4.14 Thickness of quasi-2D perovskite film on the differnt hot-casting temperature.

The anti-solvent dropping method is conventional method for the deposition of perovskite film in small laboratory scale. However, this method is not suitable for deposition of perovskite film in large area scale because it its very sensitive to many technical conditions such as amount of anti-solvent, time to drop anti-solvent and even depending on the person handling it. We fabricated large area PeLEDs using the conventional anti-solvent dropping method and hot-casting method. The anti-solvent dropping method perovskite film was fabricated by spin casting the perovskite precursor film for 30 seconds and pouring 300 ul of chlorobenzene as anti-solvent. **Figure 4.15 a,b** exhibit the photograph of light emission area of PeLEDs for different fabrication method. The active area of PeLEDs is 0.8cm^2. The emission surface of PeLEDs fabricated with anti-solvent dropping method shows partial EL intensity fluctuation. The central part where the anti-solvent directly is dropped is bright, while the edge area is relatively dark, showing the traces of dropping of anti-solvent. We selected the 4-measurement positions (2-measurement positions in the middle area and 2-measuremnet positions in outer area applying

constant voltage. The PeLEDs of the anti-solvent method show the higher EL intensity of the b, c positions in the middle area than the EL intensity of the a, d positions in the outer area, while the PeLEDs of hot-casting method show similar EL intensity in a,b,c and d position. The corresponding normalized EL spectra are shown in **Figure 4.16**. The PeLEDs of the anti-solvent method has a peak shift of about 1nm depending on the position, but the PeLEDs of the hot-casting method show a peak shift of less than 0.5nm. We demonstrated a large-area PeLEDs using hot-casting method with a 5cm x 4cm substrate (active layer = 12.8cm^2) that is considered the largest size that we could handle by spin casting. (**Figure 4.15 c**) The emission surface shows no trace and very clear luminescence. The operational stability of PeLEDs according to the different perovskite films fabricating methods is compared in **figure 4.15 d**. The operating stability of PeLEDs were evaluated under a constant current of 0.5 mA/cm^2 (100 cd m^{-2}) with encapsulation in an air atmosphere. The PeLEDs fabricated by hot casting method has 20 minutes to retain 50% of its initial luminescence (T_{50}). On the other hand, PeLEDs fabricated by anti-solvent method shows relatively low operational stability (T_{50} = 7min.). The operational time-dependent EL spectra show that there is no peak shift regardless of the perovskite film formation method. (**Figure 4.17**)

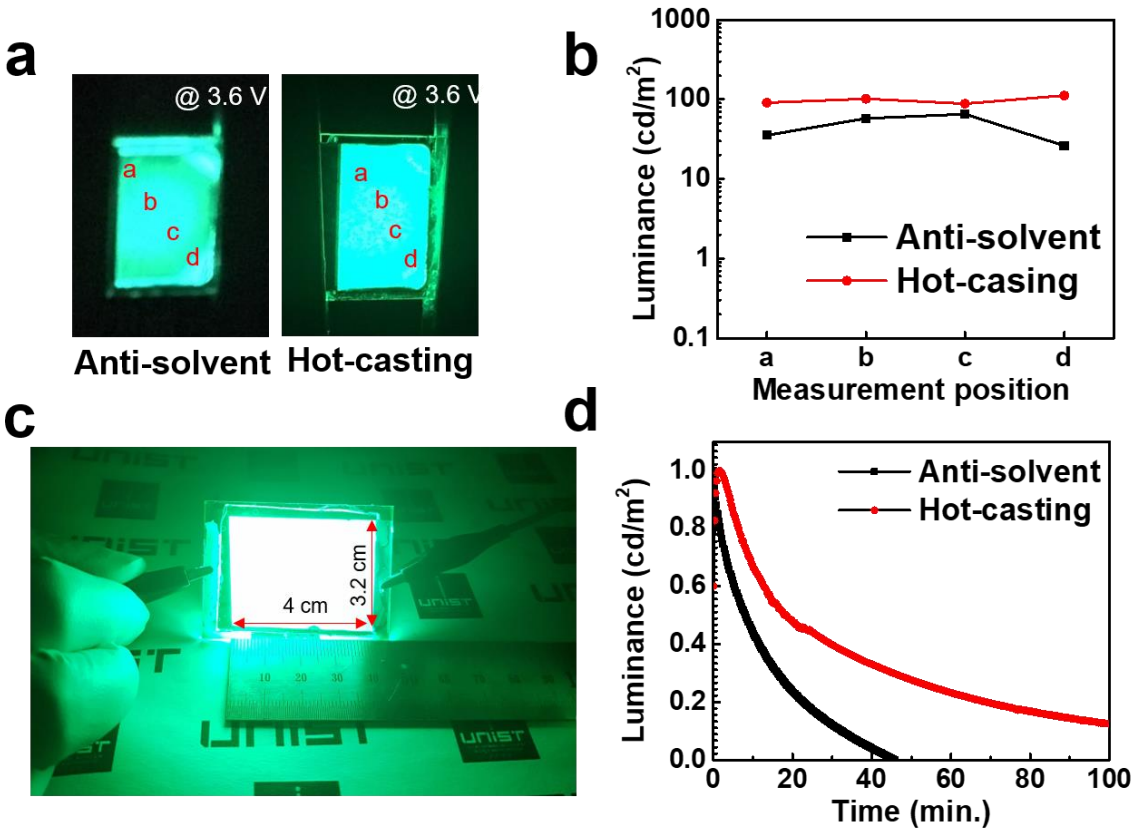

Figure 4.15 a) photograph of light emission area of PeLEDs for different fabrication method. b) partial EL intensity of 4-measurement point. c) Photograph of large-area PeLEDs applying 5V d) Operating stability of PeLEDs were evaluated under a constant current of 0.5 mA/cm^2 (100 cd m^{-2})

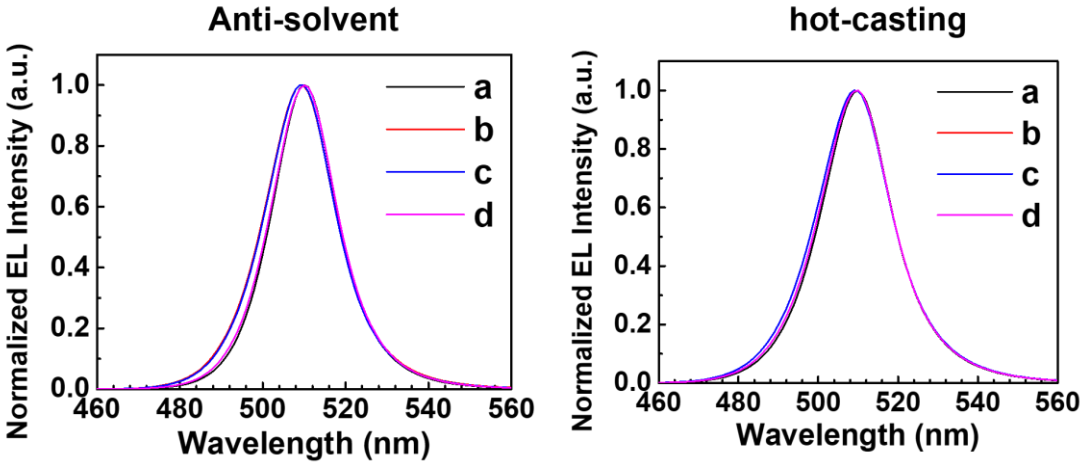

Figure 4.16 Normalized EL intensity of PeLEDs in a,b,c and d measurment points for differient fabriaciton methode.

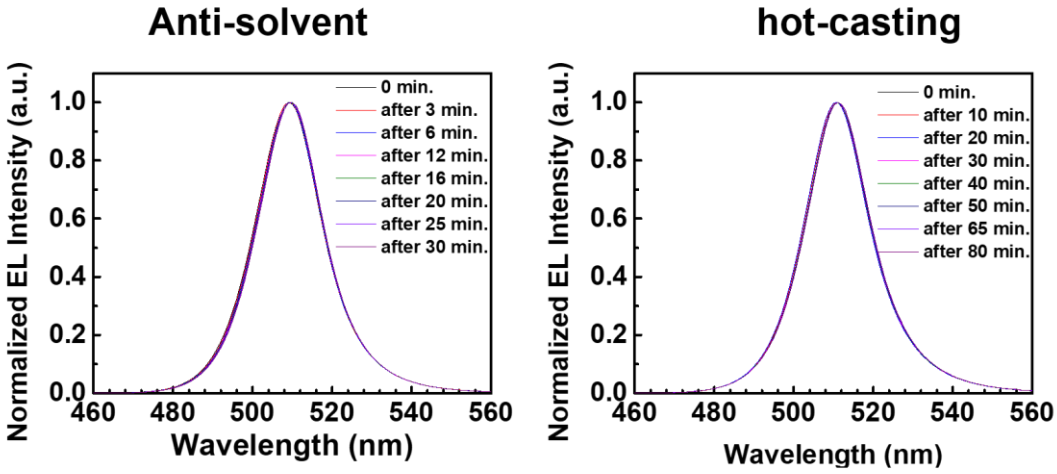

Figure 4.15 The operational time-dependent EL spectra of PeLEDs for different fabricating method

4.4 Conclusion

In summary, high efficiency Cs based quasi-2D PeLEDs have been demonstrated using hot-casting method with PVK interlayer. The introduction of PVK interlayer can reduce the hole injection barrier at the NiOx/perovskite interface. The hot-casting method to fabricate perovskite film allows uniform and pinhole-free morphology regardless of substrate surface energy. The thermal energy of the preheating substrate also contributes to the formation of highly crystalline and vertically oriented perovskite crystals. PeLEDs with an optimal substrate temperature were achieved with a maximum luminance of 3607 cdm^{-2} and maximum LE of 23.08 cdA^{-1} and maximum EQE of 8.44%. The hot-casting method not only affects the enhanced performance of PeLEDs, but also is useful for making large-area PeLEDs because the emission surface of PeLEDs shows the no trace and very clear luminescence.

Table 4.1. Summary of device performance of PeLEDs fabricated with Cs based quasi-2D perovskites on the differnt substrate preheating temperature

Hot casting temperature	Luminance $_{max}$ cd/m² @ bias	CE $_{max}$ cd/A @ bias	EQE $_{max}$ @ bias	Turn-on voltage @ 0.1 cd/m²
RT	**1756 @ 6.4**	**8.52 @ 4.2**	**3.03 @ 4.2**	**3.2**
80℃	**2813 @ 6.0**	**11.72 @ 4.2**	**4.05 @ 4.2**	**2.8**
100℃	**3607 @ 6.0**	**23.80 @ 3.6**	**8.44 @ 3.6**	**2.8**
120℃	**3091 @ 6.0**	**18.62 @ 3.8**	**6.56 @ 3.8**	**2.8**

4.5 Reference

[1] G. E. Eperon, V. M. Burlakov, P. Docampo, A. Goriely, H. J. Snaith, *Advanced Functional Materials* **2014**, 24, 151.

[2] Y. H. Kim, H. Cho, J. H. Heo, T. S. Kim, N. Myoung, C. L. Lee, S. H. Im, T. W. Lee, *Advanced materials* **2015**, 27, 1248.

[3] L. Protesescu, S. Yakunin, M. I. Bodnarchuk, F. Krieg, R. Caputo, C. H. Hendon, R. X. Yang, A. Walsh, M. Kovalenko, *Nano letters* **2015**, 15, 3692.

[4] D. Shi, V. Adinolfi, R. Comin, M. Yuan, E. Alarousu, A. Buin, Y. Chen, S. Hoogland, A. Rothenberger, K. Katsiev, *Science* **2015**, 347, 519.

[5] J. Song, J. Li, X. Li, L. Xu, Y. Dong, H. Zeng, *Adv Mater* **2015**, 27, 7162.

[6] S. D. Stranks, V. M. Burlakov, T. Leijtens, J. M. Ball, A. Goriely, H. J. Snaith, *Physical Review Applied* **2014**, 2, 034007.

[7] S. Zhou, R. Tang, L. Yin, *Advanced Materials* **2017**, 29, 1703682.

[8] K. Lin, J. Xing, L. N. Quan, F. P. G. de Arquer, X. Gong, J. Lu, L. Xie, W. Zhao, D. Zhang, C. Yan, W. Li, X. Liu, Y. Lu, J. Kirman, E. H. Sargent, Q. Xiong, Z. Wei, *Nature* **2018**, 562, 245.

[9] Y. Cao, N. Wang, H. Tian, J. Guo, Y. Wei, H. Chen, Y. Miao, W. Zou, K. Pan, Y. He, H. Cao, Y. Ke, M. Xu, Y. Wang, M. Yang, K. Du, Z. Fu, D. Kong, D. Dai, Y. Jin, G. Li, H. Li, Q. Peng, J. Wang, W. Huang, *Nature* **2018**, 562, 249.

[10] B. Zhao, S. Bai, V. Kim, R. Lamboll, R. Shivanna, F. Auras, J. M. Richter, L. Yang, L. Dai, M. Alsari, X.-J. She, L. Liang, J. Zhang, S. Lilliu, P. Gao, H. J. Snaith, J. Wang, N. C. Greenham, R. H. Friend, D. Di, *Nature Photonics* **2018**, 12, 783.

[11] H. Cho, S. H. Jeong, M. H. Park, Y. H. Kim, C. Wolf, C. L. Lee, J. H. Heo, A. Sadhanala, N. Myoung, S. Yoo, S. H. Im, R. H. Friend, T. W. Lee, *Science* **2015**, 350, 1222.

[12] A. Miyata, A. Mitioglu, P. Plochocka, O. Portugall, J. T. W. Wang, S. D. Stranks, H. J. Snaith, R. J. Nicholas, *Nat Phys* **2015**, 11, 582.

[13] K. Galkowski, A. Mitioglu, A. Miyata, P. Plochocka, O. Portugall, G. E. Eperon, J. T. W. Wang, T. Stergiopoulos, S. D. Stranks, H. J. Snaith, R. J. Nicholas, *Energ Environ Sci* **2016**, 9, 962.

[14] J. Byun, H. Cho, C. Wolf, M. Jang, A. Sadhanala, R. H. Friend, H. Yang, T. W. Lee, *Adv Mater* **2016**, 28, 7515.

[15] M. Yuan, L. N. Quan, R. Comin, G. Walters, R. Sabatini, O. Voznyy, S. Hoogland, Y. Zhao, E. M. Beauregard, P. Kanjanaboos, Z. Lu, D. H. Kim, E. H. Sargent, *Nat Nanotechnol* **2016**, 11, 872.

[16] S. Lee, D. B. Kim, I. Hamilton, M. Daboczi, Y. S. Nam, B. R. Lee, B. Zhao, C. H. Jang, R. H. Friend, J.-S. Kim, M. H. Song, *Advanced Science* **2018**, 5, 1801350.

[17] F.-X. Yu, Y. Zhang, Z.-Y. Xiong, X.-J. Ma, P. Chen, Z.-H. Xiong, C.-H. Gao, *Organic Electronics* **2017**, 50, 480.

[18] S. Zhuang, X. Ma, D. Hu, X. Dong, B. Zhang, *Ceramics International* **2018**, 44, 4685.

[19] J. Endres, D. A. Egger, M. Kulbak, R. A. Kerner, L. Zhao, S. H. Silver, G. Hodes, B. P. Rand, D. Cahen, L. Kronik, A. Kahn, *The Journal of Physical Chemistry Letters* **2016**, 7, 2722.

[20] Q. A. Akkerman, M. Gandini, F. Di Stasio, P. Rastogi, F. Palazon, G. Bertoni, J. M. Ball, M. Prato, A. Petrozza, L. Manna, *Nature Energy* **2016**, 2, 16194.

[21] J. Song, J. Li, X. Li, L. Xu, Y. Dong, H. Zeng, *Advanced Materials* **2015**, 27, 7162.

[22] Z. Xiao, R. A. Kerner, L. Zhao, N. L. Tran, K. M. Lee, T.-W. Koh, G. D. Scholes, B. P. Rand, *Nature Photonics* **2017**, 11, 108.

[23] J. Li, L. Xu, T. Wang, J. Song, J. Chen, J. Xue, Y. Dong, B. Cai, Q. Shan, B. Han, H. Zeng, *Advanced Materials* **2016**, 29, 1603885.

[24] E. Yassitepe, Z. Yang, O. Voznyy, Y. Kim, G. Walters, J. A. Castañeda, P. Kanjanaboos, M. Yuan, X. Gong, F. Fan, J. Pan, S. Hoogland, R. Comin, O. M. Bakr, L. A. Padilha, A. F. Nogueira, E. H. Sargent, *Advanced Functional Materials* **2016**, 26, 8757.

[25] J. Wang, N. Wang, Y. Jin, J. Si, Z.-K. Tan, H. Du, L. Cheng, X. Dai, S. Bai, H. He, Z. Ye, M. L. Lai, R. H. Friend, W. Huang, *Advanced Materials* **2015**, 27, 2311.

[26] N. Wang, L. Cheng, R. Ge, S. Zhang, Y. Miao, W. Zou, C. Yi, Y. Sun, Y. Cao, R. Yang, Y. Wei, Q. Guo, Y. Ke, M. Yu, Y. Jin, Y. Liu, Q. Ding, D. Di, L. Yang, G. Xing, H. Tian, C. Jin, F. Gao, R. H. Friend, J. Wang, W. Huang, *Nature Photonics* **2016**, 10, 699.

[27] W. Nie, H. Tsai, R. Asadpour, J.-C. Blancon, A. J. Neukirch, G. Gupta, J. J. Crochet, M. Chhowalla, S. Tretiak, M. A. Alam, H.-L. Wang, A. D. Mohite, *Science* **2015**, 347, 522.

[28] Y. C. Zheng, S. Yang, X. Chen, Y. Chen, Y. Hou, H. G. Yang, *Chemistry of Materials* **2015**, 27, 5116.

[29] C. Bi, Q. Wang, Y. Shao, Y. Yuan, Z. Xiao, J. Huang, *Nat Commun* **2015**, 6, 7747.

[30] H.-C. Liao, P. Guo, C.-P. Hsu, M. Lin, B. Wang, L. Zeng, W. Huang, C. M. M. Soe, W.-F. Su, M. J. Bedzyk, M. R. Wasielewski, A. Facchetti, R. P. H. Chang, M. G. Kanatzidis, T. J. Marks, *Advanced Energy Materials* **2016**, 7, 1601660.

[31] G. Cotella, J. Baker, D. Worsley, F. De Rossi, C. Pleydell-Pearce, M. Carnie, T. Watson, *Solar Energy Materials and Solar Cells* **2017**, 159, 362.

[32] H. Wu, C. Zhang, K. Ding, L. Wang, Y. Gao, J. Yang, *Organic Electronics* **2017**, 45, 302.

[33] A. T. Mallajosyula, K. Fernando, S. Bhatt, A. Singh, B. W. Alphenaar, J.-C. Blancon, W. Nie, G. Gupta, A. D. Mohite, *Applied Materials Today* **2016**, 3, 96.

[34] Y. H. Deng, E. Peng, Y. C. Shao, Z. G. Xiao, Q. F. Dong, J. S. Huang, *Energ Environ Sci* **2015**, 8, 1544.

[35] Z. Bi, Z. Liang, X. Xu, Z. Chai, H. Jin, D. Xu, J. Li, M. Li, G. Xu, *Solar Energy Materials and Solar Cells* **2017**, 162, 13.

[36] J. H. Heo, M. H. Lee, M. H. Jang, S. H. Im, *Journal of Materials Chemistry A* **2016**, 4, 17636.

[37] Z. Liang, S. Zhang, X. Xu, N. Wang, J. Wang, X. Wang, Z. Bi, G. Xu, N. Yuan, J. Ding, *RSC Advances* **2015**, 5, 60562.

[38] H. Tsai, W. Nie, J.-C. Blancon, C. C. Stoumpos, C. M. M. Soe, J. Yoo, J. Crochet, S. Tretiak, J. Even, A. Sadhanala, G. Azzellino, R. Brenes, P. M. Ajayan, V. Bulović, S. D. Stranks, R. H. Friend, M. G. Kanatzidis, A. D. Mohite, *Advanced Materials* **2018**, 30, 1704217.

[39] Y. Chen, Y. Sun, J. Peng, W. Zhang, X. Su, K. Zheng, T. Pullerits, Z. Liang, *Advanced Energy Materials* **2017**, 7, 1700162.

[40] R. Quintero-Bermudez, A. Gold-Parker, A. H. Proppe, R. Munir, Z. Yang, S. O. Kelley, A. Amassian, M. F. Toney, E. H. Sargent, *Nature Materials* **2018**, 17, 900.

Chapter 5. Acknowledgements (감사의 글)

2014 년도 봄에 아무것도 모르고 울산과학기술원에 진학하였던 저가 5 년이라는 시간이 빠르게 흘러 어느덧 졸업을 앞두고 있습니다. 시간을 돌이켜보면 막막했던 5 년동안 많은 일들이 있었습니다. 우선 저의 지도 교수님인 송명훈 교수님께 진심으로 감사드립니다. 지도교수님으로 송명훈 교수님을 만나게 된 건 큰 행운이었습니다. 교수님은 부족한 저에게 항상 자신감을 가져라 하셨고 격려의 말씀을 아끼지 않으셨습니다. 뿐만 아니라 인생의 선배로서 마음가짐이나 연구 생활을 마라톤에 비유하시면서 슬럼프에 빠지지 않도록 방향을 잡아주셨기에 지금의 제가 있습니다. 또한 KIST 에서 짧은 기간 이였지만 저를 좋게 봐주시고 졸업심사위원까지 맡아주신 경희대학교 고두현 교수님께도 진심으로 감사드립니다. 바쁘신 와중에도 함께 졸업심사 위원으로 저에게 많은 조언을 해주신 김진영 교수님, 박혜성 교수님, 권민상 교수님께도 감사의 인사를 올립니다. 교수님들의 심사가 제가 앞으로 박사의 길을 나아가는데 큰 지표가 될 것 같습니다.

타 대학교에서 아무 친구도 없는 울산에 왔을 때 어색하지 않게 친한 형동생처럼 저를 대해준 OPOL 식구들에게도 모두 고마운 마음입니다. 제일 큰형으로써 우리의 앞길을 닦아주시고 간 이보람 교수님, 저의 사수로서 새벽까지 같이 실험을 봐주신 재철이형, 동생이지만 형 같은 승진이, 같은 뜻을 가지고 있는 윤석이, 놀기도 잘놀고 일도 열심히 하는 상윤이, 랩의 없어서는 안되는 소금 같은 의대여, 랩장이자 맏형으로써 책임감있게 동생들을 챙겨주시는 대우형, 친동생 같은 충현이, 논문을 잘쓰는 종현이, 랩의 잡무를 담당하느라 애쓰는 지아, 적극적인 아영이, 그리고 막내 병수까지 모두 감사합니다. 저는 이제 곧 떠나지만 앞으로도 OPOL 이라는 소속감을 가지고 선후배님들에게 도움이 되는 연구자가 되겠습니다.

저에게 많은 지원을 해주고 졸업하고 입사할 LG 디스플레이에게도 감사의 인사를 드리고 싶습니다.

마지막으로 제가 하고자 하는 일을 묵묵히 믿어주시고 항상 기도해주신 부모님께도 감사드립니다.